Ensemble Monte Carlo simulation of electron transport in AlGaAs/GaAs heterostructures

Citation for published version (APA):
Nederveen, K. (1989). *Ensemble Monte Carlo simulation of electron transport in AlGaAs/GaAs heterostructures*. [Phd Thesis 1 (Research TU/e / Graduation TU/e), Electrical Engineering]. Technische Universiteit Eindhoven. https://doi.org/10.6100/IR318607

DOI:
10.6100/IR318607

Document status and date:
Published: 01/01/1989

Document Version:
Publisher’s PDF, also known as Version of Record (includes final page, issue and volume numbers)

Please check the document version of this publication:

• A submitted manuscript is the version of the article upon submission and before peer-review. There can be important differences between the submitted version and the official published version of record. People interested in the research are advised to contact the author for the final version of the publication, or visit the DOI to the publisher's website.
• The final author version and the galley proof are versions of the publication after peer review.
• The final published version features the final layout of the paper including the volume, issue and page numbers.

Link to publication

General rights
Copyright and moral rights for the publications made accessible in the public portal are retained by the authors and/or other copyright owners and it is a condition of accessing publications that users recognise and abide by the legal requirements associated with these rights.

- Users may download and print one copy of any publication from the public portal for the purpose of private study or research.
- You may not further distribute the material or use it for any profit-making activity or commercial gain
- You may freely distribute the URL identifying the publication in the public portal.

If the publication is distributed under the terms of Article 25fa of the Dutch Copyright Act, indicated by the “Taverne” license above, please follow below link for the End User Agreement:

www.tue.nl/taverne

Take down policy
If you believe that this document breaches copyright please contact us at:

openaccess@tue.nl

providing details and we will investigate your claim.

Download date: 04. Oct. 2023

Ensemble Monte Carlo simulation

of

ELECTRON TRANSPORT IN AlGaAs/GaAs HETEROSTRUCTURES

Karel Nederveen

Ensemble Monte Carlo simulation

of

ELECTRON TRANSPORT IN AlGaAs/GaAs HETEROSTRUCTURES

CIP-GEGEVENS KONINKLIJKE BIBLIOTHEEK, DEN HAAG

Nederveen, Karel

Ensemble Monte Carlo simulation of electron transport
in AlGaAs/GaAs heterostructures / Karel Nederveen. -
[S.l. : s.n.]. - Fig., tab.
Proefschrift Eindhoven. - Met lit. opg., reg.
ISBN 90-9003048-4
SISO 663.42 UDC 621.382.323.001.57(043.3) NUGI 832
Trefw.: halfgeleidermodellen / galliumarsenidehalfgeleiders.

Druk: WIBRO dissertatiedrukkerij, Helmond

Omslagontwerp: Henri van Nuenen, Eindhoven

Ensemble Monte Carlo simulation

of

ELECTRON TRANSPORT IN AlGaAs/GaAs HETEROSTRUCTURES

PROEFSCHRIFT

TER VERKRIJGING VAN DE GRAAD VAN DOCTOR
AAN DE TECHNISCHE UNIVERSITEIT EINDHOVEN,
OP GEZAG VAN DE RECTOR MAGNIFICUS,
PROF. IR. M. TELS, VOOR EEN COMMISSIE AANGEWEZEN
DOOR HET COLLEGE VAN DEKANEN
IN HET OPENBAAR TE VERDEDIGEN OP
VRIJDAG 27 OKTOBER 1989 TE 16.00 UUR

door

KAREL NEDERVEEN
geboren te Rotterdam

Dit proefschrift is goedgekeurd door de promotoren:
Prof. dr. F. M. Klaassen en
Prof. dr. G. Salmer
Copromotor: Dr. ir. Th. G. van de Roer

aan mijn ouders

CONTENTS

LIST OF SYMBOLS

Symbol	Meaning	Unit
$a_{\vec{q}}$	annihilation operator	
$a^{\dagger}_{\vec{q}}$	creation operator	
A	surface	m^2
$\vec{B}$	magnetic field	T
C_{GS}	source-to-gate capacitance	F
DT	field-adjusting timestep	s
e	elementary charge	C
$\vec{E}$	electric field	V/m
f	distribution function	
F	cumulative distribution function	
f_T	cutoff frequency	Hz
g_m	transconductance	S/m
$G(\vec{k},\vec{k}')$	overlap function	
$\hbar$	Planck's constant	J·s
HX	mesh cell size in x-direction	m
HY	mesh cell size in y-direction	m
$\mathcal{H}'$	energy operator	J
$I(\vec{k},\vec{k}')$	overlap integral	
I_D	drain current	A
$\vec{k}$	wave vector	m^{-1}
$\vec{K}$	two-dimensional wave vector	m^{-1}
k_B	Boltzmann's constant	J/K
k_d	inverse Debye wavelength	m^{-1}

L_T	width of a quantum well at energy W_T	m
m_0	free-electron rest mass	kg
m^*	electron effective mass	kg
M	number of simulation electrons	
$M(\vec{k},\vec{k}')$	matrix element for the transition $\vec{k}$ to $\vec{k}'$	J
N_c	effective density of states in the conduction band	m^{-3}
N_c	quantity related to electron density in a computer plasma (chapter 6)	
n_e	electron density	m^{-3}
$n_{\vec{q}}$	number of states with wave vector $\vec{q}$	
N_D	donor density	m^{-3}
N_D^+	ionized donor density	m^{-3}
$\vec{q}$	phonon wave vector	m^{-1}
$\vec{Q}$	two-dimensional phonon wave vector	m^{-1}
Q_c	charge assigned to a simulation electron	C
$\tilde{r}$	random number	
$\vec{r}$	position vector	m
$\vec{R}$	two-dimensional position vector	m
$S(\vec{k},\vec{k}')$	rate of transition $\vec{k}$ to $\vec{k}'$	Hz
S_o	disorder parameter	
t	time	s
t_T	transit time	s
T	temperature	K
$u_{\vec{k}}$	periodic part of the Bloch function	$m^{3/2}$
$\vec{v}$	velocity vector	m/s
v_T	thermal velocity	m/s
V	volume	m^3

V_{DS}	source-to-drain voltage	V
V_G	gate voltage	V
W	energy	J
W_T	threshold energy for Quantum Well Transfer	J
W_c	conduction band energy level	J
W_g	band gap	J
W_n	energy of subband n in a quantum well	J
W_F	Fermi energy	J
x	Al-mol content in $Al_xGa_{1-x}As$	
α	non-parabolicity parameter	eV^{-1}
ϵ_0	permittivity of vacuum	F/m
ϵ_s	static dielectric constant	
ϵ_∞	high-frequency dielectric constant	
ζ	chemical potential or Fermi level	J
Γ	total scatter rate including self-scattering	Hz
λ	scatter rate	Hz
λ_D	Debye wavelength	m
Λ	total scatter rate without self-scattering	Hz
ω_{pe}	plasma frequency	rad/s
Ω	volume	m^3
ρ	charge density	m^{-3}
τ_c	collision time	s
τ_h	heating time	s
τ_{pe}	inverse plasma frequency	s
ϕ	scatter angle	
ϕ	potential (chapter 5 and 6)	V
ϕ_B	Schottky barrier energy	eV

$\phi_{n_{\vec{q}}}$	phonon wave function	
$\chi_{n_{\vec{q}}}$	combined wave function of electron and phonons	$m^{3/2}$
Ψ	electron wave function	$m^{3/2}$

Chapter 1

INTRODUCTION

The subject and title of this thesis is 'Monte Carlo simulation of electron transport in AlGaAs/GaAs heterostructures'. In this introductory chapter a short account of the importance and the range of applications of AlGaAs/GaAs heterostructures will be given. Furthermore, the necessity of simulation in general, and simulation making use of the Monte Carlo method in particular, is explained. The basic Boltzmann transport equation, describing electron transport in a metal or semiconductor under influence of external forces, will be introduced. In connection with this equation the electron dynamics will be defined.

Finally an outline of the thesis is given.

1.1 Heterostructures

A heterostructure is a semiconductor crystal which consists of different semiconducting materials. At present, the most widely used heterostructures involve the binary III–V compound GaAs in combination with the ternary alloy $Al_xGa_{1-x}As$, where x is a compositional parameter between 0 and 1. The ternary alloy will be briefly denoted as AlGaAs. A great advantage is that both materials are lattice-matched. This minimizes the number of broken bonds at the interface and prevents undesirable electronic effects.

Associated with the abrupt change of semiconductor material is an abrupt change in energy band. As the energy band of AlGaAs is influenced by the compositional parameter, the difference in energy band is controllable and can be considered as a design parameter.

The AlGaAs/GaAs heterostructures have attracted a lot of interest, both for fundamental physical reasons as for their practical applications. An example of the former aspect is the 1985 Nobel prize in physics, which was awarded to Klaus von Klitzing for his accurate measurements of the Quantum Hall effect. This effect was first discovered in 1980 in the so-called two-dimensional electron gas at the SiO_2/Si interface of a MOSFET, at liquid helium temperatures. A couple of months later the same effect was found to occur at the AlGaAs/GaAs interface.

AlGaAs double heterostructure lasers have found a wide application in Compact Disc players. Heterojunction bipolar transistors (HBT), e.g. with an N-AlGaAs/p-GaAs/n-GaAs structure, are promising devices for ultra-high-speed integrated circuits. A very important device is the High Electron Mobility Transistor (HEMT), which might become a key device in future VLSI applications. Compared with its predecessor, the GaAs MESFET, it has low noise figures and combines high switching speeds with a low power dissipation.

Excellent reviews concerning heterojunctions have been given by Casey and Panish (1978), Kroemer (1985) and Milnes (1986).

1.2 Simulation

The application of a new material or the development of a new device is a matter of high cost and takes a lot of time. Therefore, for economical reasons, one is interested in a simulation tool for the prediction of the performance of the material or device to be developed. This tool may serve on the one hand in optimizing various parameters, like doping, the compositional parameters (when ternary or quaternary alloys are involved), or gate length, which affect the characteristics of the semiconductor (device). On the other hand it may help studying and understanding of physical properties.

The (Ensemble) Monte Carlo method is especially suited for the microscopic modelling of electron transport. With this method electron transport properties can be determined from first principles. Neither short time scales, in the order of the free flight time of an electron nor short distances, in the order of the mean free path of an electron, pose a principal problem.

In this thesis, the Ensemble Monte Carlo method is applied to the study of transport properties of AlGaAs/GaAs heterostructures. In this respect, the following problems are addressed:

- which *physical mechanisms* play a role in determining the electron transport in these structures,
- how can these mechanisms be *modelled*, and
- what is their actual *effect* on the device properties?

1.2.1 The Boltzmann transport equation

As may be clear from the above, for transistor applications the most interesting physical phenomenon in a semiconductor is the charge carrier transport under influence of an external electric field. Conduction electrons (being in a state of equilibrium) will be accelerated when an external field is applied, and the extra energy thus acquired will be passed on to the lattice by excitation of lattice vibrations, i.e. the electron system emits phonons (the quanta of energy of the lattice vibrations). Inversely, the electron system may absorb phonons, and after some time a situation of steady state will be reached.

The distribution function $f_n(\vec{k},\vec{r},t)$, being the occupation probability of a state characterized by a wave vector $\vec{k}$ at location $\vec{r}$ at time t, gives a complete description of the electron system in a band with index n. The above distribution function is a solution of the well-known Boltzmann transport equation (BTE) (Madelung 1978)

$$\frac{\partial f_n(\vec{k},\vec{r},t)}{\partial t} = -\frac{\partial \vec{k}}{\partial t}\cdot\vec{\nabla}_{\vec{k}} f_n(\vec{k},\vec{r},t) - \frac{\partial \vec{r}}{\partial t}\cdot\vec{\nabla}_{\vec{r}} f_n(\vec{k},\vec{r},t) + \left.\frac{\partial f_n(\vec{k},\vec{r},t)}{\partial t}\right|_{sc.} . \quad (1.1)$$

The first term on the right-hand side accounts for the influence of external forces, the second one is the diffusion term and the third, the scatter term, refers to scatter processes (possibly) involving the exchange of phonons between the electron system and the crystal lattice. Instead of 'scatter term' this term is also referred to as 'collision term'.

The number of electrons in a volume element $(\vec{r}, d\tau_{\vec{r}})$ of $\vec{r}$-space and $(\vec{k}, d\tau_{\vec{k}})$ of $\vec{k}$-space at time t is given by the product of the distribution function and the volume element $d\tau_{\vec{r}}\ d\tau_{\vec{k}}$. Actually, an electron is represented by a wave packet formed out of one-electron states. The wave packet is constructed with Bloch functions $\Psi_{n\vec{k}}(\vec{r}) = u_{n\vec{k}}(\vec{r})\exp(i\vec{k}\cdot\vec{r})$, being plane wave solutions of Schrödinger's equation. The electron thus described is in fact a quasi-particle and is called a 'crystal electron'. It faces only external forces and the 'forces' of lattice vibrations, to which it responds differently from a free electron in an empty lattice (Madelung 1978). The interactions with the fixed lattice are implicitly taken care of by means of the relation between energy and wave vector.

The packet extends in real ($\vec{r}$-) as well as in reciprocal ($\vec{k}$-) space, and the extents, respectively $\Delta\vec{r}$ and $\Delta\vec{k}$, are related to each other by Heisenberg's uncertainty relation $\Delta\vec{r}\cdot\Delta\vec{k} \geq 2\pi$. This should be realized when considering an electron at location $\vec{r}$ with wave vector $\vec{k}$.

Taking this into account, the velocity $\frac{\partial\vec{r}}{\partial t}$ in the diffusion term of eq.(1.1) can be replaced by the group velocity of the wave packet

$$\frac{\partial\vec{r}}{\partial t} = \frac{1}{\hbar} \vec{\nabla}_{\vec{k}} W(\vec{k}), \tag{1.2}$$

where $W(\vec{k})$ is the kinetic energy of an electron with wave vector $\vec{k}$. Furthermore, the external forces can be accounted for by

$$\frac{\partial\vec{k}}{\partial t} = -\frac{e}{\hbar} (\vec{E} + \vec{v} \times \vec{B}). \tag{1.3}$$

The electron dynamics herewith defined is often referred to as 'quasi-classical' (Ziman 1972), with the role of the momentum represented by $\hbar\vec{k}$. $\hbar\vec{k}$ is often referred to as the 'crystal momentum' or 'pseudomomentum', because the expectation value of the momentum is not equal to $\hbar\vec{k}$ (Madelung 1978).

Analogous to the BTE for the electron system a BTE can be set up for the phonon system as well, and one is left with two coupled sets of differential equations describing the electron system and the phonon system, respectively.

In order to simplify the solution of the BTE, it is assumed that the phonon system sets up an equilibrium state so quickly that disturbances in the phonon system can be ignored (Bloch assumption). Then the scatter term at the right hand side of the BTE for electrons can be written as (with the index n and $\vec{k}$, $\vec{r}$ and t left out wherever possible)

$$\left.\frac{\partial f}{\partial t}\right|_{sc.} = \frac{V}{(2\pi)^3}\iiint d\vec{k}' \{S(\vec{k}',\vec{k})[1-f(\vec{k})]f(\vec{k}')-S(\vec{k},\vec{k}')[1-f(\vec{k}')]f(\vec{k})\}, \quad (1.4)$$

where $S(\vec{k},\vec{k}')$ is the transition rate for an electron in state $\vec{k}$ to a state $\vec{k}'$, while a change of energy band is permitted.

Using this transformation the BTE has become an integro-differential equation, which is only solvable for very simple cases.

1.2.2 Short survey of the Monte Carlo method

In general, the name Monte Carlo method is used for any method of solution where random numbers are involved. The first description of a mathematical experiment with a random character seems to have been the determination of π by throwing darts (Hall 1873). The systematic development and the name (thought of by E. Fermi) of the Monte Carlo method dates from 1944 from the work on the atomic bomb. Two of the most important pioneers have been S. M. Ulam and J. von Neumann (1947). Nowadays extensive use of these methods is made in such fields as nuclear physics, operations research, chemistry, biology and theoretical physics.

Its use in determining electrical transport has been initiated by Kurosawa (1966). Kurosawa as well as his early successors, the most important of which are Fawcett, Boardman and Swain (1970) at first instance considered one electron during a long time and arrived at the steady state applying the theorem of ergodicity. Lebwohl and Price (1971) were the first to introduce what has become known as the Ensemble Monte Carlo method, in 'simultaneously' following several thousands of electrons (the 'ensemble'). Important contributions have further been made by Littlejohn, Hauser and Glisson (1977) and Kaszynski (1979). Excellent reviews of (Ensemble) Monte Carlo methods in electron transport calculations have been given by Price (1979) and Jacoboni and Reggiani (1983).

The Ensemble Monte Carlo method has not found application in bulk material only, but is also applicable to the simulation of semiconductor devices. A review of numerous methods that can be used for the modelling of submicron devices has been given by Castagné (1985), and a review concentrating on Monte Carlo techniques by Lugli and Jacoboni (1987). An extensive account of how to combine Monte Carlo methods and two-dimensional Poisson routines into a numerically stable scheme has been given by Hockney and Eastwood (1981).

The history of two-dimensional modelling using Monte Carlo methods for devices based on GaAs starts with the simulation of the MESFET, especially with the work of Hockney, Warriner and Reiser (1974), where for the first time two-dimensional particle models were applied. This has been followed by numerous others among which Warriner (1977a), Williams (1982) and Williams et al. (1985), Moglestue (1983, 1984, 1985, 1986) and Awano et al. (1983, 1984).

Later on attempts have been made to model (all) aspects of the High Electron Mobility Transistor (HEMT), which transistor is the successor of the GaAs MESFET and makes use of an AlGaAs/GaAs heterojunction in its structure. Ensemble Monte Carlo calculations without taking into account subband scattering have been performed by Wang and Hess (1985), Mouis et al. (1986), Fauqemberge et al. (1987, 1988) and Thobel (1988), and calculations including subband scattering by Ravaioli and Ferry (1986) and Tomizawa et al. (1985).

Other calculations on the HEMT, based on the Boltzmann moment equations, where an increasing number of moments is used, depending on the sophistication of the method, have been done by Widiger et al. (1984, 1985), Yuh Fong Tang (1985) and Buot (1987).

In this thesis Ensemble Monte Carlo calculations have been carried out to study the effects of degeneracy and various scatter mechanisms on the electron transport in GaAs (chapter 4), real space transfer between AlGaAs and GaAs (chapter 5) and various aspects of an HEMT (chapter 6). Since a more detailed discussion of the Ensemble Monte Carlo method and the scatter mechanisms is essential for this study, these two subjects are discussed in chapters 2 and 3.

1.3 Outline of this thesis

In chapter 2 the Ensemble Monte Carlo method is outlined. In this method a solution for the Boltzmann transport equation is obtained from the knowledge of the electric field strength and the scatter rates. The field strength can either be imposed or calculated self-consistently by solving Poisson's equation.

In chapter 3 the three-valley model for the band structure of GaAs (and AlGaAs) is introduced. From the general expressions following from first-order perturbation theory the calculation of the scatter rates for the various processes in GaAs and AlGaAs is discussed.

Since high electron concentrations may occur near the interface of an AlGaAs/GaAs heterojunction (typically in the order of 10^{18} cm^{-3}), degeneracy effects (Pauli exclusion principle) and electron—electron scattering can play a role. The purpose of chapter 4 is to study these two mechanisms in n-doped bulk GaAs, where the electrons are considered to be homogeneously distributed. An existing model to introduce the degeneracy effects in low-field Ensemble Monte Carlo calculations is adapted and made suitable for high field purposes. With this extended model for the first time velocity—field curves have been obtained taking into account degeneracy effects. In addition, the combined effect of electron—electron scattering and degeneracy effects have been considered together in one model for the first time.

At the heterointerface band-bending occurs, consequently electrons experience an electric field which pushes them towards the interface. The effect of this transverse field on the electron transport, parallel to the interface under influence of a longitudinal field, is studied in chapter 5. The fact that electrons may cross the potential barrier between GaAs and AlGaAs, which is called the real space transfer effect, is taken into account. The results indicate that the velocity of the electrons in GaAs parallel to the interface is increased in comparison with the velocity in undoped bulk GaAs. This effect is only due to classical effects, as energy discretization has not been included. The separate effects of the transverse field and real space transfer will be clearly demonstrated.

An Ensemble Monte Carlo model, in which Poisson's equation is solved in two dimensions, has been developed to investigate the properties of an HEMT (chapter 6). Special emphasis has been given to the study of existing criteria which ensure the stability of the calculations. It is clearly demonstrated which time integration scheme should be used to obtain a numerically stable scheme. For an HEMT with a gate length of 0.3 μm I–V characteristics and small-signal parameters have been determined. A detailed study has been carried out to determine which electrons (in Γ-, L- or X-valley) contribute to the real space transfer occurring in the device. The influence of gate length and interelectrode spacings on the small-signal parameters has been investigated.

Especially at low temperatures, energy quantization occurs in the quantum well at the interface, owing to the quantization of the wave vector transverse to the interface. This effect has been neglected in all cases mentioned above. For Monte Carlo purposes a description of the transition between situations with a discrete and a continuous energy spectrum has been developed (chapter 7). This new transition process is called 'quantum well transfer'.

All calculations reported in the present work have been performed on an Alliant FX8 computer, with the possibility of four processors concurrently working on the same problem.

Chapter 2

ENSEMBLE MONTE CARLO METHOD

2.1 Outline of the method

Compared with various analytical and iterative methods of solving the Boltzmann transport equation (1.1), the Monte Carlo method has the advantage that no a priori (simplifying) assumptions concerning the form of the distribution function are made, the evolution in time of the distribution function may be studied, and complicated energy band structures may be inserted (Vinter 1973, Jacoboni and Reggiani 1983).

Also, in device simulations, complicated geometrical structures are not difficult to handle. Note that in this method the Boltzmann transport equation is not solved explicitly, but a numerical description of the electron system in the six-dimensional phase space is obtained only from the knowledge of the scatter rates and the external fields.

In the Monte Carlo method used for transport calculations the motion of an electron is modelled as a sequence of free flights interrupted by scatter processes. In the Ensemble Monte Carlo version of this procedure, which will be applied throughout this thesis, an ensemble of electrons is followed 'simultaneously'. The ensemble averages over physical quantities of interest are collected at prescribed observation times with equidistant intervals and thus the evolution in time of the electron system under investigation is obtained. The length of the free flight, the scatter process and the change of the state of the electron as a consequence of the scattering are chosen out of different alternatives with known probability distributions, with the help of uniformly distributed random numbers.

In general, the random selection of a variable x with a certain normalized distribution f(x) is done by mapping the uniform distribution of the random number $\tilde{r}$ onto f(x):

$$\int_0^{\tilde{r}} dr = \int_0^{\tilde{x}} dx\ f(x). \tag{2.1}$$

Then

$$\tilde{r} = F(\tilde{x}), \tag{2.2}$$

where F(x) is the cumulative distribution function, or

$$\tilde{r} = P(x \leq \tilde{x}), \tag{2.3}$$

where $P(x \leq \tilde{x})$ is the probability that $x \leq \tilde{x}$. The required $\tilde{x}$ is obtained by inversion,

$$\tilde{x} = F^{-1}(\tilde{r}). \tag{2.4}$$

See fig. 2.1 for an illustration of the inversion technique.

2.1.1 Selection of the free flight time

At the heart of the Monte Carlo scheme is the calculation of the free flight time of an electron. The free flight time, also called 'scatter time', is related to the scatter probability. For each process i described by a transition rate $S_i(\vec{k},\vec{k}')$ a scatter rate is calculated according to

$$\lambda_i(\vec{k}) = \frac{V}{(2\pi)^3}\iiint d\vec{k}'\ S_i(\vec{k},\vec{k}'), \tag{2.5}$$

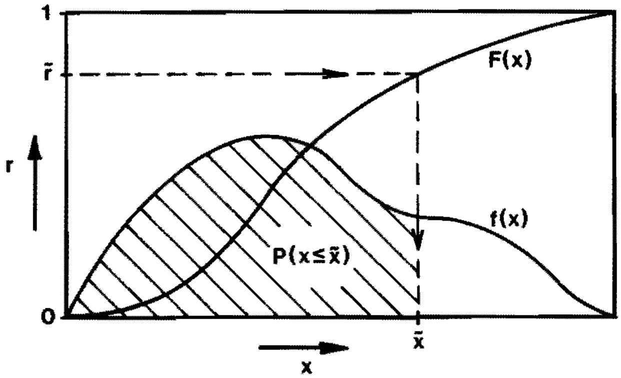

Fig. 2.1 *The principle of the inversion technique. A variable* $\tilde{x}$ *is selected from a distribution f(x) with the help of a random number* $\tilde{r}$. *(After Press et al., 1986.)*

or, in spherical coordinates

$$\lambda_i(k) = \frac{V}{(2\pi)^3} \int_0^\infty \int_0^\pi \int_0^{2\pi} dk' \ d\theta \ d\phi \ k'^2 \sin\theta \ S_i(\vec{k},\vec{k}'). \tag{2.6}$$

The total scatter rate is $\Lambda(\vec{k}) = \sum \lambda_i(\vec{k})$. Therefore $\Lambda[\vec{k}(t)]dt$ is the probability that an electron experiences a scatter process in a time dt. Hence, the probability $p_0(t,t_0)$ that an electron scattered at $t = t_0$ has not yet undergone another process after time t is (Jacoboni and Reggiani 1983)

$$p_0(t,t_0) = \exp\{ -\int_{t_0}^{t} dt' \ \Lambda[\vec{k}(t')] \}. \tag{2.7}$$

Thus, the probability $p_1(t,t_0)$ that an electron will scatter at a time between t and t+dt after its previous scattering is given by

$$p_1(t,t_0)dt = \Lambda[\vec{k}(t)] \ \exp\{ -\int_{t_0}^{t} dt' \ \Lambda[\vec{k}(t')] \} \ dt. \tag{2.8}$$

As will be clear from eqs.(2.1–2.4) the free flight time is chosen as

$$\tilde{t} = \left[\int_0^{\tilde{r}} dt \; p_1(t,t_0) \right]^{-1}. \tag{2.9}$$

As $\vec{k}$ changes constantly in time under influence of external forces, see eq.(1.3), and $\Lambda[\vec{k}(t)]$ is not an analytical function of $\vec{k}$, the expression in eq.(2.9) cannot easily be evaluated, only at high computational cost.

A solution for this problem has been proposed by Rees (1968, 1969). He introduced a 'dummy' scatter process, called 'self-scattering', which in no way affects the state of the electron. The rate of this process is such that during the period of interest the total scatter rate is a constant, denoted by Γ. The rate for this process is $\Gamma - \Lambda[\vec{k}(t)]$, which of course should be greater than or equal to zero. Thus, during the period of interest

$$\Gamma \geq \Lambda[\vec{k}(t)], \tag{2.10}$$

where the range of $\vec{k}$ covers all the values occupied by the electrons. Γ may be a constant, or depending upon $\vec{k}$ or t, but not upon the random number $\tilde{r}$. The inclusion of this fictitious process does not affect the rate of occurrence of 'real' processes, as proven by Fawcett et al. (1970).

Now, from eq.(2.8)

$$p_1(t,t_0) = \Gamma \exp(-\Gamma t), \tag{2.11}$$

and, with eq.(2.9)

$$\tilde{t} = - \frac{\ln(1 - \tilde{r})}{\Gamma}, \tag{2.12}$$

or, since $\tilde{r}$ has a uniform distribution on [0,1)

$$\tilde{t} = - \frac{\ln \tilde{r}}{\Gamma}. \tag{2.13}$$

In this way $\tilde{t}$ may become infinitely long, which should be avoided as one wishes to observe the ensemble at equidistant time points (the observation points). This is circumvented using an algorithm proposed by Widdershoven (1984a). The probability for an electron to scatter at least once in a time Δt, where Δt is the time interval between the most recent scattering event and the next observation point, reads

$$p(\Delta t) = 1 - \exp(-\Gamma \cdot \Delta t). \tag{2.14}$$

Now a random number $\tilde{r}$ is drawn to decide whether this will happen or not. If $\tilde{r} \le p(\Delta t)$ at least one scattering event will occur and the *same* number is used to calculate the free flight, after which a scatter process is selected. If $\tilde{r} > p(\Delta t)$, the resulting flight would be longer than Δt, so the free flight is assigned a length Δt, followed by a self-scattering.

2.1.2 Selection and performance of the scatter process

A 'real' scatter process j out of N for an electron in a state $\vec{k}$ is selected by choosing the first process j for which

$$\Gamma \cdot \tilde{r} \le \sum_{i=1}^{j} \lambda_i(\vec{k}). \tag{2.15}$$

If $\Gamma \cdot \tilde{r} > \sum_{i=1}^{N} \lambda_i(\vec{k})$ then self-scattering is chosen. A scatter process takes place instantaneously, absorbing no 'electron time' at all. At the observation points the physical quantities of interest (e.g., velocity, kinetic energy) are collected, just *before* the scatter process occurs. In practice, the difference in the value for the estimators taken just before or just after the scattering will be small, because at that particular moment almost always self-scattering will take place.

After a certain scattering process has been selected the new state $\vec{k}'$ has to be determined. The modulus k' is easily calculated from the new kinetic energy W', which is equal to the original kinetic energy plus or minus the energy of the phonon involved. The normalized cumulative distributions $P_\vartheta(\vartheta')$ and $P_\phi(\phi')$ for the angles ϑ and ϕ (see fig. 2.2) needed to determine the spatial orientation of $\vec{k}'$ are derived from eq.(2.5) and given by, respectively,

$$P_\vartheta(\vartheta') = \frac{\frac{V}{(2\pi)^3}\int_0^\infty\int_0^{\vartheta'}\int_0^{2\pi} dk'\ d\vartheta\ d\phi\ k'^2\sin\vartheta\ S(\vec{k},\vec{k}')}{\frac{V}{(2\pi)^3}\int_0^\infty\int_0^{\pi}\int_0^{2\pi} dk'\ d\vartheta\ d\phi\ k'^2\sin\vartheta\ S(\vec{k},\vec{k}')}, \tag{2.16}$$

and

$$P_\phi(\phi') = \frac{\frac{V}{(2\pi)^3}\int_0^\infty\int_0^{\pi}\int_0^{\phi'} dk'\ d\vartheta\ d\phi\ k'^2\sin\vartheta\ S(\vec{k},\vec{k}')}{\frac{V}{(2\pi)^3}\int_0^\infty\int_0^{\pi}\int_0^{2\pi} dk'\ d\vartheta\ d\phi\ k'^2\sin\vartheta\ S(\vec{k},\vec{k}')}. \tag{2.17}$$

The angles are selected with the help of two uniformly distributed random numbers $\tilde{r}_\vartheta$ and $\tilde{r}_\phi$ in $[0,1)$, by

$$\vartheta = P_\vartheta^{-1}(\tilde{r}_\vartheta), \tag{2.18}$$

and

$$\phi = P_\phi^{-1}(\tilde{r}_\phi). \tag{2.19}$$

By choosing a new coordinate system, with the z-axis along $\vec{k}$, the distribution of ϕ becomes uniform, so

$$\phi = 2\pi\tilde{r}_\phi\ . \tag{2.20}$$

The $\tilde{\vartheta}$ is determined in the new system and the $\vec{k}'$ thus obtained must be transformed back to the original system (Boardman 1980).

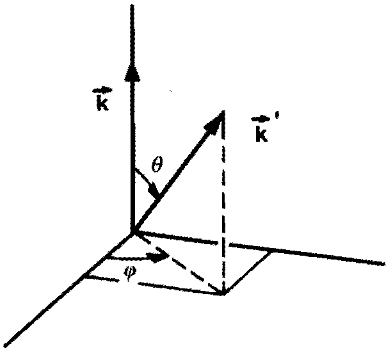

Fig. 2.2 *The scatter angles θ and ϕ necessary to determine the spatial orientation of $\vec{k}'$ with respect to $\vec{k}$.*

2.1.3 Random number generation

In (Ensemble) Monte Carlo calculations a very important role is played by the random number generator. As a true random sequence will be very difficult to realize in practice, pseudo-random sequences have to be produced with the computer. An advantage of sequences produced this way is that experiments become reproducible, which may e.g. be very useful for debugging purposes. A numerical scheme for a pseudo-random number generator, generating a uniform distribution on $[0,m_1/m_2]$ with a theoretical period m_1 is the so-called mixed congruential scheme (Hammersley and Handscomb 1964, Knuth 1969, Graybeal and Pooch 1980)

$$x_{n+1} = \frac{(ax_n + c) \bmod m_1}{m_2} \tag{2.21}$$

where x_0 = the seed (any positive real number),

a = the multiplier (a positive integer),

c = the increment (a positive integer),

m_1 = the period (a positive integer),

m_2 = the scale factor (a positive integer).

The criteria for obtaining an optimal generator with period m_1

have been enumerated by Hammersley and Handscomb (1964), Shreider (1966), Knuth (1969) and Graybeal and Pooch (1980). Widdershoven (1984b) suggested to use a binary multiplication instead of the modulus operation, which yields a faster generator (a factor of 7 faster on an Alliant FX8 computer).

In short, values of $m_1 = 2^k - 1$, where k equals the word size of the computer, and $a = 2^{16} + 3$ are recommended. The reader is referred to the above-mentioned literature for more details on the choice of c. It is sufficient to know that in the present work $c = 907633385$ has been chosen (Widdershoven 1984b).

Both schemes ('modulus' and 'binary') have been tested for different values of x_0, $a = 65539$, $c = 907633385$, $m_1 = 2147483647$ and $m_2 = m_1 + 1$. To begin with, these parameters obey the criteria referred to above. Furthermore, numerous tests have been performed on various aspects of the random generator. Both schemes satisfy the frequency test (Hammersley and Handscomb 1964, Shreider 1966), the serial test (Hammersley and Handscomb 1964), and the Kolmogorov–Smirnov test (Graybeal and Pooch 1980, Shreider 1966), which measure the uniformity, the degree of randomness and the degree of randomness, respectively (Graybeal and Pooch 1980). The period of the 'binary' number generator is found to be $\frac{1}{2}m_2$, whereas for the 'modulus' generator the (theoretical) period is equal to m_1.

It is concluded that for all practical purposes both generators perform satisfactorily. In the present work the 'binary' generator has been used.

Chapter 3

SCATTER PROCESSES

In this chapter the calculation of the scatter rates will be discussed. First the model used for the band structure of GaAs is outlined. After a short introduction of the adiabatic principle (the effective decoupling of ion and electron motion), which allows for a first-order perturbation treatment of the problem, the general expressions needed to calculate the scatter rates will be given. Subsequently, the specific processes are reviewed and the necessary scatter angle selection discussed.

The relevant material parameters for GaAs and AlAs are given in a table in section 3.5, together with the interpolation formulas necessary to obtain the material parameters for $Al_xGa_{1-x}As$.

3.1 Band structure of GaAs

The conduction band of GaAs, see fig. 3.1, is commonly divided into three separate 'valleys' with a Kane-type non-parabolicity (Kane 1957), denoted by Γ-, L- and X-valley, after the locations of their minima at the (000), (111) and (100) symmetry points in the (first) Brillouin zone, see fig. 3.2. There are three equivalent X-valleys and four equivalent L-valleys.

The dispersion relation for each valley, describing the relation between kinetic energy W and wave vector $\vec{k}$, both taken relative to

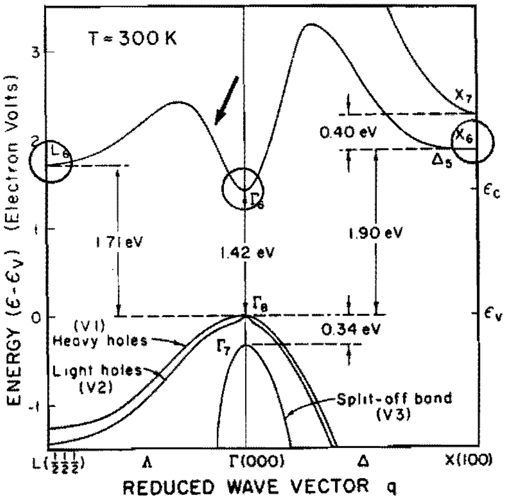

Fig. 3.1 *The energy band for GaAs at room temperature. The conduction band is indicated by the arrow, and the minima serving as valleys are encircled. (Taken from Blakemore, 1982.)*

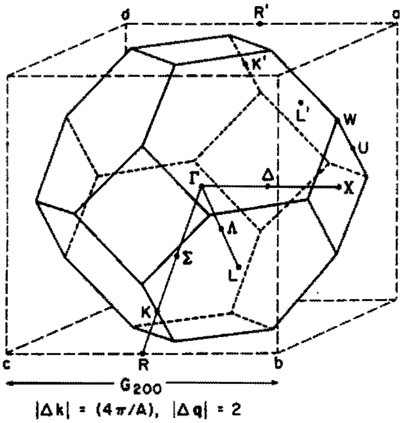

Fig. 3.2 *The first Brillouin zone for GaAs, with the crystallographic names for the various symmetry points. (Taken from Blakemore, 1982.)*

the minimum of the valley, is according to Kane (1957) for III–V compound semiconductors given by

$$W(1 + \alpha W) = \frac{\hbar^2 k^2}{2m^*}, \tag{3.1}$$

where α is the non-parabolicity parameter, and m^* is the effective mass.

In the Γ-valley α_Γ is given by

$$\alpha_\Gamma = \frac{(1 - m_\Gamma^*/m_0)^2}{W_g} , \tag{3.2}$$

where W_g is the direct energy gap between conduction band and valence band, m_Γ^* the effective mass of the electron in the Γ-valley, and m_0 the free-electron rest mass.

In the L- and X-valleys α_L and α_X are chosen such as to fit as closely as possible to the real band structure.

Each electron is in either of the valleys and may transfer from one valley to another under exchange of a phonon, while potential energy is gained or lost as kinetic energy.

The velocity of an electron is found from eq.(1.2) and in the band model described by eq.(3.1) equals

$$\vec{v} = \frac{\hbar\vec{k}}{m^*(1 + 2\alpha W)} . \tag{3.3}$$

3.2 Adiabatic principle

Electron–phonon interaction and interaction of electrons with crystal defects or impurities is easily described in first-order perturbation theory (the Born approximation) owing to the so-called 'adiabatic principle' developed by Born and Oppenheimer (Ziman 1960, Madelung 1978). The quintessence of this approach is the fact that the motions of the fixed ions in the lattice around their equilibrium positions (which motions are characterized by phonon wave vectors with a Bose–Einstein distribution, see eq. 3.5) and the motions of the 'free' conduction electrons are decoupled.

The Hamiltonian for this problem can be divided essentially into two parts, each separately contributing to the energy of the system as a whole. One part describes the movement of electrons in a fixed ion lattice and the other takes care of the movement of the ions in an electron space charge. A residual term, including both electronic and lattice states, accounts for the interaction between electrons and the lattice. The fact that this term, in general, has a low energy eigenvalue compared to the total energy of the system validates the adiabatic principle. This allows for the first-order perturbation theory to be applied, with the perturbing potential being the change in electrostatic potential as faced by the electrons, caused by the lattice vibration, the defect or the impurity. (For a detailed discussion, see Ziman 1960.)

3.3 Transition rate

In general, a free electron in a state $\vec{k}$ is described by the wave function

$$\Psi(\vec{k},\vec{r}) = u_{\vec{k}}(\vec{r}) \exp(i\vec{k}\cdot\vec{r}), \tag{3.4}$$

where $\Psi(\vec{k},\vec{r})$ is called the Bloch function, and $u_{\vec{k}}(\vec{r})$ is periodic on the lattice. For simplicity, here and in the following the band index n is dropped.

Lattice vibrations are described by wave functions $\phi_{n_{\vec{q}}}(\vec{q})$, which are Hermite polynomials, representing a lattice vibration of vector $\vec{q}$ in the $n_{\vec{q}}^{th}$ state of excitation, where $n_{\vec{q}}$ is the Bose–Einstein distribution

$$n_{\vec{q}} = \left[\exp\left(\frac{\hbar\omega_{\vec{q}}}{k_B T} \right) - 1 \right]^{-1} . \qquad (3.5)$$

The combined wave function of electron and phonons is then (Nag 1980)

$$\chi_{n_{\vec{q}}}(\vec{k},\vec{r}) = \Psi(\vec{k},\vec{r}) \prod_{\vec{q}} \phi_{n_{\vec{q}}}(\vec{q}) . \qquad (3.6)$$

The matrix element $M(\vec{k},n_{\vec{q}};\vec{k}',n_{\vec{q}'})$ for the transition from a state described by $\vec{k},n_{\vec{q}}$ to a state $\vec{k}',n_{\vec{q}'}$ is defined as

$$M(\vec{k},n_{\vec{q}};\vec{k}',n_{\vec{q}'}) = < \chi_{n_{\vec{q}}}(\vec{k},\vec{r}) | \mathcal{H}' | \chi_{n_{\vec{q}'}}(\vec{k}',\vec{r}) >$$

$$= \iiint d\vec{r} \;\; \chi^{*}_{n_{\vec{q}}}(\vec{k},\vec{r}) \; \mathcal{H}' \; \chi_{n_{\vec{q}'}}(\vec{k}',\vec{r}) , \qquad (3.7)$$

where $\mathcal{H}'$ is the energy operator for the perturbing potential.

Now, in first-order perturbation theory, the rate of transition from one state to another is given by

$$S(\vec{k},n_{\vec{q}};\vec{k}',n_{\vec{q}'}) = \frac{2\pi}{\hbar} \left| M(\vec{k},n_{\vec{q}};\vec{k}',n_{\vec{q}'}) \right|^2 \delta(W' - W \pm \Delta W) , \qquad (3.8)$$

under the condition that the free time between scatter events is large. The Dirac δ-function takes care of the conservation of energy. This equation is well known as Fermi's Golden Rule.

When an electron is scattered by an impurity the state of the lattice is unaltered, so the wavefunction of interest is just the free-electron Bloch function. In that case the perturbing potential may be expanded in a Fourier series (Nag 1980)

$$\mathcal{H}' = \sum_{\vec{q}} A(\vec{q}) \exp(i\vec{q}\cdot\vec{r}), \qquad (3.9)$$

where $A(\vec{q})$ are Fourier coefficients. The matrix element then becomes

$$M(\vec{k},\vec{k}') = \sum_{\vec{q}} \iiint d\vec{r}\; u^*(\vec{k}',\vec{r}) \exp(-i\vec{k}'\cdot\vec{r})\, A(\vec{q}) \exp(i\vec{q}\cdot\vec{r})\, u(\vec{k},\vec{r}) \exp(i\vec{k}\cdot\vec{r})$$

$$= \sum_{\vec{q}} A(\vec{q})\, \delta_{\vec{q},\vec{k}-\vec{k}'} \iiint d\vec{r}\; u^*(\vec{k}',\vec{r})\, u(\vec{k},\vec{r})$$

$$= A(|\vec{k}-\vec{k}'|)\, I(\vec{k},\vec{k}'), \qquad (3.10)$$

where $I(\vec{k},\vec{k}') = \int d\vec{r}\; u^*(\vec{k}',\vec{r})\, u(\vec{k},\vec{r})$ is referred to as the overlap integral. The condition $\vec{q} = \vec{k} - \vec{k}'$ is analogous to the condition of the conservation of momentum, and $\vec{q}$ plays a role equivalent to that of a phonon wave vector.

For Kane-type conduction bands the square of the overlap integral is called the overlap function $G(\vec{k},\vec{k}')$ and is equal to (Nag 1980)

$$G(\vec{k},\vec{k}') = |I(\vec{k},\vec{k}')|^2$$

$$= (a_k + a_{k'} + c_k c_{k'} \cos\theta)^2, \qquad (3.11)$$

where θ is the angle between $\vec{k}$ and $\vec{k}'$ and

$$a_k = \left(\frac{1 + \alpha W}{1 + 2\alpha W}\right)^{1/2}. \qquad (3.12)$$

$$c_k = \left(\frac{\alpha W}{1 + 2\alpha W}\right)^{1/2}. \qquad (3.13)$$

In case of lattice scattering, the perturbing potential may be expanded as (Ziman 1960, Nag 1980)

$$\mathcal{H}' = \sum_{\vec{q}} A(\vec{q})\, [a_{\vec{q}} \exp(i\vec{q}\cdot\vec{r}) + a^{\dagger}_{\vec{q}} \exp(-i\vec{q}\cdot\vec{r})], \qquad (3.14)$$

where $A(\vec{q})$ is related to the amplitude of the mode of vibration with wave vector $\vec{q}$ and other various material parameters, depending on the kind of vibration. $a_{\vec{q}}$ and $a^{\dagger}_{\vec{q}}$ represent the annihilation and creation operators, respectively.

Substitution leads to

$$M(\vec{k},\vec{k}') = \iiint d\vec{r} \left\{ u^{*}(\vec{k}',\vec{r}) \exp(-i\vec{k}'\cdot\vec{r}) \prod_{\vec{q}} \phi^{*}_{n_{\vec{q}}'}(\vec{q}) \times \sum_{\vec{q}} A(\vec{q}) \right.$$

$$\left. [a_{\vec{q}} \exp(i\vec{q}\cdot\vec{r}) + a^{\dagger}_{\vec{q}} \exp(-i\vec{q}\cdot\vec{r})]\; u(\vec{k},\vec{r}) \exp(i\vec{k}\cdot\vec{r}) \prod_{\vec{q}} \phi_{n_{\vec{q}}'}(\vec{q}) \right\} \qquad (3.15)$$

Analogous to the former case $\iiint d\vec{r} \exp[i(-\vec{k}' + \vec{q} + \vec{k})] = \delta_{\vec{k}',\vec{k}+\vec{q}}$ and $\iiint d\vec{r} \exp[i(-\vec{k}' - \vec{q} + \vec{k})] = \delta_{\vec{k}',\vec{k}-\vec{q}}$, with δ being the Kronecker delta. Also, see e.g. Ziman (1960)

$$< \phi_{n_{\vec{q}}-1}(\vec{q})|\; a_{\vec{q}}\; |\phi_{n_{\vec{q}}}(\vec{q}) > = \sqrt{n_{\vec{q}}}\ , \qquad (3.16)$$

describing a transition from $n_{\vec{q}}$ to $n_{\vec{q}} - 1$, i.e., annihilation of a phonon, and

$$< \phi_{n_{\vec{q}}+1}(\vec{q})|\; a^{\dagger}_{\vec{q}}\; |\phi_{n_{\vec{q}}}(\vec{q}) > = \sqrt{n_{\vec{q}} + 1}\ , \qquad (3.17)$$

describing the creation of a phonon.

Hence, the first term of the integral only has a non-zero value if $\vec{k}' = \vec{k} + \vec{q}$, representing the annihilation (or: absorption) of a phonon with wave vector $\vec{q}$, and the second term leads to the creation (or: emission) of a phonon with wave vector $\vec{q}$ and $\vec{k}' = \vec{k} - \vec{q}$.

In short, the matrix element is written as

$$M(\vec{k},\vec{k}') = A(\vec{q})\; (n_{\vec{q}} + \tfrac{1}{2} \pm \tfrac{1}{2})^{1/2}\; I(\vec{k},\vec{k}'), \qquad (3.18)$$

where the plus sign represents emission, and the minus sign the absorption of a phonon.

The scatter rate for an electron in state $\vec{k}$ to state $\vec{k}'$ is calculated with

$$\lambda(\vec{k}) = \frac{V}{(2\pi)^3} \iiint d\vec{k}' \; S(\vec{k},\vec{k}'), \tag{3.19}$$

where $S(\vec{k},\vec{k}')$ is determined by eq.(3.8) and either eqs.(3.10)–(3.13) or eqs.(3.11)–(3.13), (3.18). This formula is only valid for non-degenerate materials. Otherwise a factor $[1 - f(\vec{k}')]$ (now equal to 1) would have to be included for the probability of $\vec{k}'$ being empty, as will be clear from the scatter term (eq. 1.4) in the Boltzmann transport equation (eq. 1.1). The factor $V/(2\pi)^3$ accounts for the density of states in $\vec{k}$-space. Since the spin is not altered as a consequence of a scatter process it is not necessary to include an extra factor of 2.

Usually, eq.(3.19) is evaluated in a spherical coordinate system. A transformation to spherical coordinates yields

$$d\vec{k}' = k'^2 \sin\theta \; d\theta \; d\phi \; dk', \tag{3.20}$$

after which, because of the conservation of energy present in $S(\vec{k},\vec{k}')$, it is practical to change to W' as an integration variable, i.e.

$$k'^2 \, dk' = \frac{1}{2} \left(\frac{2m^*}{\hbar^2} \right)^{3/2} \gamma'^{\,1/2} \frac{d\gamma'}{dW'} dW', \tag{3.21}$$

where

$$\gamma(W) = W(1 + \alpha W), \tag{3.22}$$

or

$$k' \, dk' = \frac{m^*}{\hbar^2} \frac{d\gamma'}{dW'}. \tag{3.23}$$

3.4 Scatter processes

In III–V cubic semiconductors the phonon lattice vibration dispersion curve essentially consists of two groups, each consisting of one longitudinal and one or two transversal modes, as depicted in fig. 3.3. The low-frequency group represents a kind of lattice vibration where all the pairs of III–V atoms vibrate in phase, and the corresponding phonons are called 'acoustic' phonons because of the similarity with the wave propagation of acoustic waves. The other group represents pairs of III–V atoms vibrating in opposite phase and the phonons involved are referred to as 'polar optical' phonons. Polar, because in GaAs, unlike in silicon, the Ga–As pair carries a dipole moment which is modulated by the optical lattice wave.

Electron–phonon interaction only takes place with longitudinal phonons (Ziman 1960).

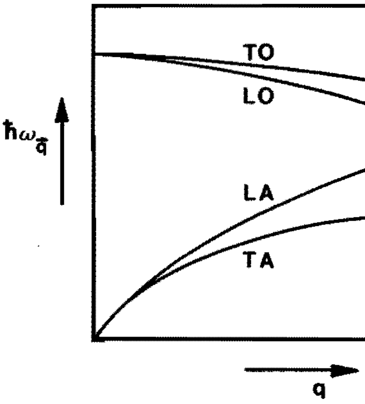

Fig. 3.3 *Schematic representation of the dispersion curve for lattice vibrations, with L(ongitudinal) and T(ransversal) O(ptical) and A(coustic) modes. (After Nag, 1980.)*

3.4.1 Acoustic mode scattering

Acoustic mode scattering is distinguished into two different parts, namely piezo-electric and deformation potential acoustic scattering.

Piezo-electric scattering

The process known as piezo-electric scattering is caused by acoustic phonons of long wavelength. The perturbing potential is proportional to the gradient of the strain caused by the vibrating lattice. As the energy associated with the acoustic phonon is low the process is taken to be elastic, i.e. no phonons are exchanged.

In this approximation, at sufficiently high temperatures, it follows from eq.(3.5)

$$n_{\vec{q}} \cong n_{\vec{q}} + 1 \cong \frac{\hbar\omega_{\vec{q}}}{k_B T} = \frac{\hbar v_s\, |\vec{k}' - \vec{k}|}{k_B T} . \tag{3.24}$$

Note that another approximation is applied in eq.(3.24). This concerns the group velocity of the wave packet for the acoustic phonon. The energies concerned are situated in the lower part of the dispersion curve, where the curve may be approximated by a straight line. The group velocity then becomes

$$\vec{v} = \hbar^{-1}\, \vec{\nabla}_{\vec{q}} \hbar\omega_{\vec{q}} \cong \omega_{\vec{q}}/\vec{q} = v_s , \tag{3.25}$$

where v_s is the velocity of sound in the material.

The transition rate is now given by (Rode 1978, Nag 1980)

$$S(\vec{k},\vec{k}') = 2\,\frac{2\pi}{\hbar}\left(\frac{eP_z}{\epsilon_0\epsilon_s}\right)^2 \frac{k_B T}{2V\rho v_s^2}\,\frac{1}{|\vec{k} - \vec{k}'| + k_d^2}\,\delta(W - W') , \tag{3.26}$$

In determining $S(\vec{k},\vec{k}')$ from the matrix element $M(\vec{k},\vec{k}')$, with eq.(3.18), the overlap integral $I(\vec{k},\vec{k}')$ is taken equal to 1. Absorption and emission are taken together accounting for the first factor of 2. k_d is the inverse Debye length associated with screening,

$$k_d = \left(\frac{e^2 n_e}{\epsilon_0 \epsilon_s k_B T} \right)^{1/2} . \tag{3.27}$$

Hence, from eqs.(3.19) and (3.26)

$$\lambda(W) = \frac{1}{8\hbar^2} \left(\frac{eP_z}{\epsilon_0 \epsilon_s}\right)^2 \frac{k_B T}{\rho v_s^2} \left(\frac{2m^*}{W}\right)^{1/2} \frac{(1 + 2\alpha W)}{\gamma^{1/2}} \ln\left(1 + \frac{8m^*\gamma}{\hbar^2 k_d^2}\right), \tag{3.28}$$

where γ is given by eq.(3.22). P_z is related to the piezo-electric stress tensor and the elastic constants.

With the general formulas (2.16) and (2.18) one finds

$$\cos\vartheta = 1 + \frac{\hbar^2 k_d^2}{4m^*\gamma} \left[1 - \left(1 + \frac{8m^*\gamma}{\hbar^2 k_d^2} \right)^{\tilde{r}} \right], \tag{3.29}$$

while ϕ is randomly distributed over $[0,2\pi)$, and $|\vec{k}'| = |\vec{k}|$.

This scatter process is of a relatively low importance in GaAs at the temperatures considered in this thesis.

Deformation potential scattering

In the deformation potential interaction of electrons with long-wavelength acoustic modes the perturbing potential is proportional to the strain produced by these vibrations.

Analogous to the former case the process is taken to be elastic with the energy of the associated phonon low enough to ensure the validity of eq.(3.24) again. The transition rate is (Rode 1978)

$$S(\vec{k},\vec{k}') = 2\,\frac{2\pi}{\hbar}\,\frac{D_a^2\,k_BT}{2V\rho v_s^2}\,G(\vec{k},\vec{k}')\,\delta(W - W'), \tag{3.30}$$

and

$$\lambda(W) = \frac{(2m^*)^{3/2}\,D_a^2\,k_BT}{2\pi\hbar^4\rho v_s^2}\,[W(1 + \alpha W)]^{1/2}\left[\frac{(1 + \alpha W)^2 + \frac{1}{3}\,\alpha^2W^2}{(1 + 2\alpha W)}\right]. \tag{3.31}$$

Here $|\vec{k}'| = |\vec{k}|$, $\phi = 2\pi\tilde{r}$ and

$$\cos\theta = \left\{\frac{[(1 + 2\alpha W)^3(1 - \tilde{r}) + \tilde{r}]^{1/3} - 1}{\alpha W} - 1\right\}. \tag{3.32}$$

This process is of a relatively low importance in GaAs at the temperatures considered in this thesis.

3.4.2 Optical mode scattering

Optical mode scattering consists of two different parts, a polar and a non-polar one.

Polar mode scattering

The dominant scatter mechanism in III–V compound semiconductors near room temperature is associated with the electric polarization caused by the optical mode vibration. It is an inelastic process, as the energy associated with the optical phonon cannot be neglected compared with k_BT, like with acoustic mode scattering.

The transition rate is (Rode 1978)

$$S(\vec{k},\vec{k}') = \frac{2\pi}{\hbar}\,\frac{2\pi e^2\hbar\omega_o}{4\pi\epsilon_0V}\left(\frac{1}{\epsilon_\infty} - \frac{1}{\epsilon_s}\right)\frac{G(\vec{k},\vec{k}')}{|\vec{k} - \vec{k}'|^2}\,(n_{\vec{q}} + \tfrac{1}{2} \pm \tfrac{1}{2})\,\delta(W' - W \pm \hbar\omega_o), \tag{3.33}$$

where the plus sign denotes the emission of and the minus sign the absorption of a phonon with wave vector $\vec{k} - \vec{k}'$ and energy $\hbar\omega_o$. The longitudinal optical phonon energy is assumed a constant, since the optical branch of the frequency spectrum has a zero gradient at $\vec{q} = 0$ and only phonons having small $\vec{q}$ can interact with electrons in semiconductors (Ehrenreich 1957). The value of ω at the centre of the first Brillouin zone is taken to be the constant ω_o. $n_{\vec{q}}$ is again the Bose-Einstein distribution (eq. 3.5), with $\omega_{\vec{q}} = \omega_o$.

The scatter rate now is given by

$$\lambda(W) = \frac{(2m^*)^{1/2}\, e^2\omega_o}{8\pi\epsilon_0\hbar}\left(\frac{1}{\epsilon_\infty} - \frac{1}{\epsilon_s}\right)(1 + 2\alpha W')\frac{F(W,W')}{\gamma^{1/2}}(n_{\vec{q}} + \tfrac{1}{2} \pm \tfrac{1}{2}), \qquad (3.34)$$

where $W' = W \pm \hbar\omega_o$, and

$$F(W,W') = \frac{1}{C}\left[A \ln\left|\frac{\gamma^{1/2} + \gamma'^{1/2}}{\gamma^{1/2} - \gamma'^{1/2}}\right| + B\right], \qquad (3.35)$$

$$A = [2(1 + \alpha W)(1 + \alpha W') + \alpha(\gamma + \gamma')]^2, \qquad (3.36)$$

$$B = -2\alpha(\gamma\gamma')^{1/2}\,[4(1 + \alpha W)(1 + \alpha W') + \alpha(\gamma + \gamma')], \qquad (3.37)$$

$$C = 4(1 + \alpha W)(1 + \alpha W')(1 + 2\alpha W)(1 + 2\alpha W'). \qquad (3.38)$$

The scatter angle ϑ is not easily evaluated since from eqs.(2.16) and (2.18) an expression is obtained which is not analytically solvable. Widdershoven (1984a) has developed a method to obtain ϑ from this expression with the help of random numbers. Again ϕ is randomly distributed over $[0,2\pi)$.

This process is very important at the temperatures considered in this thesis (77 K and 300 K), and the rate of occurrence is practically independent of energy (except for a threshold for the emission of phonons). It is not a very efficient process, in that it favours small scatter angles. This means that, on the average, velocity is not dramatically changed as a consequence of this process.

Non-polar mode scattering

In the L-valley not only scattering by polar optical phonons occurs but also by non-polar optical phonons. This scatter process is caused by a deformation potential, and the transition rate is given by (Fawcett et al. 1970, Rode 1978)

$$S(\vec{k},\vec{k}') = \frac{2\pi}{\hbar}\,\frac{\hbar D_o^2}{2V\rho\omega_{no}}\,G(\vec{k},\vec{k}')\,(n_{\vec{q}} + \tfrac{1}{2} \pm \tfrac{1}{2})\,\delta(W' - W \pm \hbar\omega_{no}), \qquad (3.39)$$

where the plus sign denotes emission and the minus sign the absorption of a phonon with wave vector $\vec{k} - \vec{k}'$ and energy $\hbar\omega_{no}$. D_o is the optical deformation potential.

The resulting scatter rate is

$$\lambda(W) = \frac{(2m^*)^{3/2}\,D_o^2}{4\pi\hbar^2\rho\hbar\omega_{no}}\,[W'(1 + \alpha W')]^{1/2} \times$$

$$\left[\frac{(1 + \alpha W)(1 + \alpha W') + \frac{1}{3}\alpha^2 WW'}{1 + 2\alpha W}\right]. \qquad (3.40)$$

As there is no dependency on ϕ, the angle $\phi = 2\pi\tilde{r}$, and

$$\cos\theta = \{\,[(b + c)^3 - 2c(3b^2 + c^2)\tilde{r}]^{1/3} - b\,\}\,/\,c, \qquad (3.41)$$

with

$$b = \left(\frac{1 + \alpha W}{1 + 2\alpha W}\right)^{1/2}\left(\frac{1 + \alpha W'}{1 + 2\alpha W'}\right)^{1/2}, \qquad (3.42)$$

and

$$c = \left(\frac{\alpha W}{1 + 2\alpha W}\right)^{1/2}\left(\frac{\alpha W'}{1 + 2\alpha W'}\right)^{1/2}. \qquad (3.43)$$

This process is of a relatively low importance in GaAs at the temperatures considered in this thesis.

3.4.3 *Intervalley scattering*

Associated with the three-valley model of the conduction band structure are the possibilities of equivalent and non-equivalent intervalley scattering. In the first process an electron scatters between different L- or X-valleys and remains in the same type of valley. As a result of the second process an electron transfers from a valley of any type to another valley of different type. These are again processes caused by a deformation potential.

The transition rate for an electron transferring from valley i to valley j is given by (Fawcett et al. 1970)

$$S(\vec{k},\vec{k}') = (Z_j - \delta_{ij}) \frac{D_{ij}^2}{8\pi^2 \rho\omega_{ij}} G_{ij}(\vec{k},\vec{k}')(n_{ij,\vec{q}} + \tfrac{1}{2} \pm \tfrac{1}{2}) \times$$

$$\delta(W'_j + \Delta_j - W_i - \Delta_i \pm \hbar\omega_{ij}), \qquad (3.44)$$

where

$$G_{ij}(\vec{k},\vec{k}') = \left(\frac{1 + \alpha_i W_i}{1 + 2\alpha_i W_i} \right) \left(\frac{1 + \alpha_j W'_j}{1 + 2\alpha_j W'_j} \right), \qquad (3.45)$$

and $n_{\vec{q}}$ is the Bose—Einstein distribution (eq. 3.5) with $\omega_{\vec{q}} = \omega_{ij}$. Z_{ij} denotes the number of equivalent valleys j, being equal to 1 for the Γ-valley, 4 for the L-valley and 3 for the X-valley. The plus sign stands for emission, the minus sign for absorption of a intervalley phonon. The wave vectors $\vec{k}$ and $\vec{k}'$, and the energies W and W′ are taken relative to the bottom of the valley concerned, whereas Δ_i and Δ_j denote the energy level of the bottom of the valley concerned relative to the bottom of the Γ-valley.

This yields for the total scatter rate

$$\lambda(W) = \frac{(Z_j - \delta_{ij})(2m_j^*)^{3/2} D_{ij}^2}{2\pi\hbar^2 \rho\hbar\omega_{ij}} \gamma_j'^{1/2} (1 + 2\alpha_j W') G_{ij}(\vec{k},\vec{k}')\times$$

$$(n_{ij,\vec{q}} + \tfrac{1}{2} \pm \tfrac{1}{2}), \tag{3.46}$$

$$W' = W_i + \Delta_i - \Delta_j \mp \hbar\omega_{ij}. \tag{3.47}$$

As there is no explicit dependence on ϑ in $S(\vec{k},\vec{k}')$ ϑ is easily evaluated as

$$\vartheta = \arccos(1 - 2\tilde{r}). \tag{3.48}$$

and $\phi = 2\pi\tilde{r}$.

This process is of great importance at fields higher than ± 2 kV/cm, especially at out-of-equilibrium conditions, just after (in the order of picoseconds) an electric field change has occurred. It has a randomizing effect on the velocity, which can be understood from eq.(3.48).

3.4.4 Random potential alloy scattering

A scatter process which can only be present in ternary and quaternary alloys is the one arising from the random arrangement of the atoms in the alloy on the lattice sites. In the following only the case for ternary alloys is treated.

A ternary alloy $A_xB_{1-x}C$ can be imagined to be constructed of the two binary compounds AC and BC. The B-atoms substituting the A-atoms in the AC lattice, or alternatively the A-atoms substituting the B-atoms in the BC lattice, cause a local disturbance in the lattice potential. This disturbance is used as the scatter potential in evaluating the matrix element in a first-order perturbation treatment.

For an alloy with non-parabolic energy bands the transition rate is given by (Harrison and Hauser 1976, Littlejohn et al. 1978)

$$S(\vec{k},\vec{k}') = \frac{2\pi}{\hbar} \frac{3\pi^2}{16V} \Omega\, x(1 - x)\, \gamma^{1/2} \frac{d\gamma}{dW} |\Delta U|^2 S_o\, \delta(W - W'), \qquad (3.49)$$

where Ω is the volume of the primitive cell of the alloy, being $a^3/4$ where a is the lattice constant, and ΔU is the scatter potential. S_o is a parameter describing the degree of disorder: if $S_o = 0$ the order is perfect (a superlattice) and if $S_o = 1$ the atoms are randomly distributed and the disorder is at its maximum.

Hence, the scatter rate is

$$\lambda(W) = \frac{3\pi(m^*)^{3/2}}{8\ 2^{1/2}\hbar^4} \Omega\, x(1 - x)\, \gamma^{1/2} \frac{d\gamma}{dW} |\Delta U|^2 S_o, \qquad (3.50)$$

where $|\vec{k}'| = |\vec{k}|$, and θ is selected with eq.(3.48) and $\phi = 2\pi\tilde{r}$.

The value of the scatter potential ΔU is still subject to debate. Harrison and Hauser (1976) give three possible candidates, among which the energy bandgap difference and the electron affinity difference of the binary compounds AC and BC. For AlGaAs, values of 0.49 eV or 1.51 eV ,respectively ,result. These two values yield substantially different scatter rates! For fundamental reasons Harrsion and Hauser have chosen the difference in electron affinities as the scatter potential.

Recently, measurements by Saxena (1985) indicate an x-dependence of ΔU, with e.g. values of 1.6 eV and 1.2 eV for x=0.2 and x=0.3, respectively. However, these values yield mobilities in Ensemble Monte Carlo calculations which are not in accordance with measurements, as shown by Thobel (1988). Therefore, in this work the approach as suggested by Harrison and Hauser is followed.

In InGaAs and InGaAsP there is a considerable influence on mobility as a result of this process. However, in the AlGaAs ternary compound the importance of this process is limited.

3.4.5 Ionized impurity scattering

Usually the approach followed for scattering by ionized impurities is the one by Brooks–Herring (Chattopadhyay and Queisser 1981). Herein a screened Coulomb potential (or: Yukawa potential) is used in connection with first-order perturbation theory to arrive at the scatter rate. The potential energy of an electron in the field of an ionized impurity with charge e at distance r is

$$V(r) = \frac{e^2}{4\pi\epsilon_0\epsilon_s r}\exp(-k_d r), \tag{3.51}$$

where k_d, the inverse Debye length, is given by eq.(3.27). As depicted in section 3.3 no lattice states are involved, so the matrix element is the Fourier transform of the potential energy, and

$$S(\vec{k},\vec{k}') = \frac{2\pi}{\hbar}\left(\frac{e}{V\epsilon_0\epsilon_s}\right)^2 \frac{G(\vec{k},\vec{k}')}{(k_d^2 + |\vec{k} - \vec{k}'|^2)^2}\,\delta(W - W'). \tag{3.52}$$

The scatter rate is obtained by integrating over the final states $\vec{k}'$ and subsequently summing over all impurities, i.e. multiplication with N_iV, where N_i is the impurity concentration and V the volume of the crystal. Neglecting non-parabolicity and putting $G(\vec{k},\vec{k}')$ equal to 1 (Kaszynski 1979) it follows that

$$\lambda(k) = \frac{e^4 m^* N_i}{4\pi(\epsilon_0\epsilon_s)^2\hbar^3 k_d^2 k[1 + (2k/k_d)^{-2}]}. \tag{3.53}$$

In the following an alternative approach is outlined, as developed by Ridley (1977) and subsequently adapted for Monte Carlo purposes by Van de Roer and Widdershoven (1986).

Classically the scatter rate is calculated from (Seeger 1973)

$$\lambda(\vec{k}) = N_i \sigma_c v(\vec{k})$$

$$= N_i \pi b_m^2 v, \tag{3.54}$$

where σ_c is the crosssection and b_m the maximum impact parameter. The cross-section is calculated from the differential cross-section $\sigma(\theta)$ by

$$\sigma_c = 2\pi \int_0^{\pi} d\theta \; \sigma(\theta) \; \sin\theta \; , \tag{3.55}$$

where θ is the angle of deflection of the particle from its original direction of motion.

In the Brooks–Herring model the range of the scatter potential is limited to $1/k_d$ (screening length), by introducing the exponential factor to the Coulomb potential, and the interaction is considered to take place between two bodies, viz. the impurity and the electron. However, if the average distance between the scatter centres is smaller than the screening length more centres can play a role and the Brooks–Herring approach is in error because it simply adds the effects of all these centres.

In the Conwell–Weisskopf model (Conwell and Weisskopf 1950, Chattopadhyay and Queisser 1981) this problem has been circumvented by cutting off the Coulomb field at a distance equal to half the average distance of the impurities.

The two models have in common that they both define a range for the scatter potential in which only one centre is active. Ridley (1977) proposed to refine these models by introducing the probability that indeed no second scatter centre is present in a cylinder with radius b (the impact parameter),

$$b = 2\pi \int_{\vartheta}^{\pi} d\vartheta' \sigma(\vartheta') \sin\vartheta' , \tag{3.56}$$

and length $a = N_i^{-1/3}$, this probability being

$$p(b) = \exp(-\pi b^2 N_i a). \tag{3.57}$$

If a second scatter centre would be present it would be closer to the electron and the first centre would become ineffective in this model. It is asssumed that at any time an electron can be scattered only by the ion nearest to it. Thus

$$\sigma_R(\vartheta) = \sigma_{BH}(\vartheta) \exp(-\pi a b^2 N_i)$$

$$= \sigma_{BH}(\vartheta) \exp\left(-aN_i \int_{\vartheta}^{\pi} d\vartheta' \ \sigma_{BH}(\vartheta') \sin\vartheta'\right). \tag{3.58}$$

Now the scatter rate is found by (eqs. 3.54, 3.55)

$$\lambda(W) = N_i 2\pi v \int_0^{\pi} d\vartheta \ \sigma_R(\vartheta) \sin\vartheta. \tag{3.59}$$

After integration this yields

$$\lambda(W) = N_i^{1/3} v(\vec{k}) \left[1 - \exp\left(\frac{\lambda_{BH}(\vec{k})}{N_i^{1/3} v(\vec{k})} \right) \right], \tag{3.60}$$

which is equal to

$$\lambda(W) = \frac{\hbar k}{2m^*(1 + 2\alpha W)} \left[1 - \exp\left(- \frac{aN_i m^{*2} e^4 (1 + 2\alpha W)}{\pi \hbar^4 (\epsilon_0 \epsilon_s)^2 k_d^2 \ (4k^2 + k_d^2)} \right) \right]. \tag{3.61}$$

Now, the angle selection has to be performed.

First, from eqs.(2.16) and (2.18), the angle ϑ_R may be found by

$$\tilde{u} = \frac{N_i 2\pi v \int_{\vartheta_R}^{\pi} d\vartheta' \;\; \sigma_R(\vartheta')\sin\vartheta'}{N_i 2\pi v \int_{0}^{\pi} d\vartheta' \;\; \sigma_R(\vartheta')\sin\vartheta'}$$

$$= \frac{1 \;-\; \exp(-N_i^{2/3} \int_{\vartheta_R}^{\pi} d\beta \; 2\pi\sin\beta \;\; \sigma_{BH}(\beta)}{1 \;-\; \exp\left(-\, \dfrac{\lambda_{BH}(\vec{k})}{N_i^{1/3} v(\vec{k})}\right)}$$

$$= \frac{1 \;-\; \exp(-N_i a\pi r^2)}{1 \;-\; \exp(-N_i a\pi r_m^2)} \;, \qquad (3.62)$$

with

$$\lambda_{BH}(\vec{k}) = N_i 2\pi v(\vec{k}) \int_{0}^{\pi} d\vartheta' \;\; \sigma_{BH}(\vartheta') \; \sin\vartheta'$$

$$= N_i v \pi r_m^2, \qquad (3.63)$$

and

$$\pi r^2 = 2\pi \int_{\vartheta_R}^{\pi} d\vartheta' \;\; \sigma_{BH}(\vartheta') \; \sin\vartheta' \qquad (3.64)$$

It follows from eq.(3.62) that

$$\frac{r^2}{r_m^2} = -\, \frac{a^2}{\pi r_m^2} \ln\left[1 \;-\; \tilde{u} + \tilde{u}\, \exp\left(-\, \frac{\pi r_m^2}{a^2}\right)\right]. \qquad (3.65)$$

Having found r^2/r_m^2, by drawing a random number $\tilde{u}$, ϑ_R is found by solving eq.(3.64), which eventually results in (Van de Roer and Widdershoven 1986)

$$\cos\vartheta_R(r^2/r_m^2) = \left(1 \;-\; \frac{2(1 \;-\; r^2/r_m^2)}{1 + 4\; r^2 k^2/(r_m^2 k_d^2)}\right). \qquad (3.66)$$

At ionized impurity densities higher than 10^{16} cm^{-3} at 77 K and

$5 \cdot 10^{17}$ cm^{-3} at 300 K this process comes into play. It is a very important factor in limiting the velocity, especially at fields up to 7 kV/cm. See chapter 4 for results.

3.4.6 Electron—electron scattering

At electron densities in the order of 10^{16} cm^{-3} and higher the Coulomb repulsion between electrons comes into play. An electron in state $\vec{k}_1$ is scattered into state $\vec{k}'_1$ by an electron in state $\vec{k}_2$ which itself is scattered into state $\vec{k}'_2$. Following the approach of Ziman (1960), a screened Coulomb potential analogous to eq.(3.51)

$$V(r) = - \frac{e^2}{4\pi\epsilon_0\epsilon_s r} \exp(-k_d r) \qquad (3.67)$$

is used as the energy operator $\mathcal{H}'$ in combination with first-order perturbation theory. The matrix element then becomes

$$<\vec{k}_1,\vec{k}_2|\mathcal{H}'|\vec{k}'_1,\vec{k}'_2> = \frac{e^2}{V\epsilon_0\epsilon_s} \frac{\delta_{\vec{k}_1+\vec{k}_2,\vec{k}'_1+\vec{k}'_2}}{|\vec{k}'_1-\vec{k}_1|^2 + k_d^2} \ . \qquad (3.68)$$

The scatter rate is obtained from Takenaka et al. (1979)

$$\lambda(\vec{k}_1) = \sum_{\vec{k}'_1} \sum_{\vec{k}_2} \sum_{\vec{k}'_2} \frac{2\pi}{\hbar} \left(\frac{e^2}{V\epsilon_0\epsilon_s}\right) \left(\frac{\delta_{\vec{k}_1+\vec{k}_2,\vec{k}'_1+\vec{k}'_2}}{|\vec{k}'_1-\vec{k}_1|^2 + k_d^2}\right)^2 \times$$

$$f(\vec{k}_2)[1 - f(\vec{k}'_1)][1 - f(\vec{k}'_2)] \ \delta(W_1 + W_2 - W'_1 - W'_2). \qquad (3.69)$$

Under the assumption that the probabilities $f(\vec{k}'_1)$ and $f(\vec{k}'_2)$ for $\vec{k}'_1$ and $\vec{k}'_2$ being occupied are practically equal to zero, the scatter rate becomes

$$\lambda(\vec{k}_1) = \iiint d\vec{k}_2 \; f(\vec{k}_2) \; \frac{n_e m^* e^4 |\vec{k}_1 - \vec{k}_2|}{4\pi\hbar^3 (\epsilon_0 \epsilon_s)^2 k_d^2 (k_d^2 + |\vec{k}_1 - \vec{k}_2|^2)} \, , \qquad (3.70)$$

where n_e denotes the electron density.

This expression has been derived for the case of parabolic bands, where both wave vector and energy are conserved, i.e. $\vec{k}_1 + \vec{k}_2 = \vec{k}'_1 + \vec{k}'_2$ and $W_1 + W_2 = W'_1 + W'_2$. It has proved useful to work with $\vec{g}$ and $\vec{g}'$, where $\vec{g} = \vec{k}_2 - \vec{k}_1$ and $\vec{g}' = \vec{k}'_2 - \vec{k}'_1$. The angle ϑ between $\vec{g}$ and $\vec{g}'$ is given by Matulionis et al. (1975)

$$\cos\vartheta = 1 - \frac{2r}{1 + g^2(1 - r)/k_d{}^2}, \qquad (3.71)$$

where $\vec{g} = |\vec{g}_1| = |\vec{g}_2|$. The azimuthal angle ϕ is randomly distributed over $[0,2\pi)$ and

$$\vec{k}'_1 = \vec{k}_1 - (\vec{g}' - \vec{g})/2. \qquad (3.72)$$

For the selection of the electron–electron scattering process a rejection scheme is used owing to Brunetti et al. (1985). When in the Ensemble Monte Carlo calculations this process is selected for the electron under consideration, the other electron necessary is randomly selected from the ones left.

This process has a thermalizing effect and has an increasing effect on the velocity, see chapter 4 for further details.

3.5 Material parameters

In the following table the material parameters for GaAs and AlAs are collected, together with the interpolation formulas necessary to obtain the parameters for $Al_xGa_{1-x}As$.

Table 3.1 *Material parameters for GaAs, AlAs and* Al_xGa_yAs*, where* $y = 1 - x$.

GaAs	AlAs	Al_xGa_yAs
	lattice constant (Å)	
$a_G = 5.642$	$a_A = 5.661$	$a_{AG} = xa_A + ya_G$
	density (kg/m^3)	
$d_G = 5360$	$d_A = 3598$	$d_{AG} = \dfrac{xd_Aa_A^3 + yd_G^3a_G}{a_{AG}^3}$
	longitudinal polar optical phonon energy (eV)	
$\hbar\omega_{LO,G} = .03536$	$\hbar\omega_{LO,A} = .05$	
	$\hbar\omega_{LO,AG} = \left[\dfrac{\epsilon_{s,AG}}{\epsilon_{\infty,AG}} \left(x\dfrac{\epsilon_{\infty,A}}{\epsilon_{s,A}} \hbar^2\omega_{LO,A}^2 + y\dfrac{\epsilon_{\infty,G}}{\epsilon_{s,G}} \hbar^2\omega_{LO,G}^2 \right) \right]^{1/2}$	
	acoustic wave velocity (m/s)	
$V_G = 5240$	$v_A = 5820$	
$H_A = \dfrac{\epsilon_{\infty,A}}{\epsilon_{s,A}} \hbar^2\omega_{LO,A}^2$	$H_G = \dfrac{\epsilon_{\infty,G}}{\epsilon_{s,G}} \hbar^2\omega_{LO,G}^2$	$B = \left(\dfrac{d_A}{d_G} \right) \left(\dfrac{a_A}{a_G} \right)^3$
$C = \left(\dfrac{v_G}{a_G} \right)^2$	$A = \left(\dfrac{v_A}{a_A} \right)^2$	$D = BAH_G + \dfrac{CH_A}{B}$
		$VN = x^2AH_A + xyD + y^2CH_G$ $VD = xH_A + yH_G$ $v_{AG} = a_{AG} \sqrt{\dfrac{VN}{VD}}$

Table 3.1 *continued*

	static dielectric constant	
$\epsilon_{s,G} = 12.9$	$\epsilon_{s,A} = 10.9$	
$F_G = \frac{\epsilon_{s,G} - 1}{\epsilon_{s,G} + 2}$	$F_A = \frac{\epsilon_{s,A} - 1}{\epsilon_{s,A} + 2}$	$F_{AG} = xF_A + yF_G$
		$\epsilon_{s,AG} = \frac{1 + 2F_{AG}}{1 - F_{AG}}$
	acoustic deformation potential energy (eV)	
$D_{\Gamma,G} = 7.0$	$D_{\Gamma,A} = 12.2$	for each valley:
$D_{L,G} = 9.2$	$D_{L,A} = 12.5$	$D_{AG} = xD_A + yD_G$
$D_{X,G} = 9.27$	$D_{X,A} = 9.5$	
	effective mass (kg)	
$m^*_{\Gamma,G} = .063m_0$	$m^*_{\Gamma,A} = .14m_0$	for each valley:
$m^*_{L,G} = .222m_0$	$m^*_{L,A} = .24m_0$	$m_{AG} = \frac{m_G m_A}{xm_G + ym_A} m_0$
$m^*_{X,G} = .58m_0$	$m^*_{X,A} = .37m_0$	
	non-parabolicity parameter (eV^{-1})	
$\alpha_{\Gamma,G} = .61$	$\alpha_{\Gamma,A} = .251$	$\alpha_{\Gamma,AG} = \frac{(1 - m^*_{\Gamma,AG}/m_0)^2}{W_{g,\Gamma,AG}}$
$\alpha_{L,G} = .461$	$\alpha_{L,A} = .57$	for the L- and X-valley:
$\alpha_{X,G} = .204$	$\alpha_{X,A} = .251$	$\alpha_{AG} = y\alpha_G + x\alpha_A$

Table 3.1 *continued*

	intervalley coupling constant (eV/m)	
$D_{\Gamma L,G} = 10^{11}$	$D_{\Gamma L,A} = 5\cdot10^{10}$	for each coupling constant:
$D_{\Gamma X,G} = 10^{11}$	$D_{\Gamma X,A} = 10^{11}$	
$D_{LL,G} = 10^{11}$	$D_{LL,A} = 5\cdot10^{10}$	$D_{AG} = xD_A + yD_G$
$D_{LX,G} = 5\cdot10^{10}$	$D_{LX,A} = 5\cdot10^{10}$	
$D_{XX,G} = 7\cdot10^{10}$	$D_{XX,A} = 10^{11}$	
	intervalley phonon energy (eV)	
$\hbar\omega_{\Gamma L,G} = .0278$	$\hbar\omega_{\Gamma L,A} = .0413$	
$\hbar\omega_{\Gamma X,G} = .0299$	$\hbar\omega_{\Gamma X,A} = .0473$	for each energy:
$\hbar\omega_{LL,G} = .029$	$\hbar\omega_{LL,A} = .044$	$\hbar\omega_{AG} = x\hbar\omega_A + y\hbar\omega_G$
$\hbar\omega_{LX,G} = .0293$	$\hbar\omega_{LX,A} = .0473$	
$\hbar\omega_{XX,G} = .0299$	$\hbar\omega_{XX,A} = .0473$	
	forbidden gap (eV)	
$W_{g,\Gamma,G} = 1.439$	$W_{g,\Gamma,A} = 2.964$	$W_{g,\Gamma,AG} = 1.439 + 1.087x + 0.438x^2$
$W_{g,L,G} = 1.769$	$W_{g,L,A} = 2.464$	$W_{g,L,AG} = 1.769 + 0.695x$
$W_{g,X,G} = 1.961$	$W_{g,X,A} = 2.221$	$W_{g,X,AG} = 1.961 + 0.1x + 0.16x^2$

Table 3.1 *continued*

	high-frequency dielectric constant	
$\epsilon_{\infty,G} = 10.92$	$\epsilon_{\infty,A} = 8.5$	
$F_G = \dfrac{(\epsilon_{\infty,G} - 1)}{(\epsilon_{\infty,G} + 2)}$	$F_A = \dfrac{(\epsilon_{\infty,A} - 1)}{(\epsilon_{\infty,A} + 2)}$	$F_{AG} = xF_A + yF_G$ $\epsilon_{\infty,AG} = \dfrac{(1 + 2F_{AG})}{(1 - F_{AG})}$
	electron affinity (eV)	
$\chi_{e,G} = 4.07$	$\chi_{e,A} = 3.58$	$\chi_{e,AG} = x\chi_{e,A} + y\chi_{e,G}$
	piezoelectric constant (C/m^2)	
$P_{z,G} = 0.16$	$P_{z,A} = 0.1$	$P_{z,AG} = \dfrac{xP_{z,A}\epsilon_{s,A}a_A^2 + yP_{z,G}\epsilon_{s,G}a_G^2}{\epsilon_{s,AG}(a_{AG})^2}$
	optical deformation potential (eV/m)	
$D_{o,\Gamma,G} = 0$ $D_{o,L,G} = 3 \cdot 10^{10}$ $D_{o,X,G} = 0$	$D_{o,\Gamma,A} = 0$ $D_{o,L,A} = 3 \cdot 10^{10}$ $D_{o,X,A} = 0$	for each valley: $D_{o,AG} = xD_{o,A} + yD_{o,G}$
	optical phonon energy (eV)	
$\hbar\omega_{o,G} = 0.0343$	$\hbar\omega_{o,A} = 0.0475$	$\hbar\omega_{o,AG} = x\hbar\omega_{o,A} + y\hbar\omega_{o,G}$

The values and formulas have been compiled by Williams and Glisson (1985). A review with values for material parameters for GaAs has been published by Blakemore (1982) and a review with interpolation formulas for $Al_xGa_{1-x}As$ has been written by Adachi (1985).

3.6 Additional remarks

It should be remarked that in the treatment of the scatter processes in this chapter only static screening is taken into account. The term accounting for static screening is found from the highly complex dielectric function $\epsilon(\vec{q},\omega)$, by setting $\omega=0$. For a complete description of the dielectric function, also called the Lindhard function, see e.g. Madelung (1978).

The Fourier transform of the screened scatter potential, $U_F(\vec{q})$, is found from the Fourier tranform of the unscreened potential, $V_F(\vec{q})$, through

$$U_F(\vec{q}) = \frac{V_F(\vec{q})}{\epsilon(\vec{q},\omega)} . \tag{3.73}$$

In the case of static screening, when $\omega=0$,

$$\epsilon(\vec{q},0) = 1 + \lambda_D/q^2, \tag{3.74}$$

where λ_D is the Debye wavelength, and screening is easily introduced with eqs.(3.73) and (3.74). This approach has (implicitly) been followed in the calculation of the scatter rates for piezo-electric scattering, ionized impurity scattering and electron–electron scattering.

Dynamic screening ($\omega \neq 0$) corresponding to inelastic scattering processes, requires a more complex description of the dielectric function. The inclusion of a frequency-dependent dielectric function, and thereby of dynamic screening, in the calculation of the scatter rates lies outside the scope of this thesis.

Another problem, associated with the dielectric function, is the treatment of electron–plasmon scattering (Lugli and Ferry 1985). In this process, an electron is scattered by collective excitations of the electron gas. These excitations are known as the plasma oscillations and the energy quantum of these movements is called 'plasmon'.

To describe this process, the Coulomb part of the Hamiltonian for the electron gas is split into two parts by the introduction of a cut-off wave vector q_c. For wavelengths above $1/q_c$ the collective-mode scattering dominates (electron–plasmon scattering), below $1/q_c$ the 'binary' electron–electron scattering term as described in section 3.4.6 prevails.

The value of q_c is obtained from an analysis of the singularities of the dielectric function, and equals roughly $1/(2\lambda_D)$.

The importance of electron–plasmon scattering in bulk GaAs relative to the electron–electron scattering from section 3.4.6 is not clear from the published work by Lugli and Ferry. Both processes taken together yield a minor influence on the steady-state velocity, although on short time scales and in the form of the distribution function a considerable influence appears. Actually, the same conclusions approximately apply to electron–electron scattering alone (see chapter 4).

For this reason and the fact that it only comes into play at wavelengths higher than twice the Debye wavelength, it seems reasonable to neglect electron–plasmon scattering at first instance.

Chapter 4

ELECTRON TRANSPORT IN HIGHLY DOPED GaAs

In this chapter results are presented of Ensemble Monte Carlo calculations of electron transport in bulk GaAs at temperatures of 77 K and 300 K. First results will be shown for the case in which the semiconductor is undoped and the conduction electrons only arise from thermal generation. These results are used to check the Monte Carlo program. As the electron density increases with increasing doping densities, the Pauli exclusion principle becomes more important as well as interelectronic collisions (electron–electron scattering). The main purpose of the present chapter is to study the influence of the two latter mechanisms on transport properties. This has been done in detail by alternatingly turning them on or off, while the scattering by ionized impurities is taken into account in all cases.

The results are presented in plots of the velocity, the energy, and the valley occupancy as a function of the electric field. In all simulations the following scatter processes (see chapter 3) have been taken into account in the physical model:

elastic acoustic phonon scattering (ACe),
piezoelectric scattering (PE),
polar and non-polar optical phonon scattering (resp. POPA, POPE and NPOPA, NPOPE),
equivalent and non-equivalent intervalley scattering (resp. L-LA,

L-LE, X-XA, X-XE, and g-LA, g-LE, g-XA, g-XE, L-XA, L-XE).

The abbreviations between brackets are employed in tables to be presented. The 'A' denotes a process where absorption and 'E' a process where emission of a phonon takes place. The processes mentioned here are referred to in the following as the basic scatter processes.

4.1 Results for non-doped GaAs

In figs. 4.1–4.3 the velocity, kinetic energy and relative valley occupancy are presented as functions of electric field. These results have been obtained by Ensemble Monte Carlo simulations of GaAs at 77 K, where only the basic scatter processes are taken into account. This represents the situation of bulk GaAs with a negligible doping. The same quantities for the same material at 300 K are shown in figs. 4.4–4.6. In each figure the overall values of each quantity are shown together with those in the separate valleys.

The carrier density is taken equal to the intrinsic carrier density, which equals $2.25 \cdot 10^{6}$ cm^{-3} at 300 K. In reality, GaAs will always be unintentionally doped, giving rise to carrier density higher than the intrinsic value. For the purpose of the simulations presented in this subsection the electron density is irrelevant.

As the material parameters of Williams and Glisson (see chapter 3) have been used, the results of the present work have been compared with those obtained by these authors, at electric fields strengths of 4, 7 and 20 kV/cm (Williams 1982, Glisson et al. 1982).

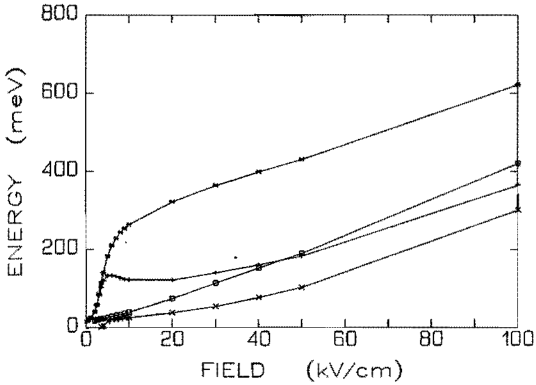

Fig. 4.1 *The average steady-state kinetic energy against electric field for bulk GaAs at 77 K, for all electrons (+), and electrons in the Γ-valley (*), the L-valley (o), and the X-valley (x).*

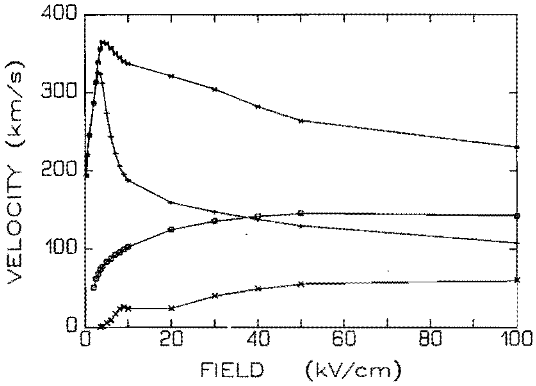

Fig. 4.2 *The average drift velocity against electric field for bulk GaAs at 77 K. The symbols have the same meaning as in fig. 4.1.*

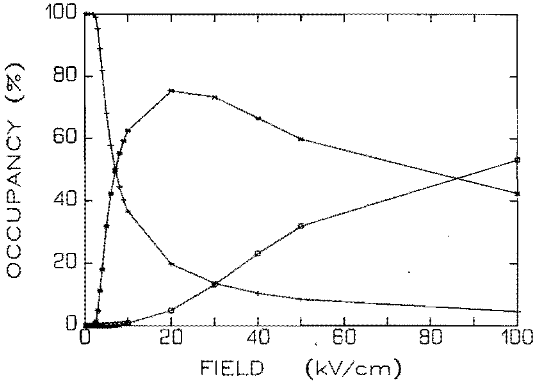

Fig. 4.3 *The average relative valley occupancy against electric field for bulk GaAs at 77 K, for electrons in the Γ-valley (+), the L-valley (*), and the X-valley (o).*

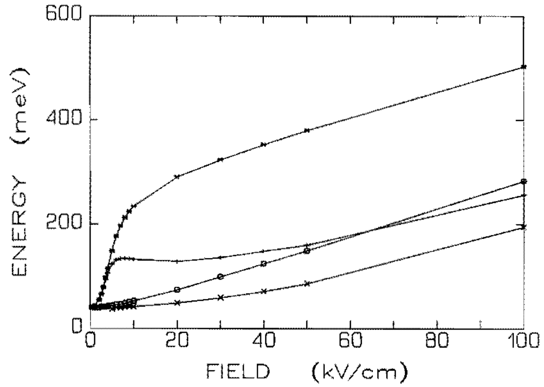

Fig. 4.4 *The average steady-state kinetic energy against electric field for bulk GaAs at 300 K, for all electrons (+), and electrons in the Γ-valley (*), the L-valley (o), and the X-valley (x).*

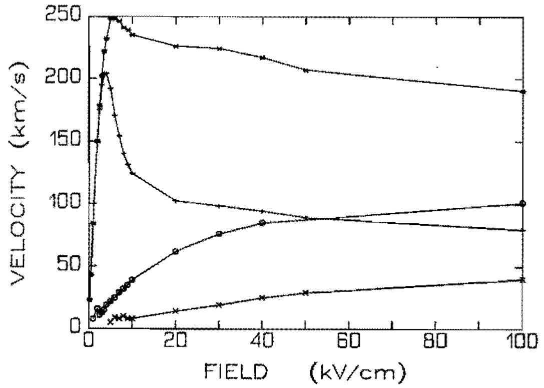

Fig. 4.5 *The average drift velocity against electric field for bulk GaAs at 300 K. The symbols have the same meaning as in fig. 4.4.*

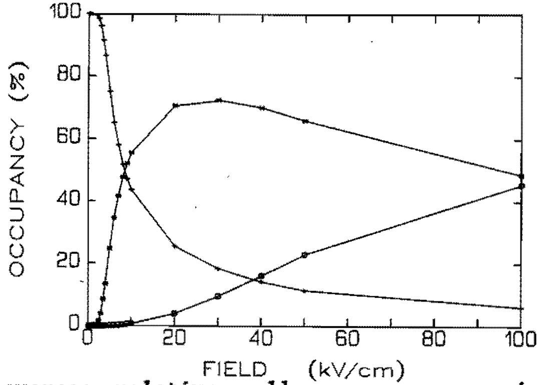

Fig. 4.6 *The average relative valley occupancy against electric field for bulk GaAs at 300 K, for electrons in the Γ-valley (+), the L-valley (*), and the X-valley (o).*

The present results have been obtained with a three-valley (Γ-L-X) model, the results of Williams and Glisson with a two-valley (Γ-L) model. However, this will cause a (small) difference only at 20 kV/cm, as the X-valley becomes populated only at field strengths above 10 kV/cm.

The following respective values have been obtained at the fields mentioned above: velocity 204, 154 and 102 km/s (Williams and Glisson: 203, 156 and 94 km/s), energy .106, .134 and .128 eV (.105, .137 and .132 eV) and Γ-valley occupancy 86.6, 58.1 and 25.4 % (87.8, 61.2 and 29.6 %). Regarding the fact that the deviations always remain smaller than 5 % (with the exception of the velocity and valley occupancy at 10 kV/cm) it may be concluded that the computer program developed performs correctly.

A comparison has also been made with experiments carried out at room temperature (Braslau and Hauge 1970, Houston and Evans 1977). The measured and calculated velocity–field curves, shown in fig. 4.7, match satisfactorily.

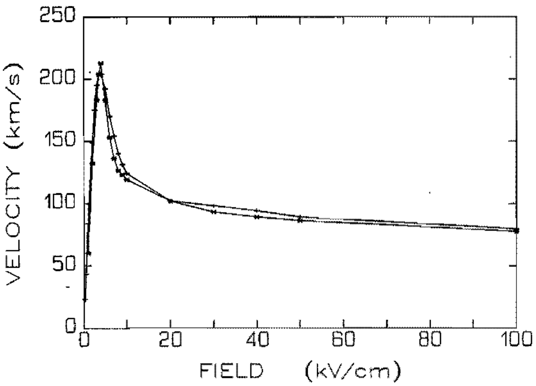

Fig. 4.7 *The drift velocity for electrons in undoped bulk GaAs at 300 K, obtained by EMC calculations (+), compared with measured values (*).*

In tables 4.1 and 4.2 the occurrence of the scatter processes at fields of 1, 5, and 10 kV/cm are shown for temperatures of 77 K and 300K, respectively. These tables give a good impression of the relative importance of each scatter process under different circumstances and will serve as a starting point to study the influence of the scatter processes coming into play at high doping densities.

It is clear from these tables that polar optical phonon scattering is the dominant process. In addition, the temperature-dependence of the Bose–Einstein distribution (eq. 3.5) can be recognised in the less frequent occurrence of both this scatter process and intervalley scattering at 77 K compared with 300 K. As less optical and intervalley phonons are available at lower temperature, scattering by such phonons becomes less likely.

The higher velocities at 77 K are mainly caused by these effects. Firstly, because of the decreased importance of intervalley scattering more electrons reside in the high-mobility Γ-valley. Secondly, as a consequence of the decrease in the occurrence of polar optical phonon scattering, electrons in any valley have a higher velocity.

Table 4.1 *The average occurrence, per electron, per valley, of the basic scatter processes in GaAs at 77 K, for electric field strengths of 1, 5 and 10 kV/cm. Steady-state conditions are considered, and the results apply to a time interval of 0.1 ps.*

	1 kV/cm		5 kV/cm		10 kV/cm	
	Γ	L	Γ	L	Γ	L
# electrons	5000		3405	1595	1830	3130
Ace	> 0		0.01	0.03	0.01	0.04
PE	0.02		0.01	0.05	0.01	0.04
POPA	0.0		> 0	0.01	> 0	0.01
POPE	0.07		0.42	0.12	0.50	0.27
g-LA	0.0		0.0	> 0	0.01	> 0
g-LE	0.0		0.04	0.09	0.15	0.09
g-XA	0.0		0.0		> 0	
g-XE	0.0		0.0		0.01	
L-LA				0.01		0.01
L-LE				0.08		0.18
L-XA				0.0		0.0
L-XE				0.0		> 0
NPOPA	0.0		0.0	0.0	0.0	0.0
NPOPE	0.0		0.0	0.0	0.0	> 0

Table 4.2 *The average occurrence, per electron, per valley, of the basic scatter processes in GaAs at 300 K, for electric field strengths of 1, 5 and 10 kV/cm. Steady-state conditions are considered, and the results apply to a time interval of 0.1 ps.*

	1 kV/cm		5 kV/cm		10 kV/cm	
	Γ	L	Γ	L	Γ	L
# electrons	4997	3	3755	1240	2180	2785
Ace	0.01		0.03	0.16	0.04	0.17
PE	0.08		0.05	0.15	0.04	0.15
POPA	0.23		0.21	0.41	0.20	0.42
POPE	0.25		0.53	0.46	0.64	0.55
g-LA	0.0		0.04	0.05	0.12	0.05
g-LE	0.0		0.03	0.14	0.12	0.14
g-XA	0.0		> 0		> 0	
g-XE			0		> 0	
L-LA				0.29		0.31
L-LE				0.32		0.39
L-XA				> 0		> 0
L-XE				> 0		> 0
NPOPA	0.0		0.0	0.01	0.0	0.01
NPOPE	0.0		0.0	0.01	0.0	0.01

4.2 Effect of ionized impurity scattering

Usually, n-doped GaAs is obtained by doping with Si or Ge. The donor level for both materials is located about 6 meV below the conduction band. In order to obtain an ionized impurity density of $5\cdot10^{17}$ cm^{-3} at 77 K or an ionized impurity density of $1\cdot10^{18}$ cm^{-3} at 300 K it can be calculated (Smith 1978) that one needs a doping density of approximately $1.4\cdot10^{19}$ cm^{-3}, or $5.4\cdot10^{18}$ cm^{-3} respectively.

In figs. 4.8–4.10 the results of Ensemble Monte Carlo calculations at 77 K are shown with ionized impurity and electron densities of 10^{15}, 10^{16}, 10^{17} and $5\cdot10^{17}$ cm^{-3}, respectively. For comparison, the values for the zero-doping case are included. Contrary to the presentation in the previous section no distinction is made between separate valleys. No essential new information would be provided, since qualitatively for each case the same curves result.

In figs. 4.11–4.13 the same approach is taken for the results obtained at room temperature, for ionized impurity and electron densities of 10^{16}, 10^{17}, $5\cdot10^{17}$ and 10^{18} cm^{-3}. The same general conclusions can be drawn for both temperatures: the higher the doping density, the lower the drift velocity, the lower the energy and the higher the Γ-valley occupancy. These effects are most prominent at fields up to 3 kV/cm, since the impurities have the largest influence on low-energy electrons.

The above results have been compared with magnetoresistance measurements by Evanno (1983) and Monte Carlo calculations by Perri (1986), for an ionized impurity and electron density of 10^{17} cm^{-3} at 300 K. From table 4.3 one can conclude that neither the results by

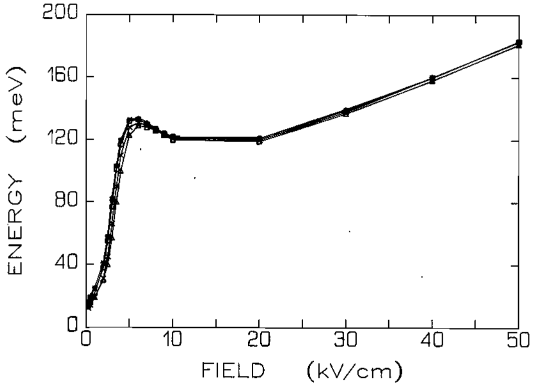

Fig. 4.8 *Average steady-state kinetic energy against electric field in GaAs at 77 K. The ionized impurity densities are 0 (+), 10^{15} cm^{-3} (*), 10^{16} cm^{-3} (o), 10^{17} cm^{-3} (x), and $5\cdot10^{17}$ cm^{-3} (Δ).*

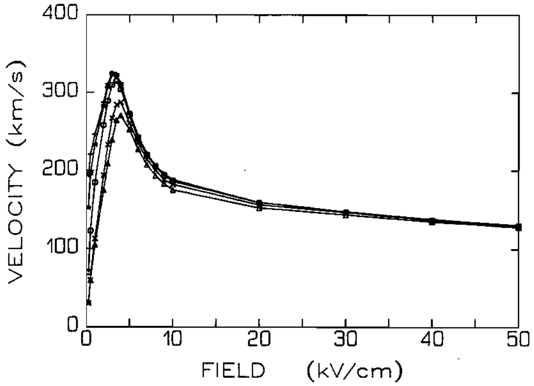

Fig. 4.9 *Average drift velocity against electric field in GaAs at 77 K. The symbols have the same meaning as in fig. 4.8.*

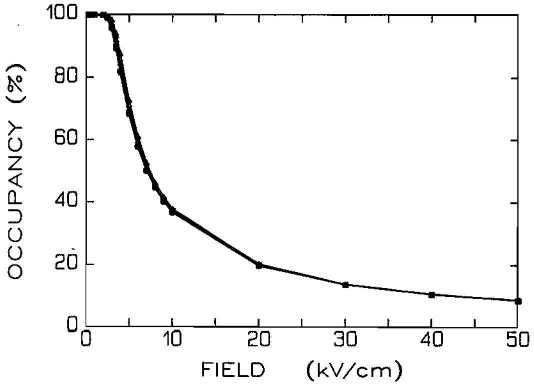

Fig. 4.10 *Average relative Γ-valley occupancy against electric field in GaAs at 77 K. The symbols have the same meaning as in fig. 4.8.*

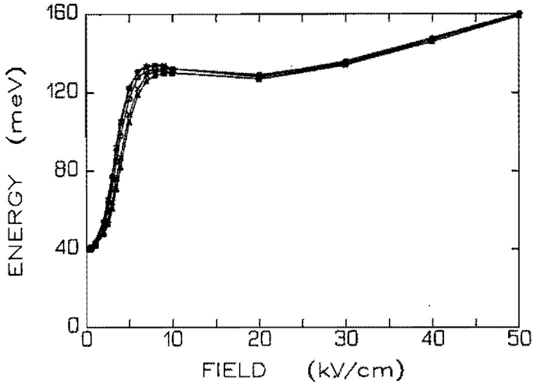

Fig. 4.11 *Average steady-state kinetic energy against electric field in GaAs at 300 K. The ionized impurity densities are 0 (+), 10^{16} cm^{-3} (*), 10^{17} cm^{-3} (o), $5 \cdot 10^{17}$ cm^{-3} (x), and 10^{18} cm^{-3} (Δ).*

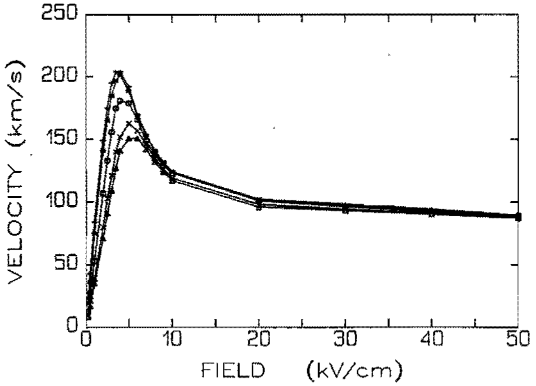

Fig. 4.12 *Average drift velocity against electric field in GaAs at 300 K. The symbols have the same meaning as in fig. 4.11.*

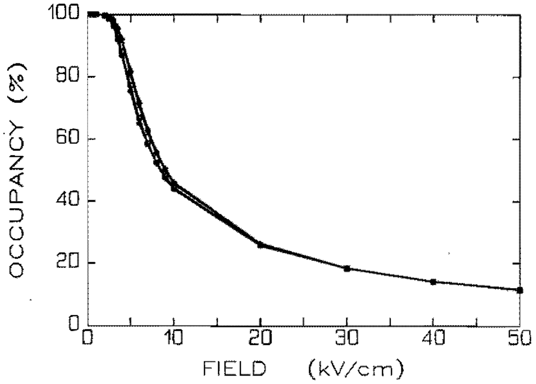

Fig. 4.13 *Average relative Γ-valley occupancy against electric field in GaAs at 300 K. The symbols have the same meaning as in fig. 4.11.*

Perri nor the results obtained in this work exactly match the measurements. However, in a qualitative manner, both match the measurements equally well.

In table 4.4 the rate of occurrence in steady state of all scatter processes is shown for an ionized impurity density of 10^{18} cm^{-3} at 300 K. Comparison of table 4.4 with table 4.2 shows that for an ionized impurity and electron density of 10^{18} cm^{-3} (at 300 K), ionized impurity scattering is the most important scatter process at low fields. However with increasing fields this process becomes less important.

Table 4.3 *Steady-state velocities in n-doped GaAs as obtained from this work (KN), Monte Carlo calculations by Perri (FP) and magnetoresistance measurements by Evanno (MHE). Ionized impurity and electron density is 10^{17} cm^{-3} and the temperature equals 300 K.*

Electric field	velocity (KN)	velocity (FP)	velocity (MHE)
(kV/cm)	(km/s)	(km/s)	(km/s)
1	53	52	35
3	156	155	108
5	179	156	170
10	123	110	105
20	101	97	-

Table 4.4 *The average occurrence, per electron, per valley, of the scatter processes in n-doped GaAs at 300 K, for electric field strengths of 1, 5 and 10 kV/cm. The ionized impurity and electron density equal 10^{18} cm^{-3}. Steady-state conditions are considered, and the results apply to a time interval of 0.1 ps. Scattering by the impurities is denoted by the abbreviation IIe.*

	1 kV/cm		5 kV/cm		10 kV/cm	
	Γ	L	Γ	L	Γ	L
# electrons	5000		4125	870	2305	2665
Ace	0.01		0.02	0.15	0.04	0.17
PE	> 0		> 0	0.01	0.0	0.01
POPA	0.23		0.21	0.42	0.20	0.41
POPE	0.24		0.45	0.46	0.63	0.53
g-LA	0.0		0.023	0.049	0.11	0.05
g-LE	0.0		0.017	0.136	0.11	0.14
g-XA	0.0		0.0		0.0	
g-XE	0.0		0.0		0.0	
L-LA				0.29		0.30
L-LE				0.32		0.37
L-XA				0.0		> 0
L-XE				0.0		> 0
IIe	0.95		0.77	1.30	0.61	1.31
NPOPA	0.0		0.0	0.01	0.0	0.01
NPOPE	0.0		0.0	0.01	0.0	0.01

4.3 Effect of degeneracy

4.3.1 Discussion of degeneracy

The Pauli exclusion principle becomes more important under degenerate conditions. In that case the Fermi–Dirac distribution

$$f_{FD}(W) = \frac{1}{\exp[(W-\zeta)/k_BT] + 1}\ , \tag{4.1}$$

where ζ is the chemical potential (or Fermi level), can no longer be approximated by the Maxwell–Boltzmann distribution

$$f_{MB}(W) = \exp[(\zeta-W)/k_BT]. \tag{4.2}$$

In the usual Monte Carlo approach, for the calculation of the scatter rate in eq.(2.5) the transition rate $S(\vec{k},\vec{k}')$ is used, neglecting the factor $1 - f(\vec{k}')$ formally to be taken into account according to eq.(1.4). This factor represents the probability that the new state $\vec{k}'$ is not occupied. This corresponds to $f_{MB}(W')$ or $f_{MB}(\vec{k}')$ equal 0. This approximation serves well under non-degenerate conditions, where Maxwell–Boltzmann statistics apply.

The chemical potential is found from (Ziman 1972)

$$\zeta = W_F - \frac{\pi^2}{6}(k_BT)^2 \left[\frac{\partial}{\partial W} \ln g(W)\right]_{W=W_F}$$

$$= W_F - \frac{\pi^2(k_BT)^2}{12}\cdot\frac{(1 + 8\alpha W_F + 8\alpha^2W_F^2)}{c_F(1 + 2\alpha W_F)}\ . \tag{4.3}$$

Here α is the non-parabolicity parameter for the Γ-valley as given by eq.(3.2). The chemical potential at $T = 0$ K is called the Fermi energy W_F, and is equal to

$$W_F = \frac{-1 + \sqrt{1 + 4c_F}}{2\alpha} , \tag{4.4}$$

where

$$c_F = \frac{\hbar^2}{2m^*}(3n_e\pi^2)^{2/3} , \tag{4.5}$$

and n_e is the electron concentration. The density of states in the conduction band, $g(W)$, is given by, using the Kane approximation,

$$g(W) = \frac{2^{1/2}(m^*)^{3/2}}{\pi^2\hbar^3} \sqrt{W(1 + \alpha W)}\ (1 + 2\alpha). \tag{4.6}$$

All energies are taken with respect to the bottom of the conduction band. Only the Γ-valley is taken into account here. As electrons in thermodynamical equilibrium are considered, this approximation will not lead to serious errors.

As the limit for the validity of the Maxwell–Boltzmann approach the electron concentration at which ζ rises above the bottom of the conduction band is taken. Only at concentrations higher than this limiting value $n_{e,\mathrm{limit}}$ degeneracy effects will be taken into account.

Taking α equal to zero leads to

$$n_{e,\mathrm{limit}} = \frac{4\pi}{3\cdot 12^{3/4}}\, 2\left(\frac{2m^*\pi k_B T}{\hbar^2} \right)^{3/2} = 0.64\ N'_c , \tag{4.7}$$

where for GaAs N'_c is a few percents smaller than the effective density of states in the conduction band, N_c (Blakemore 1982). Usually, the limit is taken as (Smith 1978)

$$n_{e,\mathrm{limit}} = 0.4\ N_c . \tag{4.8}$$

Hence, approximation eq.(4.7) will serve well. The values for $n_{e,\mathrm{limit}}$ at 77 K and 300 K resulting from eq.(4.7) are

$$n_{e,\mathrm{limit}}(77) = 2.58\cdot10^{17}\ \mathrm{cm}^{-3}\ , \tag{4.9}$$

and

$$n_{e,\mathrm{limit}}(300) = 3.35\cdot10^{16}\ \mathrm{cm}^{-3}, \tag{4.10}$$

respectively.

4.3.2 Inclusion of degeneracy in Ensemble Monte Carlo calculations

The method followed to introduce the degeneracy effects into the Ensemble Monte Carlo scheme is based upon the ideas of Bosi and Jacoboni (1976), originally developed for the one-electron Monte Carlo method. Lugli and Ferry (1985c) further developed these ideas which will be presented below, with some minor changes.

The quintessence of the solution lies in the factor 1 - $f(\vec{k}')$ 'officially' modifying the transition rate $S(\vec{k},\vec{k}')$ (see chapter 2). As outlined in the former subsection, $f(\vec{k}')$ is set to zero assuming Maxwell–Boltzmann statistics. All final states $\vec{k}'$ are available in this scheme. In Ensemble Monte Carlo methods $f(\vec{k}')$ is exactly known at equidistant time steps and could be used to update the scatter rates at regular time intervals (Williams et al. 1986), which is a very time consuming process. Therefore a different approach, also based upon the knowledge of $f(\vec{k}')$ in the Ensemble Monte Carlo scheme, is followed.

In first instance the usual procedure for the selection of a scatter process and the final state is applied (see chapter 2). Once the final state $\vec{k}'$ has been chosen, the normalized $f(\vec{k}')$ has become exactly known and a rejection technique is used to decide whether the transition from $\vec{k}$ to $\vec{k}'$ actually will take place.

Note that in $f(\vec{k}')$ the $\vec{k}'$ for the electron under treatment is contained at the *end* of its free flight, together with the states of the other electrons at the *beginning* of the free flight. A suitable choice of time step between the observation points, i.e. comparable to the scatter time (≤ 0.1 ps), minimizes the error.

The normalization of $f(\vec{k}')$ consists of determining how many electrons are allowed to occupy a cell of given volume in $\vec{k}$-space with respect to the electron density. When M simulation electrons are used to simulate a density n_e, the effective volume V of real space that is occupied equals $V = M/n_e$. The density of allowed wave vectors is equal to $2V/(2\pi)^3$ (Kittel 1986), where the factor 2 accounts for the two possible spin orientations of an electron. Now, a grid can be set up in $\vec{k}$-space, with cells of volume

$$\Omega_c(k,\vartheta,\phi) = k^2 \sin\vartheta \; d\vartheta d\phi dk \ . \tag{4.11}$$

The number of electrons M_c that are allowed to occupy a cell with volume Ω_c is the density of states times the volume, so

$$M_c = \frac{2\Omega_c V}{8\pi^3} = \frac{2\Omega_c M}{8\pi^3 n_e} \ . \tag{4.12}$$

The normalized distribution f_c is determined for each cell and is equal to the number of electrons occupying a cell, divided by M_c.

This f_c and a random number $\tilde{r}$ in [0,1) are used to decide whether an electron is allowed to enter that particular cell: if $\tilde{r} \leq f_c$ the transition is forbidden and a self-scattering takes place instead, and if $\tilde{r} > f_c$ it is allowed and carried out.

With this algorithm actually the Pauli exclusion principle will be taken into account.

In the approach outlined above two minor changes compared to the one proposed by Lugli and Ferry (1985c) have been introduced.

These authors considered a constant cubic volume $\Omega_c = \Delta k_x \Delta k_y \Delta k_z$ in $\vec{k}$-space instead of a variable 'spherical' volume, as presented in this work. The reason of this change is the following. Drawing electrons in initial states determined by the Fermi–Dirac distribution, followed by the restriction imposed by the Pauli exclusion principle, does not yield a satisfactory distribution (i.e., a Fermi–Dirac distribution) when using a constant cubic volume, whereas using a spherical volume it does. As Zimmermann (1987) suggested, the method presented here more closely reflects the symmetry of the problem.

Another change will be introduced in the following. Lugli and Ferry report an application of their algorithm only to low-field problems (90 V/cm and 900 V/cm), in which all electrons reside in the Γ-valley. A complete extension to the three-valley model for higher fields would be rather complicated, though feasible. In this work it is suggested to circumvent this problem at first instance. Considering the fact that in the L- and X-valleys much more states are available than in the Γ-valley, it is reasonable to suppose that the Pauli exclusion principle will not come into play for states in these valleys. So, the rejection scheme will only be considered when the *final* state is in the Γ-valley.

This approximation is expected to yield, as a first order approach, at the electron concentrations considered in the following, a good qualitative impression of what will happen at higher fields, where also electrons in the other valleys are present.

4.3.3 Results

The results of Ensemble Monte Carlo calculations for GaAs, taking the Pauli exclusion principle into account, are shown in figs. 4.14–4.16. The ionized impurity and electron densities are 10^{18} cm^{-3} and the temperature 300 K. For comparison, also the results obtained neglecting degeneracy (section 4.2) are shown in these figures.

As can be seen in fig. 4.14 the influence on energy is the most prominent at fields up to 10 kV/cm. This corresponds to what is expected. At low fields the electrons are densely packed in $\vec{k}$- (and energy) space according to the Fermi–Dirac distribution. Only higher wave vector values (higher energies) are available as final states.

At fields below 5 kV/cm velocity has increased. This is caused by the fact that the exclusion principle at these fields mainly operates at the expense of ionized impurity scattering (which process has its maximum probability at low energies in the order of 0.03 eV), as can be concluded from comparison of tables 4.4 and 4.5.

At fields above 5 kV/cm this effect no longer dominates, but the fact that more electrons reside in the low-mobility L-valley (see fig. 4.12), and the velocity drops below the values calculated without the exclusion principle.

Between 10 and 20 kV/cm the effect eventually disappears, as the electrons have been spread out sufficiently in $\vec{k}$-space, and sufficient states have become available.

The influence on the energy distributions of electrons in the Γ-valley is demonstrated for fields of 1 and 5 kV/cm, respectively, in figs. 4.17 and 4.18. The influence of the exclusion principle at 5 kV/cm is less pronounced than at 1 kV/cm, but still present.

Comparison of the present results at a field of 900 V/cm with those obtained by Lugli and Ferry shows the same behaviour for the energy distribution. However, the influence on velocity does not correspond. This may be caused by the fact that in the work of Lugli and Ferry Thomas-Fermi screening is used, instead of Debye screening. In Thomas-Fermi screening the screening length as defined by eq.(3.27) is used, with the 'electron temperature' instead of the lattice temperature. The electron temperature, a measure for the kinetic energy of the electrons, is not a constant, and is usually larger than the lattice temperature. As a consequence of a higher temperature the screening length increases, and therefore the influence of ionized impurity scattering, yielding lower velocities.

Comparison however with comparable calculations of Williams et al. (1986), which were obtained by regularly updating the scatter rates, shows the same influence of degeneracy on low field behaviour.

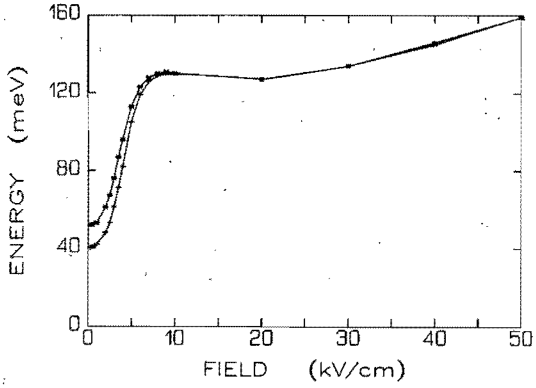

Fig. 4.14 Average steady-state kinetic against electric field for GaAs at 300 K. The ionized impurity density is 10^{18} cm^{-3}. The case (*) where degeneracy is taken into account, and (+) where it is not.

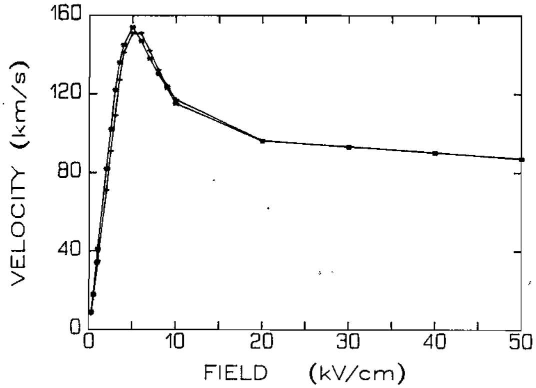

Fig. 4.15 Average drift velocity against electric field for GaAs at 300 K. The ionized impurity density is 10^{18} cm^{-3}. The symbols have the same meaning as in fig. 4.14.

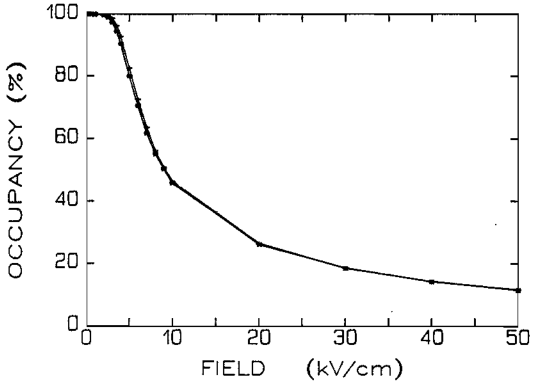

Fig. 4.16 Average relative Γ-valley occupancy against field for GaAs at 300 K. The ionized impurity density is 10^{18} cm^{-3}. The symbols have the same meaning as in fig. 4.14.

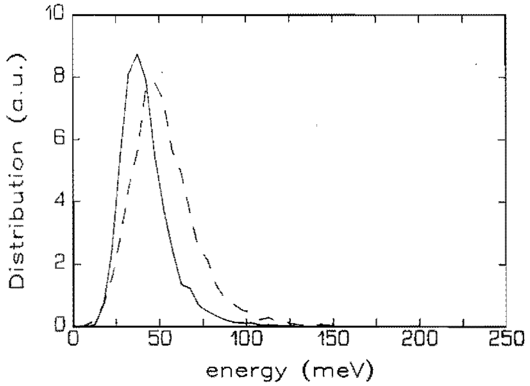

Fig. 4.17 *Energy distribution of Γ-valley electrons in steady state, without (—) and with (– –) degeneracy being taken into account. Ionized impurity density is 10^{18} cm^{-3}, the temperature is 300 K and the electric field strength is 1 kV/cm.*

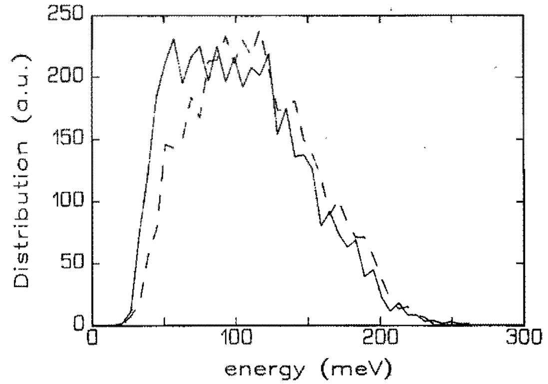

Fig. 4.18 *Energy distribution of Γ-valley electrons in steady state, without (—) and with (– –) degeneracy being taken into account. Ionized impurity density is 10^{18} cm^{-3}, the temperature is 300 K and the electric field strength is 5 kV/cm.*

Table 4.5 *The average occurrence, per electron, per valley, of the scatter processes in n-doped GaAs at 300 K, for electric fields of 1, 5 and 10 kV/cm. The ionized impurity and electron density equal 10^{18} cm^{-3}. Steady-state conditions are considered, and the results apply to a time interval of 0.1 ps. Scattering by impurities is denoted by IIe. Degeneracy (PEP) has been taken into account.*

	1 kV/cm		5 kV/cm		10 kV/cm	
	Γ	L	Γ	L	Γ	L
# electrons	4495	5	4000	995	2285	2685
Ace	0.01		0.02	0.16	0.03	0.17
PE	> 0		> 0	0.01	> 0	0.01
POPA	0.20		0.19	0.43	0.19	0.42
POPE	0.21		0.43	0.48	0.57	0.55
g-LA	> 0		0.03	0.06	0.10	0.05
g-LE	> 0		0.02	0.14	0.12	0.14
g-XA	0.0		> 0		> 0	
g-XE	0.0		0.0		> 0	
L-LA				0.30		0.32
L-LE				0.33		0.40
L-XA				> 0		0.01
L-XE				> 0		> 0
IIe	0.60		0.63	1.35	0.55	1.33
PEP	0.61		0.17	> 0	0.03	> 0
NPOPA	0.0		0.0	0.01	0.0	0.01
NPOPE	0.0		0.0	0.01	0.0	0.01

4.4 Effect of electron-electron scattering

The results of Ensemble Monte Carlo calculations for GaAs, including the electron–electron scattering process (chapter 3) are shown in figs. 4.19–4.21. The ionized impurity density and the electron density both are equal to 10^{18} cm^{-3} and the temperature is 300 K. For comparison the results obtained for the same densities without taking this process into account (section 4.2) are also shown.

From fig. 4.19 it is seen that the average energy is hardly affected by this process. However, both velocity and Γ-valley occupancy have been significantly raised, for electric fields in the range 5 to 20 kV/cm.

In table 4.6 the rates of occurrence of the scatter processes are shown. Comparison with table 4.4 shows that at 1 kV/cm the occurrence of neither of the processes, except of course for the one added, is changed. Therefore it is clear that velocity has not been changed either (fig. 4.20).

At 5 kV/cm the reduction of intervalley scattering, even in steady state conditions is clear, as well as at 10 kV/cm. This suppression of intervalley scattering results in a higher velocity, since more electrons reside in the high-mobility Γ-valley.

The energy distributions of electrons in the Γ-valley at 1, 5 and 10 kV/cm, rsepectively, are shown in figs. 4.22–4.24. These figures clearly show the thermalizing influence of electron–electron scattering. The influence on the occurrence of intervalley scattering arises from the 'shrinking' of the energy distribution at the high-energy tail, as the probability of intervalley scattering increases with increasing energy.

One-electron Monte Carlo results obtained by Inoue and Frey (1980) under the same conditions yield results, which are qualitatively comparable to the present results. At 4 kV/cm the following values have been found: average velocity with and without electron–electron scattering 148 and 138 km/s, respectively (Inoue and Frey: 170 and 170 km/s), relative Γ-valley occupancy 94.6 and 92.6 % (88 and 86 %), and kinetic energy .084 and .082 eV (.087 and .075 eV). At 10 kV/cm these values have become resp. 136 and 117 km/s (130 and 120 km/s), 49.6 and 46.1 % (37 and 32 %) and .13 and .13 eV (.21 and .18 eV).

The fact that the values do not correspond must be caused by different material parameters. The energies are difficult to compare, as Inoue and Frey only give electron temperatures T_e, which have been converted according to $\frac{3}{2}k_BT_e + \frac{1}{2}m_\Gamma^*v^2 = W_{kin}$.

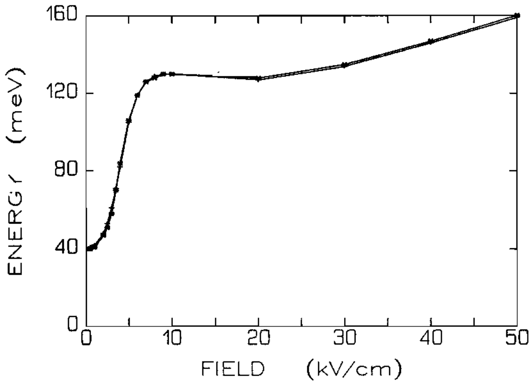

Fig. 4.19 *Average steady-state kinetic energy against electric field for GaAs at 300 K. The ionized impurity density is 10^{18} cm^{-3}. The case (*) where electron–electron scattering is taken into account, and (+) where it is not.*

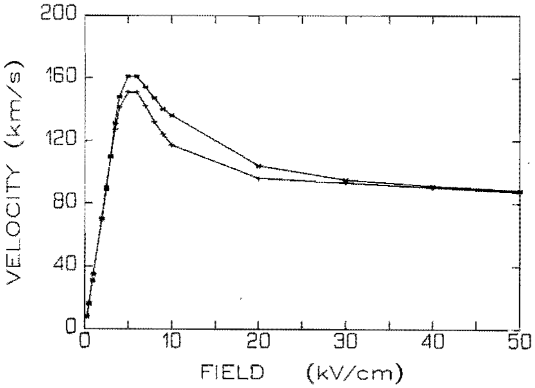

Fig. 4.20 *Average drift velocity as a function of electric field for GaAs at 300 K. The ionized impurity density is 10^{18} cm^{-3}. The symbols have the same meaning as in fig. 4.19.*

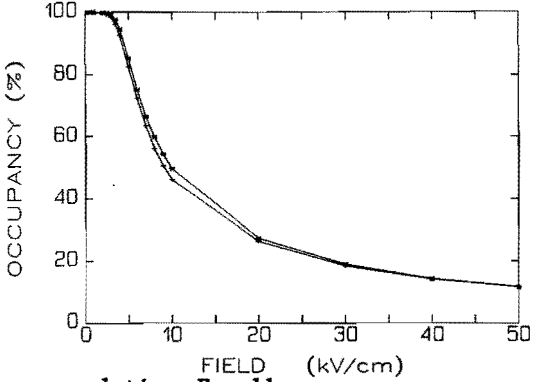

Fig. 4.21 *Average relative Γ-valley occupancy as a function of electric field for GaAs at 300 K. The ionized impurity density is 10^{18} cm^{-3}. The symbols have the same meaning as in fig. 4.19.*

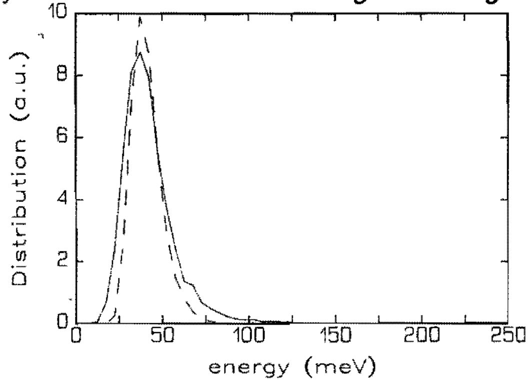

Fig. 4.22 *Energy distribution of Γ-valley electrons in steady state, without (—) and with (– –) electron–electron scattering being taken into account. Ionized impurity density is 10^{18} cm^{-3}, the temperature is 300 K and the electric field strength is 1 kV/cm.*

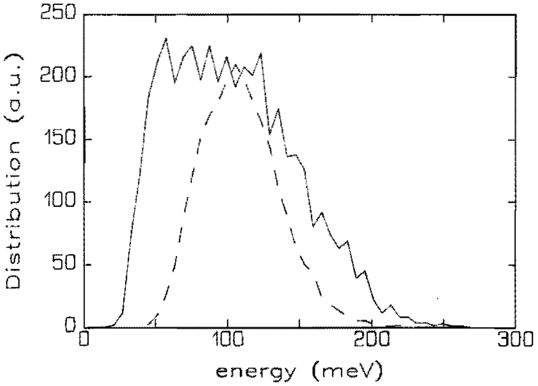

Fig. 4.23 *The same as in fig. 4.22,* **with** *an electric field of 5 kV/cm.*

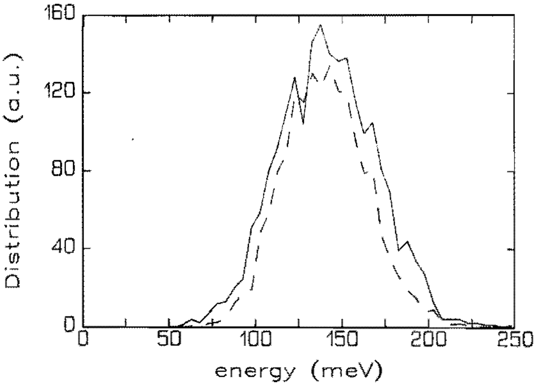

Fig. 4.24 *The same as in fig. 4.22,* **with** *an electric field of 10 kV/cm.*

Table 4.6 *The average occurrence, per electron, per valley, of the scatter processes in n-doped GaAs at 300 K, for electric field strengths of 1, 5 and 10 kV/cm. The ionized impurity and electron density equal* 10^{18} cm^{-3}. *Steady-state conditions are considered, and the results apply to a time interval of 0.1 ps. Scattering by the impurities is denoted by the abbreviation IIe. Electron–electron scattering (E-E) has been taken into account.*

	1 kV/cm		5 kV/cm		10 kV/cm	
	Γ	L	Γ	L	Γ	L
# electrons	5000		4260	735	2480	2480
Ace	0.01		0.02	0.16	0.03	0.18
PE	> 0		>0	0.01	> 0	0.01
POPA	0.23		0.21	0.42	0.19	0.42
POPE	0.24		0.47	0.47	0.58	0.58
g-LA	0.0		0.018	0.054	0.09	0.05
g-LE	0.0		0.015	0.137	0.11	0.14
g-XA	0.0		> 0		> 0	
g-XE	0.0		0.0		> 0	
L-LA				0.30		0.32
L-LE				0.33		0.42
L-XA				> 0		0.01
L-XE				> 0		> 0
IIe	0.95		0.76	1.33	0.59	1.33
NPOPA	0.0		0.0	0.01	0.0	0.01
NPOPE	0.0		0.0	0.01	0.0	0.01
E-E	0.68		0.33	0.66	0.32	0.85

4.5 Effect of electron-electron scattering in combination with degeneracy

Finally, Ensemble Monte Carlo calculations on GaAs have been performed, where electron–electron scattering and the Pauli exclusion principle both are taken into account. This is achieved by the introduction of the factors 1 - $f(\vec{k}'_1)$ and 1 - $f(\vec{k}'_2)$, present in eq.(3.69), in the same way as described in section 4.3. An electron–electron scatter process will be rejected if *one* of the two final states $\vec{k}'_1$ and $\vec{k}'_2$ cannot be occupied.

In figs. 4.25–4.27 the results are shown, for an ionized impurity and electron density of 10^{18} cm^{-3} and a temperature of 300 K. The results obtained in section 4.2 are again shown for comparison.

The results indicate an addition of the two mechanisms: at fields below 4 kV/cm the exclusion principle dominates, resulting in an increased energy and a slight increase of the velocity. The tendency towards higher Γ-valley occupancy caused by electron–electron scattering is at these fields neutralized by the opposite tendency of the exclusion principle.

At fields beyond 4 kV/cm the influence of electron–electron scattering dominates that of the Pauli exclusion principle. Then, practically the same curves as in section 4.4 appear.

The energy distributions given in figs. 4.28 and 4.29 demonstrate the interaction of both mechanisms, at 1 kV/cm. Figure 4.28 shows a comparison of the case with only electron–electron scattering and the case with electron–electron scattering combined with the exclusion principle. Analogous to section 4.3 the distribution is shifted towards higher energies as a consequence of the inclusion of the latter.

Figure 4.29 compares the case of only the exclusion principle with the case of exclusion principle and electron–electron scattering. Again, as in section 4.4, the thermalizing influence shows: the distribution function in the latter case has become less broadened than in the former case.

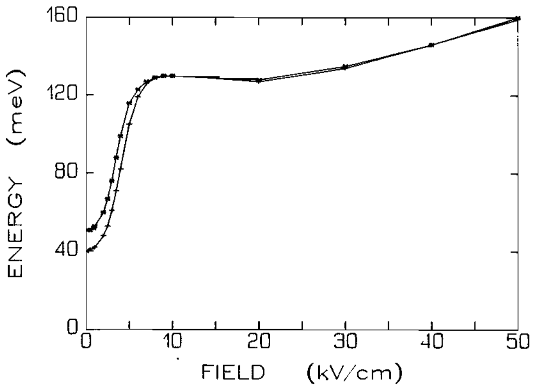

Fig. 4.25 *Average steady-state kinetic energy against electric field for GaAs at 300 K. The ionized impurity density is 10^{18} cm^{-3}, where electron–electron scattering and degeneracy are taken into account (*), and where they are not (+).*

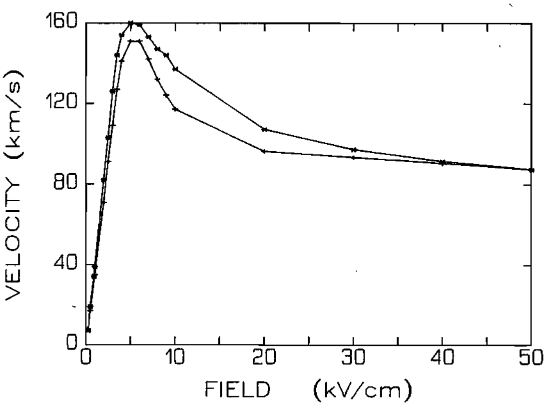

Fig. 4.26 *Average drift velocity against electric field for GaAs at 300 K. The ionized impurity density is 10^{18} cm^{-3}. The symbols have the same meaning as in fig. 4.25.*

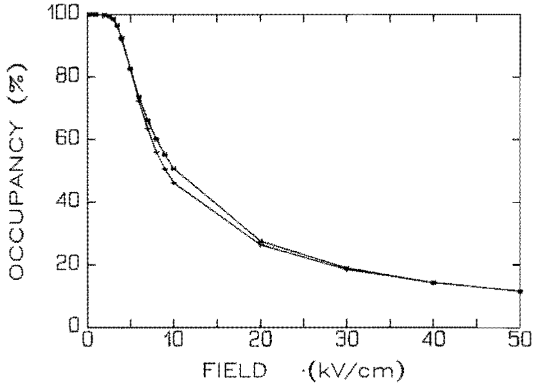

Fig. 4.27 *Average relative Γ-valley occupancy against electric field for GaAs at 300 K. The ionized impurity density is* 10^{18} *cm*$^{-3}$*. The symbols have the same meaning as in fig. 4.25.*

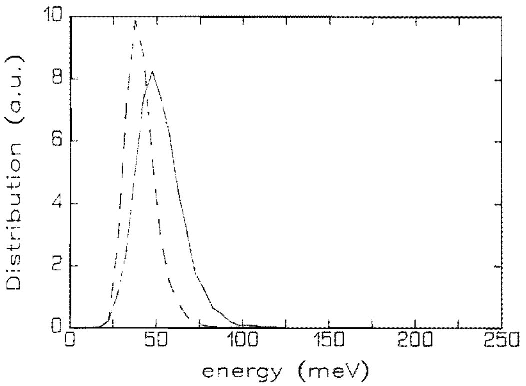

Fig. 4.28 *Energy distribution of Γ-valley electrons in steady state, with electron–electron scattering and degeneracy (—) and with only electron–electron scattering (– –) taken into account. Ionized impurity density is* 10^{18} *cm*$^{-3}$*, the temperature is 300 K and the electric field strength is 1 kV/cm.*

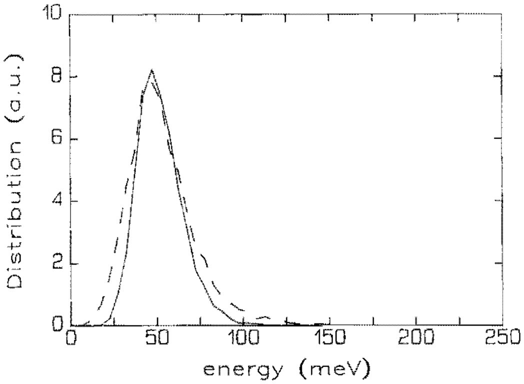

Fig. 4.29 *Energy distribution of Γ-valley electrons in steady state, with electron–electron scattering and degeneracy (—) and with only degeneracy (– –) taken into account. Ionized impurity density is* 10^{18} *cm*$^{-3}$*, the temperature is 300 K and the electric field strength is 1 kV/cm.*

4.6 Concluding remarks

Concerning the effects of degeneracy and electron–electron scattering on the transport properties of GaAs, with an ionized impurity and electron density of 10^{18} cm^{-3} at 300 K, the following conclusions can be drawn.

Electron–electron scattering causes an increase in velocity in the order of 10 % at fields between 5 and 30 kV/cm. While the average energy is hardly affected, the high- and low-energy tails of the energy distribution increase relatively towards the peak value of the distribution. This causes a reduction of intervalley scattering.

As a result of the inclusion of degeneracy velocity is slightly changed; an increase at fields until 10 kV/cm, a decrease at higher fields. The energy distribution as a whole is shifted towards higher energy, especially at low fields. Consequently, at low fields average energy is significantly increased.

When both mechanisms are combined their effects are superposed. In a way both mechanisms counteract, especially at the high-energy tail of the distribution. There, degeneracy pushes the distribution towards higher, and electron—electron scattering towards lower energies.

This observation appears to be in contrast with a statement by Lugli and Ferry (1985c). They stated that degeneracy forces the electrons into high-energy regions, which is correct, after which they conclude that degeneracy has (in a way) exactly the same influence on energy distribution as electron—electron scattering. From the work presented here it follows that the latter only applies to electrons in the low-energy tail!

In general, at the density considered, the effect on transport properties is not dramatic. Electron—electron scattering is the more prominent one of the two mechanisms studied.

At higher densities degeneracy is expected to have a larger influence than at the density considered, which has been confirmed for an electron and ionized impurity density of 10^{19} cm^{-3}. However, at this density, already at near-equilibrium conditions electrons tend to populate the L-valley, and the validity of the model presented here becomes questionable. In this case full account of the occupation of the states in the whole Brillouin zone should be taken. From the view point of algorithm design and physical concept this is not an easy task to fulfil.

Chapter 5

ELECTRON TRANSPORT IN AN AlGaAs/GaAs HETEROJUNCTION

In this chapter results are presented of Ensemble Monte Carlo calculations of electron transport along the interface of an AlGaAs/GaAs heterojunction. Parallel to the interface a constant electric field is applied. A rectangular region is considered with very simple boundary conditions. In order to obtain the electric field perpendicular to the interface, Poisson's equation is solved in one dimension only. This one-dimensional approach is justified because the longitudinal dimension is take sufficiently high for the electron density to be independent of the longitudinal coordinate. On the one hand the model developed serves as a first step in accomplishing a more complex one, i.e. a model of the HEMT (chapter 6). On the other hand it makes it possible to consider into detail the influence of real space transfer and the electric field perpendicular to the interface.

5.1 Introduction

In modulation doped N-AlGaAs/GaAs heterojunctions, conduction electrons in the GaAs side of the heterojunction, under influence of a field parallel to the interface, reach higher steady-state velocities than in n-doped GaAs with an equivalent electron density

(Dingle et al. 1978). This occurs at moderate field strengths and becomes more prominent when the temperature is lower. The speed enhancement is caused by the spatial separation of the conduction electrons in GaAs from the donors in the AlGaAs layer. These electrons originate from AlGaAs, and have been diffused into GaAs. There they have become trapped in a potential well because of the difference in conduction band levels of GaAs and AlGaAs. In addition, as a result of the space charge present, band bending occurs. See fig. 5.1.

In this way, a high electron density has been obtained while the negative effect of ionized impurities on mobility has been circumvented. This is one advantage of the heterojunction based HEMT (chapter 6) over the conventional GaAs MESFET.

In the potential well at the interface a two-dimensional electron gas may be formed. In a two-dimensional electron gas, electron transport perpendicular to the interface is prohibited. The wave vector component in this direction is quantized and discrete energy subbands are formed. As a result, the scatter rates as presented in chapter 3 are modified (Price 1981). However, in the results presented in this chapter, the influence of this energy discretization has been neglected.

Another physical mechanism associated with heterostructures is real space transfer. The concept of real space transfer has been introduced by Hess et al. (1979) as a means of obtaining a negative differential resistance in layered AlGaAs/GaAs heterostructures. Monte Carlo calculations on these structures have been performed, without and with taking into account the influence of the transverse electric field, respectively by Glisson et al. (1980) and Littlejohn et al. (1983).

In the calculations on multiple AlGaAs/GaAs layers by Littlejohn et al. (1983) it has been suggested that in the presence of a transverse field steady-state velocities in GaAs are increased. In the results to be presented in the following the influence of the transverse field will be further investigated, however, in a single heterostructure.

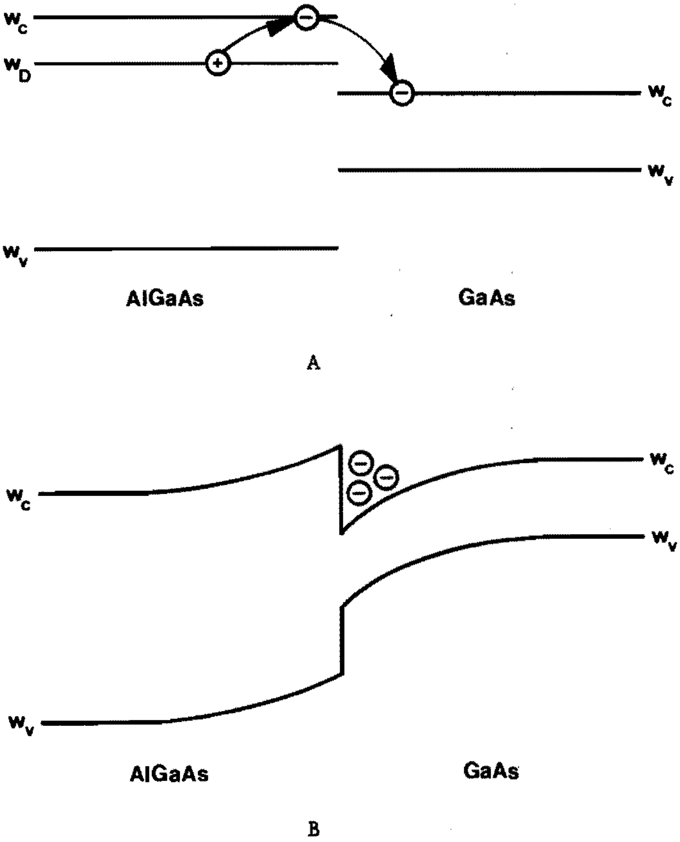

Fig. 5.1 *The energy band diagrams of AlGaAs and GaAs. The diffusion of conduction electrons from the AlGaAs is depicted (A), which electrons become trapped in the potential well at the heterointerface (B).*

5.2 Description of the model for electron transport

The area studied is rectangular and consists of a layer of N-doped AlGaAs on top of a layer of undoped GaAs, see fig. 5.2. Starting from a situation of thermal equilibrium with all electrons in GaAs, the electron transport under influence of an electric field parallel to the interface (corresponding to the x-direction in fig. 5.2) is studied. This field will be denoted by 'longitudinal' field.

In order to obtain the electric field perpendicular to the interface, Poisson's equation is solved in this direction (the y-direction). The resulting field is called the 'transverse' field.

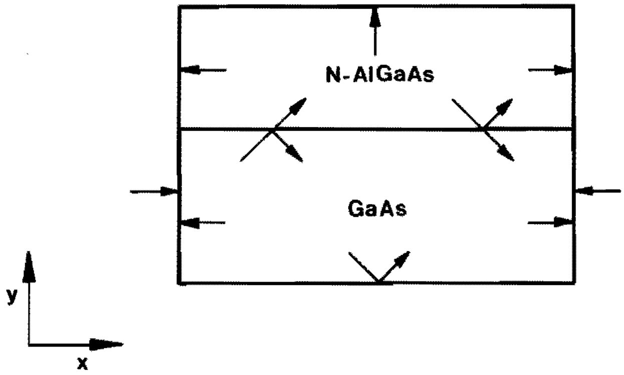

Fig. 5.2 *The heterojunction modelled consists of a layer of N-AlGaAs on top of undoped GaAs. The arrows denote the boundary conditions for the electrons, which will be introduced in section 5.2.3.*

5.2.1 Ensemble Monte Carlo method

The Ensemble Monte Carlo method as described in chapter 2 is applied. The longitudinal field is fixed, and the transverse field is determined from the solution of Poisson's equation

$$\frac{\partial^2 \phi}{\partial y^2} = - \frac{\rho}{\epsilon_0 \epsilon_s} . \qquad (5.1)$$

Here ϕ denotes the potential and ρ the charge density. The transverse electric field E_y is given by

$$E_y = \frac{\partial \phi}{\partial y} . \qquad (5.2)$$

In this approach the variation of electron density in the x-direction is neglected. This is justified, the longitudinal field being constant, if the length of the interface is long enough for electrons to reach the steady-state velocity when they proceed along the interface. This condition is surely fulfilled with an interface length over 2 μm.

The conduction bands of GaAs and AlGaAs are both described by the three-valley model given in chapter 3. The material parameters for both materials are taken from table 3.1.

Scatter processes taken into account are acoustic phonon, piezoelectric, polar and non-polar optical phonon, equivalent and non-equivalent intervalley scattering, and in the AlGaAs also ionized impurity and random potential alloy scattering. Note that energy discretization in the potential well at the interface is not taken into account. This means that the scatter rates given in chapter 3 apply.

5.2.2 Boundary conditions for Poisson's equation

The total simulation time is divided into equidistant time intervals, the so-called field-adjusting time steps. At the end of each time step the one-dimensional Poisson equation (5.1) is solved, from which the transverse electric field distribution valid in the next step is determined.

The direction for which eq.(5.1) is solved is divided into a uniform one-dimensional 'mesh'. As all electrons are considered to originate from the AlGaAs layer, the charge density $d\rho$ associated with one simulation particle is given by

$$d\rho = - \frac{e t_{AG} N_D^+}{M}. \tag{5.3}$$

Here t_{AG} means the thickness of the AlGaAs layer, N_D^+ the ionized impurity density in this layer, and M the number of simulation particles. This charge density is attributed to the mesh point nearest to the electron considered.

The following boundary conditions for the electric field are applied for the solution of eq.(5.1). The electric field at the extreme boundaries equals zero, and the normal component of the dielectric displacement is continuous, i.e. at the heterointerface

$$\epsilon_{s,AG} E_{y,AG} = \epsilon_{s,G} E_{y,G} \tag{5.4}$$

The indices G and AG denote GaAs and AlGaAs, respectively.

The boundary conditions for the potential are depicted in fig. 5.3, where the energy band diagrams of AlGaAs and GaAs in equilibrium are shown. At the top of the AlGaAs layer, by analogy with a gate, the internal potential equals the applied potential diminished by the Schottky barrier potential (see also chapter 6).

The potential difference in fig. 5.3 associated with the term $\zeta_{AG} - \zeta_G - \Delta W_c$ is the so-called built-in potential (Casey and Panish 1978), where ζ is the chemical potential (Fermi level) and ΔW_c the difference in the conduction band energy levels of the two materials. Under non-degenerate conditions ζ with respect to the conduction band is given by (Smith 1978)

$$\zeta = k_B T \ln(n_e/N_c), \tag{5.5}$$

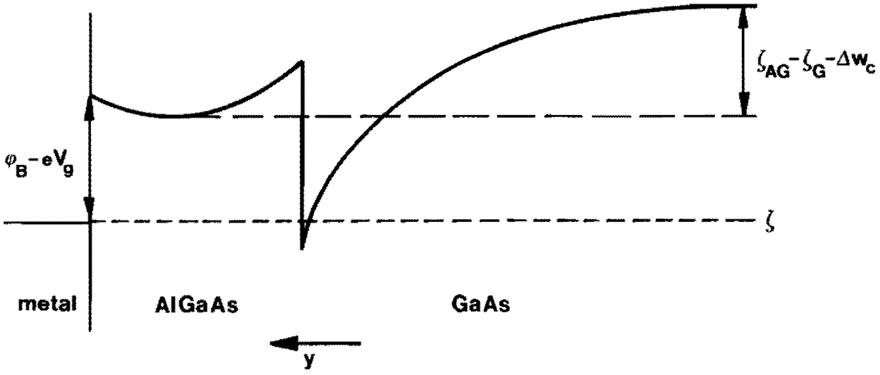

Fig. 5.3 *The AlGaAs/GaAs energy band diagram for the conduction band, with the boundary conditions for the potential.*

where the effective density of states in the conduction band N_c is approximated by (Casey and Panish 1978)

$$N_c = \frac{(k_B T m_0^{1/2})^3}{2^{1/2}\pi^{3/2}\hbar^3}\left[\left(\frac{m_\Gamma}{m_0}\right)^{3/2} + 4\left(\frac{m_L}{m_0}\right)^{3/2}\exp\left(-\frac{W_{\Gamma L}}{k_B T}\right)\right.$$

$$\left. + 3\left(\frac{m_X}{m_0}\right)^{3/2}\exp\left(-\frac{W_{\Gamma X}}{k_B T}\right)\right]. \tag{5.6}$$

Here, $W_{\Gamma L}$ and $W_{\Gamma X}$ are the differences in energy between the Γ- and the L-, respectively, the X-valley.

The chemical potential for the N-doped AlGaAs has been calculated with eqs.(5.5) and (5.6). For the undoped GaAs the expression valid for intrinsic semiconductors (Smith 1978) is used, giving ζ with respect to the conduction band

$$\zeta = -\frac{1}{2}\,\Delta W_g + \frac{3}{4}\,k_B T\,\ln(m_h/m_e). \tag{5.7}$$

For the effective hole mass $m_h = 0.50m_0$ is taken (Blakemore 1982) and for the effective electron mass $m_e = 0.063m_0$. This yields for GaAs at 300 K a value of $\zeta = -0.68$ eV , i.e. slightly higher than midway between conduction and valence band. The ratio of the difference in conduction band ΔW_c and the difference in band gap ΔW_g for AlGaAs and GaAs has been the subject of intensive debate. Values in the range between 0.59 and 0.85 have been reported. A review has been given by Kroemer (1986), and he recommended to accept the value determined by Watanabe et al. (1985). This suggestion is followed here, and a value

$$\Delta W_c = 0.62\ \Delta W_g . \tag{5.8}$$

is used.

5.2.3 Boundary conditions for electron transport

An electron reaching one of the extreme vertical boundaries (see fig. 5.2) is absorbed and randomly re-injected at the other side in GaAs with a hemi-Maxwellian distribution. An electron reaching the top boundary in AlGaAs (the 'gate') is absorbed and in the same way re-injected at the left (the 'source'). At the bottom boundary in GaAs specular reflection will take place.

At the heterointerface two possibilities exist. An electron may either cross the potential barrier, changing material, or reflect specularly against the interface.

The former is called 'real space transfer' and occurs under the condition of conservation of energy and wave vector parallel to the interface (Wang and Hess 1985). The above condition reads for an electron initially in the GaAs

$$W_G - \Delta W_c - \frac{\hbar^2 k_{\parallel,G}^2}{2m_{AG}^*(1 + \alpha_{AG} W_{AG})} > 0. \tag{5.9}$$

Here W_G and W_{AG} denote the kinetic energies in GaAs and AlGaAs, $k_{\parallel,G}$ the wave vector parallel to the interface in GaAs, α_G the non-parabolicity factor in GaAs and m_{AG}^* the effective mass in AlGaAs.

It applies equally to electrons in either valley, where energies and wave vectors are taken with respect to the bottom of the valley concerned. Furthermore, an electron experiencing real space transfer is assumed to stay in the same valley.

The boundary conditions mentioned in this subsection are represented symbolically by the arrows in fig. 5.2.

5.3 Results

Typically the range of the Al-content x of $Al_xGa_{1-x}As$/GaAs systems studied is 0.3–0.35. In this work an Al-content of x=0.35 has been chosen. As a consequence the energy barriers for the Γ-, L- and X-valleys are 0.269, 0.09 and -0.11 eV, respectively (see also fig. 5.4). The higher the Al-content the higher the energy barrier between GaAs and AlGaAs; for x = 0.3 the respective barriers are 0.227, 0.07 and -0.095 eV. The real space transfer effects which are reported in the following depend on the height of the barrier. However, the differences in the energy barriers for x=0.3 and x=0.35 are not very high and general conclusions can be drawn only from studying the present system.

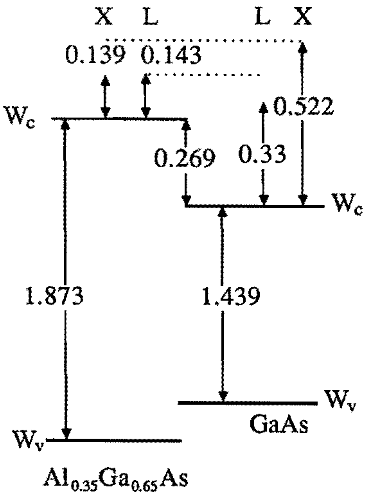

Fig. 5.4 *Schematic energy band diagram of the $Al_{0.35}Ga_{0.65}As/GaAs$ heterojunction. Furthermore, the energy levels for the different valleys are shown.*

chosen in order to be able to study the effects of the interface only, with a minimal influence of injection and absorption of electrons.

Each simulation starts with all electrons in the Γ-valley of GaAs, randomly positioned near the interface, halfway between 'source' and 'drain'. The state of the electron is selected from a Maxwell–Boltzmann distribution at the lattice temperature. The number of simulation particles is equal to 5000 in each case, and the field-adjusting time step has a value of 0.025 ps.

From this initial condition the electrons are left with no external field applied during 5 ps. In this way bend bending becomes established self-consistently. The state thus obtained serves as the thermodynamical equilibrium condition of the heterojunction.

Then a longitudinal field is switched on and the electron system is studied during 15 ps. This period is sufficient to ensure a steady-state condition at the end.

In figs. 5.5–5.7 the steady-state characteristics of kinetic energy, longitudinal velocity and Γ-valley occupancy as a function of the longitudinal field are shown for the GaAs electrons in the heterojunction and for bulk GaAs (see chapter 4), at a temperature of 300 K. In the heterojunction case, results are shown for an ionized impurity density in AlGaAs of 10^{15} and 10^{17} cm^{-3}. The GaAs is assumed to be undoped. The gate voltage equals 0.5 V.

The width of the 'potential well' formed at the interface is in the order of 0.5 μm for $N_D^+ = 10^{15}$ cm^{-3} and 0.2 μm for $N_D^+ = 10^{17}$ cm^{-3}. These values have been determined at the position where the electron density at the interface has reached half of its peak value. For $N_D^+ = 10^{15}$ cm^{-3} the values of the electron concentration at this position equal $7.5 \cdot 10^{15}$ cm^{-3}, respectively $1.5 \cdot 10^{15}$ cm^{-3} at electric fields of 5 kV/cm and 10 kV/cm. When $N_D^+ = 10^{17}$ cm^{-3} these values have become, respectively, $10 \cdot 10^{18}$ cm^{-3} and $1.5 \cdot 10^{18}$ cm^{-3}. The width of the 'potential well' in these cases is much larger than the limit for energy quantization to occur (which limit is in the order of 400 Å).

At all fields in excess of 2 kV/cm, the velocity in the heterojunction has a significantly higher value than in the bulk material. At the same time, the energy is lower and the Γ-valley occupancy is higher. Especially the Γ-valley energy and velocity are affected. This is in particular shown in figs. 5.8 and 5.9. In these figures the average steady-state kinetic energy and velocity, respectively, both in the Γ-valley, are shown. One can see that the Γ-valley energies for $N_D^+ = 10^{17}$ cm^{-3} are more below the bulk value than for $N_D^+ = 10^{15}$ cm^{-3}. At the same time, the Γ-valley velocities

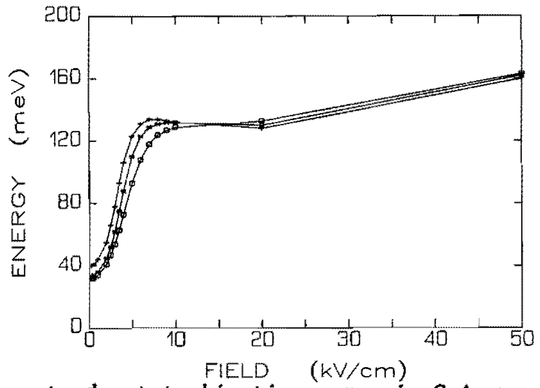

Fig. 5.5 *Average steady-state kinetic energy in GaAs versus electric field, at 300 K, + - bulk GaAs, * - GaAs side of the heterojunction, $N_D^+ = 10^{15}$ cm^{-3}, o - GaAs side of the heterojunction, $N_D^+ = 10^{17}$ cm^{-3}.*

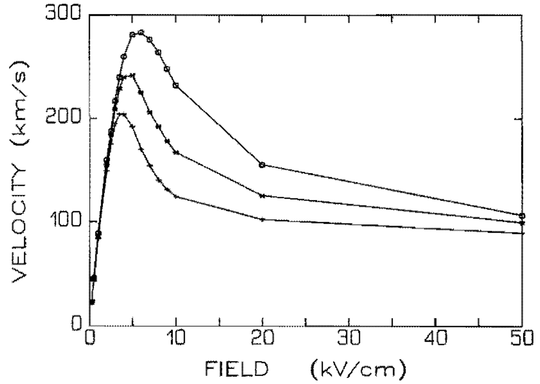

Fig. 5.6 *Average steady-state velocity in GaAs versus electric field, at 300 K. The symbols have the same meaning as in fig. 5.5.*

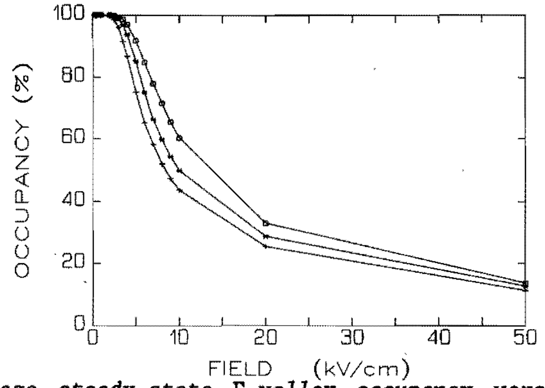

Fig. 5.7 *Average steady-state Γ-valley occupancy versus electric field in GaAs, at 300 K. The symbols have the same meaning as in fig. 5.5.*

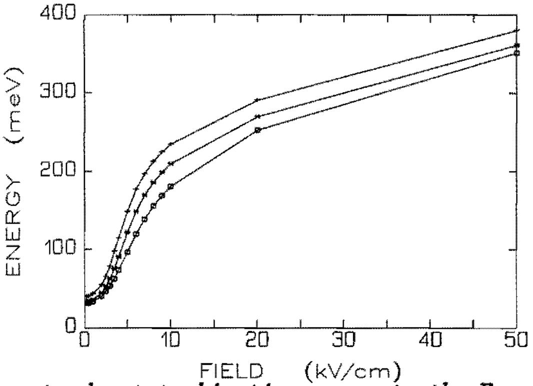

Fig. 5.8 *Average steady-state kinetic energy in the Γ-valley in GaAs versus electric field, at 300 K, + - bulk GaAs, * - GaAs side of the heterojunction, $N_D^+ = 10^{15}$ cm^{-3}, o - GaAs side of the heterojunction, $N_D^+ = 10^{17}$ cm^{-3}.*

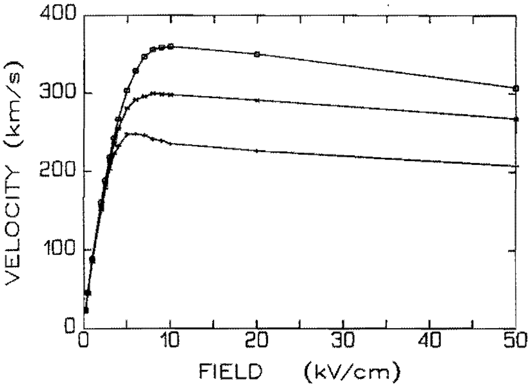

Fig. 5.9 *Average steady-state velocity in the Γ-valley in GaAs versus electric field, at 300 K. The meaning of the symbols is the same as in fig. 5.8.*

for $N_D^+ = 10^{17}$ cm^{-3} have increased more above the bulk values than for $N_D^+ = 10^{15}$ cm^{-3}.

Both the higher Γ-valley occupancy and the higher Γ-valley velocity contribute to the higher overall velocity. This effect becomes more pronounced at higher AlGaAs doping densities, and it also occurs at 77 K (Nederveen and Van de Roer 1988).

In carrying out measurements the distinction between electrons in GaAs or AlGaAs cannot be made. Therefore, in figs. 5.10 and 5.11 in addition to velocity values for electrons in bulk GaAs and electrons in GaAs in the heterojunction, the total velocity parallel to the heterointerface, averaged over GaAs and AlGaAs is shown. As can be seen in these figures, the total velocity is lower than the velocity in GaAs only. This is what is expected, since the AlGaAs is a low-mobility material. However, this total velocity is still considerably higher than in the bulk.

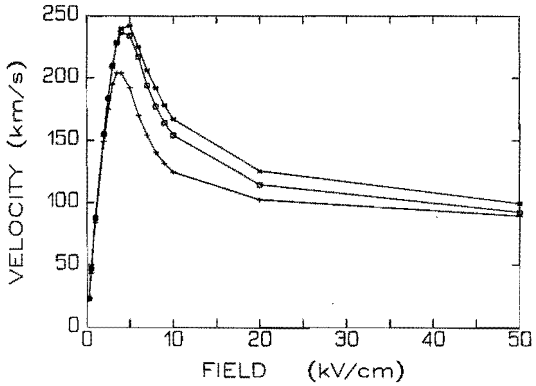

Fig. 5.10 *Average steady-state velocity at 300 K, $N_D^+ = 10^{15}$ cm^{-3}.*
+ - *bulk GaAs*, * - *GaAs side of the heterojunction*,
o - *averaged over both sides of the heterojunction.*

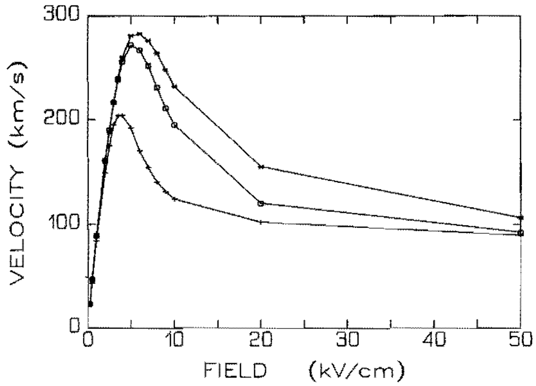

Fig. 5.11 *Average steady-state velocity at 300 K, $N_D^+ = 10^{17}$ cm^{-3}.*
+ - *bulk GaAs*, * - *GaAs side of the heterojunction*,
o - *averaged over both sides of the heterojunction.*

In table 5.1 the rates of occurrence for the scatter processes in GaAs are shown, for an AlGaAs doping density of 10^{17} cm^{-3}. A comparision with table 4.2 learns that polar optical phonon emission and Γ to L intervalley scattering have been reduced. Both reductions can be explained as a result of the lower energy.

Especially the latter process has a large influence on velocity. It is a velocity randomizing process. So, when there are less electrons in the L-valley, in steady-state less electrons transfer from L to Γ and contribute to velocity randomization. Hence, velocity is higher.

Two mechanisms cause the above reduction in energy.

To begin with the transverse electric field, caused by bend bending and gate voltage. It has been found that the wave vector component transverse to the interface is consistently smaller than its corresponding values in the bulk. This is caused by the transverse field, which keeps, in combination with the potential barrier, the electrons from reaching values as high as in bulk. As a result total kinetic energy is lowered.

Secondly, real space transfer has an influence on the average energy. For $Al_{0.35}Ga_{0.65}As$ the value of ΔW_c is about 0.22 eV, which is much lower than the Γ–L energy separation of 0.33 eV. Hence, real space transfer competes with intervalley scattering. Higher energy electrons disappear from the Γ-valley, thereby lowering the average energy in the Γ-valley, and therefore they will not contribute to velocity randomization as described above.

Table 5.1 *The average occurrence, per electron, per valley, of the basic scatter processes in GaAs in the heterojunction, at 300 K. The AlGaAs doping density is 10^{17} cm^{-3}. Electric field strengths are 1, 5 and 10 kV/cm. Steady-state conditions are considered, and the results apply to a time interval of 0.1 ps.*

	1 kV/cm		5 kV/cm		10 kV/cm	
	Γ	L	Γ	L	Γ	L
# electrons	5000		4456	398	2456	1607
Ace	0.01		0.02	0.15	0.03	0.17
PE	0.01		0.01	0.02	0.01	0.02
POPA	0.24		0.22	0.42	0.20	0.43
POPE	0.17		0.42	0.42	0.55	0.53
g-LA	0.0		0.01	0.05	0.07	0.05
g-LE	0.0		0.01	0.13	0.08	0.14
g-XA	0.0		0.0			
g-XE	0.0		0.0			
L-LA				0.29		0.31
L-LE				0.27		0.38
L-XA				0.0		> 0
L-XE				0.0		> 0
NPOPA	0.0		0.0	0.01	0.0	0.01
NPOPE	0.0		0.0	0.01	0.0	0.01

That both mechanisms have an effect can be verified by successively varying the gate voltage, conditions for real space transfer and the doping density in the AlGaAs. In table 5.2 results for gate voltages of 0.3 and 0.5 V are compared for different doping densities, where real space transfer is alternatingly turned on and off (in the latter case no real space transfer at all is allowed).

Table 5.2 *Steady-state velocities in bulk GaAs* ($N_D^+ = 0$) *and in the heterojunction for two values of* N_D^+. *In the heterojunction also two values of* V_G *have been applied, and real space transfer has been turned on (+) and off (-). All simulations have been done for three different values of electric field E.*

N_D^+ (cm^{-3})	0	10^{15}				10^{17}			
real space transfer		+	+	-	-	+	+	-	-
gate voltage (V)		.3	.5	.3	.5	.3	.5	.3	.5
E (kV/cm)	velocity (km/s)								
1	84	83	87	83	84	89	89	89	90
5	192	213	242	203	229	270	281	263	271
10	124	142	167	129	145	206	232	190	207

As can be concluded from this table, the velocity enhancement increases with increasing transverse field. The increase of transverse field is caused either by an increased gate voltage, or by an increased band bending as a result of higher AlGaAs doping. On the other hand, turning off real space transfer, decreases the velocity enhancement.

In table 5.3 results are shown which further verify the fact that real space transfer affects the velocity in the heterojunction. Bulk and heterojunction simulations have been performed with the Γ–L separation temporarily set to 0.15 eV, in order to force electrons to prefer intervalley scattering above real space transfer. This lowering of the Γ–L gap is preferred above an increase of the barrier height, because this would affect the transverse field.

Table 5.3 *Steady-state velocities in bulk GaAs ($N_D^+ = 0$) and in the heterojunction for two values of N_D^+. In the heterojunction also two values of V_G have been applied, and real space transfer has been turned on (+) and off (-). All simulations have been done for two different values of electric field E. The Γ–L separation has been set to 0.15 eV, in this case.*

N_D^+ (cm^{-3})	0	10^{15}				10^{17}			
real space transfer		+	+	-	-	+	+	-	-
gate voltage (V)		.3	.5	.3	.5	.3	.5	.3	.5
E (kV/cm)	velocity (km/s)								
5	108	116	133	115	133	113	173	114	172
10	88	91	100	91	100	90	131	90	131

As expected, the influence of real space transfer on the velocity has been practically disappeared, and only the transverse field effect remains.

5.4 Conclusion

In this chapter the occurrence of higher steady-state velocities in the GaAs part of an AlGaAs/GaAs heterojunction, compared to undoped bulk GaAs, has been discussed. This is caused by a reduction in intervalley transfer due to both the transverse field and real space transfer.

Similar effects in Monte Carlo simulations on AlGaAs/GaAs layered heterostructures have been reported earlier (Littlejohn et al. 1983), but the conclusions then were tentative. In this work those results have been confirmed and an extended explanation has been given.

In practical circumstances these effects could be obscured by other mechanisms, such as degeneracy, electron—electron scattering or energy quantization, but they would still be present.

As regards the influence of degeneracy, as concluded in chapter 4 degeneracy would push the electron energy distribution towards higher energies, so the reduction of intervalley scattering would be (partly) neutralized. Electron—electron scattering, on the other hand, would counteract the influence of degeneracy as regards the occurrence of intervalley scattering.

However, as the electron distribution is not homogeneous in the heterojunction, it is very difficult to take these two mechanisms into account.

The results reported here seem to be in contrast with measurements on AlGaAs/GaAs heterostructures by Masselink et al. (1988). Masselink et al. (1988) found lower, instead of higher, velocities in a two-dimensional electron gas compared to bulk GaAs. One reason for the discrepancy between the results of the present work and theirs could be the above-mentioned simplifications in the physical model (neglect of degeneracy, electron—electron scattering and energy quantization). Another factor which may have an influence may be the fact that the measurements by Masselink et al. are microwave measurements, which tend to yield lower velocity values than the steady-state ones.

Chapter 6

HIGH ELECTRON MOBILITY TRANSISTOR

6.1 A description of the HEMT

The potential of modulation doped AlGaAs/GaAs heterostructures, grown by Molecular Beam Epitaxy (MBE) (Panish and Cho 1980), has been clear since Dingle and co-workers (Dingle et al. 1978) discovered an increased electron mobility in the two-dimensional electron gas formed in undoped GaAs at the AlGaAs heterointerface. Since then, based upon these structures, several laboratories have been developing field-effect transistors (FETs), which have become known under such names as: 'modulation doped FET' (MODFET), 'selectively doped heterojunction transistor' (SDHT), 'two-dimensional electron gas FET' (TEGFET), 'heterostructure FET' (HFET) or 'high electron mobility transistor' (HEMT). Since the first one reported was referred to as HEMT (Mimura et al. 1980), solely this acronym will be used in the following.

HEMT technology is still improving (Morkoç 1984, Mimura et al. 1986, Eastman 1988), but already, compared with the conventional GaAs metal-electrode semiconductor FET (MESFET) with the same dimensions the noise figures are lower and the gain at microwave frequencies higher. Switching speeds in the order of 10 ps have already been obtained, consuming about 10^{-15} J of energy. The potential areas of application are in high-speed digital systems (mainframes or supercomputers) operating at 77 K, or as analog low-noise transistors at microwave frequencies (higher than 100 GHz).

The basic geometry is schematically shown in fig. 6.1. The device is grown on a semi-insulating GaAs substrate and consists of, successively, an unintentionally doped GaAs layer, a so-called spacer and a heavily doped N-AlGaAs layer. The spacer, consisting of undoped AlGaAs, enlarges the mobility of the electrons in the GaAs conduction channel by increasing the distance of the electrons from the ionized impurities in the AlGaAs.

For optimum device performance and reliable operation, the source and drain contacts should be low-resistance ohmic contacts. A widely used method nowadays is the alloy regrowth technique (Robinson 1985), using the Au–Ge–Ni system which has the lowest specific resistance and the highest reliability. During the heat-treatment process the Ge diffuses into the semiconductor forming an n^+ region which overlaps the two-dimensional electron gas at the heterointerface. The gate contact is a Schottky barrier junction, realized by depositing a metal film of e.g. Ti–Pt–Au on top of the AlGaAs surface.

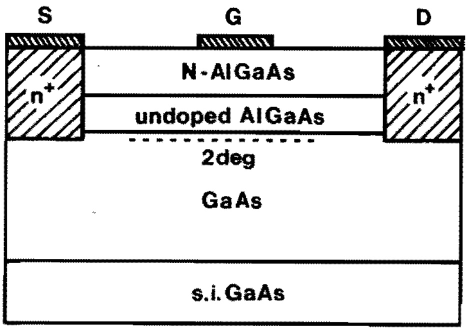

Fig. 6.1 *Cross-section of the High Electron Mobility Transistor.*

Recently other methods for the ohmic contacts have been proposed which rely on a heavily doped n-type GaAs layer deposited on top of the AlGaAs. The metal contact should be alloyed lightly and should not reach through the heterojunction, since this would increase the contact resistance (Fritzsche 1988). Of course in this case the GaAs has to be etched away in the gate region.

6.2 Modified Timestep Cycle

The main difference between one- and two-dimensional modelling is, of course, the fact that Poisson's equation in the latter case has to be solved in two dimensions. In combination with the basic Monte Carlo scheme as described in chapter 2 one arrives at the so-called Modified Timestep Cycle (Hockney and Eastwood 1981). The cycle describes the various tasks to be performed in one so-called field-adjusting time step. It reads

1. Assign charge to the mesh
2. Solve Poisson's equation and calculate the electric field
3. Move all electrons subsequently in reciprocal space as well as in real space during the field-adjusting time step by means of the Ensemble Monte Carlo method
4. Go to 1.

In the following the first two steps of the cycle are explained, in this order. The third step has been treated in chapter 2.

6.2.1 Charge assignment

For the purpose of the two-dimensional solution of Poisson's equation the area under investigation will be divided in a uniform rectangular mesh, see fig. 6.2, with the mesh increments in x- and y-direction denoted by HX and HY, respectively. The indices (i,j) of the mesh points in fig. 6.2 range from 0 to NX in the x-, and from 0 to NY in the y-direction, where NX and NY should both be a power of 2. The latter requirement stems from the fact that in the program used for the two-dimensional solution of Poisson's equation the Discrete Fourier Transform is applied.

Each mesh point is the centre of a rectangular cell with dimensions HX, HY. In the 'cloud-in-cell' (CIC) charge assignment scheme the charge of one electron is spread out over the four nearest mesh points, with for each mesh point a weight factor determined by the overlap of an imaginary cell (HX, HY) with the electron in the middle (the hatched area in fig. 6.3) and the four cells related to the mesh points.

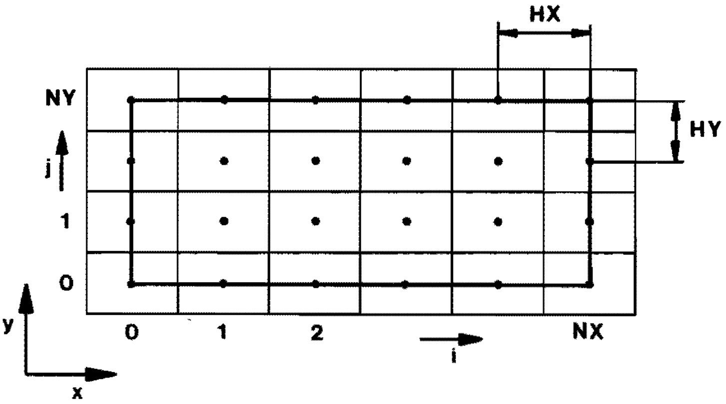

Fig. 6.2 *The area under investigation is divided into a mesh of (NX + 1)·(NY + 1) points. The mesh cell increments in x- and y-direction are, respectively, HX and HY.*

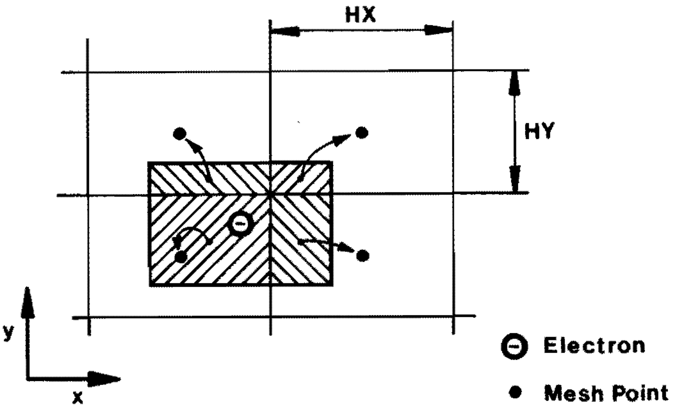

Fig. 6.3 *Principle of the cloud-in-cell charge assignment scheme. The charge of an electron is divided over the four nearest mesh points. As is easily understood from the figure, an alternative name is 'area weighing' scheme.*

It is easy to verify that the contribution $d\rho(x,y)$ of one electron (being at a point (x_p,y_p)) to the charge density (per m^2) in a mesh point (x,y) is given by

$$d\rho(x,y) = \frac{Q_c}{HX \cdot HY} \, V\left(\frac{x - x_p}{HX} \right) V\left(\frac{y - y_p}{HY} \right), \tag{6.1}$$

with

$$V(z) = \begin{cases} 1-|z| & |z| \le 1 \\ 0 & |z| > 1 \end{cases} . \tag{6.2}$$

In addition, the charge Q_c of a carrier is given by

$$Q_c = - \frac{e \, N_f}{M}, \tag{6.3}$$

where N_f denotes the real number of carriers meant to be represented by M simulation particles.

For the assignment of the charges of fixed ionized impurities with density N_D^+ the charge $N_D^+ \cdot HX \cdot HY$ that is to be divided over four mesh points, is considered to be fixed in the middle between the four mesh points. Suppose, for instance, that the area in fig. 6.2 as a whole has an impurity density of N_D^+. Then, with the impurities homogeneously spread out over the area, the contribution to the inner mesh points equals N_D^+, to the corner mesh points $\frac{1}{4}N_D^+$ and the other outer edge mesh points $\frac{1}{2}N_D^+$.

6.2.2 *Poisson's equation*

In order to solve the two-dimensional Poisson equation

$$\frac{\partial^2\phi}{\partial x^2} + \frac{\partial^2\phi}{\partial y^2} = \frac{-\rho}{\epsilon_0\epsilon_s} \qquad (6.4)$$

in the rectangular mesh as described in the previous paragraph, the five-point finite difference form of this equation is used:

$$\frac{\phi_{i-1,j} - 2\phi_{i,j} + \phi_{i+1,j}}{HX^2} + \frac{\phi_{i,j-1} - 2\phi_{i,j} + \phi_{i,j+1}}{HY^2} = -\frac{\rho_{i,j}}{\epsilon_0\epsilon_s}, \qquad (6.5)$$

where $\phi_{i,j}$ and $\rho_{i,j}$ denote, respectively, the electrostatic potential and the charge density on the mesh point (iHX,iHY).

In this work the program POT4A by Beard and Hockney (1985) has been used for solving this equation. It is a so-called Rapid Elliptic Solver, designed to solve eq.(6.5) in a rectangular region using Hockney's Fourier Analysis Cyclic Reduction (FACR) scheme, with one level of odd-even reduction. The effect of electrodes and changes in dielectric constant are taken into account using a numerical capacity matrix technique (Hockney and Eastwood 1981). With regard to speed of solution, the FACR scheme is especially suited to the kind of problems encountered in device modelling.

6.3 Stability

In all calculations connected to a 2D mesh, quantities are discretized in space as well as in time. In this paragraph, in combination with the inevitable rounding errors, the effect of the discretization errors on the stability of the calculations is considered. Regarding instability four major sources are distinguished, i.e.,

1) the kind of the so-called time integration scheme
2) the time discretization
3) the space discretization
4) the charge assignment.

Furthermore, the sources affect each other. For some of them theoretical stability criteria can be formulated, for the others one has to rely on empirical criteria. In the following the four error sources will be treated in the same order as above, where sources 2 to 4 are related in such a high degree that they are treated together in one paragraph.

6.3.1 Effect of time integration

The particles considered in any simulation move in general in space and time according to Newton's laws of motion.

$$\frac{d\vec{x}}{dt} = \vec{v}, \qquad (6.6)$$

and

$$m \frac{d\vec{v}}{dt} = \vec{F}. \tag{6.7}$$

For the purpose of stability analysis and neglecting non-parabolicity effects, these equations will be written as,

$$\frac{d\vec{x}}{dt} = \frac{\hbar\vec{k}}{m^*} , \tag{6.8}$$

and

$$\frac{\hbar d\vec{k}}{dt} = -e\vec{E} , \tag{6.9}$$

respectively. In the present work eqs.(6.8) and (6.9) have been discretized in the following way

$$\frac{x_{n+1} - x_n}{DT} = \frac{\hbar k_{n+1}}{m^*} , \tag{6.10}$$

and

$$\frac{\hbar(k_{n+1} - k_n)}{DT} = -eE_n, \tag{6.11}$$

where DT is the discretization timestep. (In fact, DT is the free-flight time of the electron and its maximum value is equal to the field-adjusting timestep defined in section 6.2.) This scheme, called the time integration scheme, may be evaluated considering consistency, accuracy, stability and efficiency (Hockney and Eastwood 1981).

In the following the main topic will be the stability of this time integration scheme. Stability is concerned with the propagation of errors, due to truncation and roundoff.

Writing eq.(6.11) in terms of position only, one obtains

$$\frac{\hbar(k_{n+1} - k_n)}{DT} = \frac{m^*}{DT^2}(x_{n+1} - 2x_n + x_{n-1}) = - eE_n = F(x_n). \tag{6.12}$$

Defining the exact solution of this equation by X_n ($n=0,\ldots,N$) and the resulting approximate solution by x_n, the roundoff error, is given by

$$\epsilon_n = x_n - X_n. \tag{6.13}$$

Substitution of eq.(6.13) in eq.(6.12) yields, after subtraction of the exact solution,

$$\frac{m^*}{DT^2}(\epsilon_{n+1} - 2\epsilon_n + \epsilon_{n-1}) = F(X_n+\epsilon_n) - F(X_n) = \epsilon_n \frac{\partial F}{\partial x}\bigg|_{x=X_n}, \tag{6.14}$$

where the roundoff error ϵ_n is assumed to be sufficiently small to justify the Taylor expansion in the right hand side of eq.(6.14).

Equation (6.14) is difficult to solve, unless $\frac{\partial F}{\partial x}\Big|_{x=X_n}$ is a constant. Because one looks for the worst case only (the question of interest is whether or not the scheme is unstable, not how unstable it is) $\frac{\partial F}{\partial x}\Big|_{x=X_n}$ is replaced by its maximum negative value $-\left|\frac{\partial F}{\partial x}\right|_{max}$, the minus-sign arising from the assumption that the solution be oscillatory. Thus, eq.(6.14) becomes

$$\epsilon_{n+1} - 2\epsilon_n + \epsilon_{n-1} = - \frac{1}{m^*}\left|\frac{\partial F}{\partial x}\right|_{max} DT^2\epsilon_n = - \Omega^2 DT^2 \epsilon_n. \tag{6.15}$$

Taking as a trial solution $\epsilon_n = \lambda^n = \exp(i\omega nDT)$, the following characteristic equation is obtained

$$\lambda^2 - 2\lambda + 1 = - \Omega^2 DT^2 \lambda, \tag{6.16}$$

having solutions λ_+ and λ_-. The general solution will be of the form $\epsilon_n = a\lambda_+^n + b\lambda_-^n$. Now, if either $|\lambda_+|$ or $|\lambda_-|$ were greater than unity the error would propagate and grow exponentially. Hence, one can conclude that for the time integration scheme to be stable, the characteristic solutions λ_+ and λ_- should be located inside or on the unit circle. This condition is fulfilled if $\Omega DT < 2$, where Ω is the highest frequency of interest in the simulated medium. In a semiconductor this is the plasma frequency (Hockney and Eastwood 1981).

It is interesting to take a closer look at two other possible time integration schemes.

The first one to be considered is the one proposed by Hockney and Eastwood (1981), being

$$\frac{x_{n+1} - x_n}{DT} = \frac{\hbar}{2m^*} (k_{n+1} + k_n), \tag{6.17}$$

$$\frac{\hbar(k_{n+1} - k_n)}{DT} = F(x_n). \tag{6.18}$$

In exactly the same way as described above, this leads through

$$x_{n+1} - 2x_n + x_{n-1} = \frac{DT^2}{2m^*} [F(x_n) + F(x_{n-1})], \tag{6.19}$$

to the error propagation formula

$$\epsilon_{n+1} - 2\epsilon_n + \epsilon_{n-1} = - \frac{DT^2\Omega^2}{2} (\epsilon_n + \epsilon_{n-1}), \tag{6.20}$$

resulting in the following characteristic equation

$$\lambda^2 - 2\lambda + 1 = - \frac{DT^2\Omega^2}{2} (\lambda + 1). \tag{6.21}$$

Defining $A = DT^2\Omega^2/2$, the solution is

$$\lambda_{\pm} = 1 - \frac{A}{2} \pm \frac{A}{2}\sqrt{1 - 8/A} \ . \tag{6.22}$$

With A in (0,8] the solutions λ_+ and λ_- are complex conjugated

$$\lambda_{\pm} = 1 - \frac{A}{2} \pm i\frac{A}{2}\sqrt{8/A - 1} \ , \tag{6.23}$$

and $|\lambda| = \sqrt{1+A} > 1$. Hence the time integration scheme is unstable in this range. For $A > 8$ the solutions are real and $|\lambda| = \sqrt{1 - 3A + \frac{1}{2}A^2}$. The minimum value of $|\lambda|$ occurs for $A = 8$, being $|\lambda| = 3$. At no positive value of A ($= DT^2\Omega^2/2$) will $|\lambda|$ be smaller than unity, from which it follows that this scheme is unconditionally unstable.

Another scheme one may be inclined to apply is given by

$$\frac{x_{n+1} - x_n}{DT} = \frac{\hbar}{m^*} k_n \ , \tag{6.24}$$

and

$$\frac{\hbar(k_{n+1} - k_n)}{DT} = F(x_n). \tag{6.25}$$

Analogous to the previous case

$$\frac{m^*}{DT^2}(x_{n+2} - 2x_{n+1} + x_n) = F(x_n). \tag{6.26}$$

This leads to

$$\epsilon_{n+2} - 2\epsilon_{n+1} + \epsilon_n = -DT^2\Omega^2\epsilon_n \ , \tag{6.27}$$

and

$$\lambda^2 - 2\lambda + 1 = -DT^2\Omega^2. \tag{6.28}$$

Taking $A = DT^2\Omega^2$, the solution is

$$\lambda_{\pm} = 1 \pm \sqrt{-DT^2\Omega^2} \; . \tag{6.29}$$

All solutions (for real A) are complex conjugated and

$$|\lambda| = \sqrt{1 + DT^2\Omega^2} > 1 \; . \tag{6.30}$$

Hence, this scheme is unconditionally unstable as well.

6.3.2 Space and time discretization combined with charge assignment

Between scatter events the ensemble of electrons in the computer model may be regarded as a collisionless plasma. The Monte Carlo scheme may be looked upon as if the physical scatter processes are superimposed on the collisionless plasma model. The characteristic times of the latter associated with the rounding errors should be such that the former is not influenced. For collisionless plasmas the influence of the inherent differences between the 'real' plasma and the computer model has been investigated (Hockney and Eastwood 1981).

A 'computer plasma' differs from a real plasma in the particle density (n) and the finite discretization of space (HX and HY) and time (DT). The relation between the real and the approximated quantities is represented by means of a couple of dimensionless quantities of which the first is N_c,

$$N_c = n\lambda_D^2 \left\{ 1 + \frac{HX \cdot HY}{\lambda_D^2} \right\} , \tag{6.31}$$

where λ_D = the Debye wavelength = $\left(\dfrac{\epsilon_0 \epsilon_s k_B T}{e^2 n} \right)^{1/2}$

HX = mesh cell size in x-direction

HY = mesh cell size in y-direction

n = M/A = the number of simulation particles divided by the area in which the simulation electrons represent a known charge density, i.e. the density of simulation electrons.

As can be concluded from the empirical correlations summarized below, N_c is strongly dependent on the charge assignment scheme used.

The other dimensionless quantities are associated with the space discretization, being HX/λ_D and HY/λ_D, and with the time discretization, being $\omega_{pe}DT$. Here ω_{pe} denotes the plasma frequency. The plasma frequency is related to λ_D by $\omega_{pe} = v_T/\lambda_D$, where $v_T = \sqrt{k_B T/m^*}$ is the thermal velocity.

It has been found that two empirical relaxation times describe the behaviour of the computer model, denoted by τ_c and τ_h respectively. The first one, called the 'collision time', is a measure for the time it takes for a particle in a collisionless plasma to reach a value of 90° for the root-mean-square deviation from its trajectory. The second one, called the 'heating time', is a measure for the increase in kinetic energy of a particle in a plasma model. During the heating time the mean energy of the plasma is increased by $\frac{1}{2}k_B T$.

The above collision time, N_c and plasma frequency are found to be related through

$$\tau_c = N_c \tau_{pe}, \tag{6.32}$$

where $\tau_{pe} = 2\pi/\omega_{pe}$.

The relation between τ_h and N_c is made irrelevant by considering τ_h/τ_c. With eq.(6.32) it is always possible to obtain τ_h from τ_h/τ_c. The behaviour of τ_h/τ_c as a function of the dimensionless quantities

H/λ_D, where H may be either HX or HY, and $\omega_{pe}DT$ results in a very complicated picture.

However, taking into account the condition $\omega_{pe}DT < 2$ and introducing $v_T DT/H < 1$, the range of possible values for DT and H is strongly restricted. The latter condition introduces the constraint that an electron with thermal velocity should not cover a distance of more than one mesh cell in time DT.

These conditions define an optimum path in (H,DT)-space, being

$$(\omega_{pe}DT)_{opt.} = \min(\frac{1}{2}\frac{H}{\lambda_D}\ ,\ 1). \tag{6.33}$$

Note that this optimum path is safely chosen halfway the limits posed by the two restrictions mentioned above.

On this path one finds (Hockney and Eastwood 1981)

$$\frac{\tau_h}{\tau_c} = \frac{K_H}{(H/\lambda_D)^2} = \frac{K_H}{HX \cdot HY/\lambda_D^2}\ . \tag{6.34}$$

For the five-point finite difference form of Poisson's equation combined with the CIC scheme for the charge assignment the constant K_H equals 40.

The consequences for a practical simulation are the following.

First one should take care that $\omega_{pe}DT < 2$ and $v_T D/H < 1$. This being the case, one should check that H, DT and M are chosen such that the collision rate $1/\tau_c$ does not interfere with the physical scatter mechanism, i.e., $1/\tau_c < \lambda_{min}$. Subsequently, one calculates the heating time, from which the rate of energy conservation per scatter event may be determined. The restriction posed by the heating time is not very severe, considering the values of the heating time in the usual simulations. One should take care that $\tau_h \gg 1/\lambda_{min}$, from which follows $\tau_h/\tau_c \gg 1$, which usually is the case.

Numerical values will be given in section 6.5, when simulations are presented.

6.4 Boundary conditions

For a correct device simulation boundary conditions have to be provided for the electrodes, the heterointerface and all other (outer) boundaries.

6.4.1 Electrodes

The source and drain potentials are ohmic contacts, as a consequence the contact potentials seen internally in the device are equal to the potentials applied externally. According to Shaw (1981) an ideal ohmic contact is a majority carrier injecting contact, meaning that it is able to supply all the majority carriers demanded by the bulk for any applied electric field. An injecting contact thus acts as a reservoir of carriers at the metal—semiconductor interface that continuously keeps adjusting itself to meet the current levels demanded by the bulk. From this description it is reasonable to impose charge neutrality as a boundary condition in the region adjacent to an electrode, i.e, the electron density there equals the ionized impurity density. This is achieved in the following manner: an ohmic contact is treated as perfectly absorbing, i.e., each simulation electron reaching the contact is absorbed. At the end of each field-adjusting timestep the electrons required to fulfil the condition of charge neutrality in the regions adjacent to the electrodes are injected with velocities drawn from a hemi-Maxwellian distribution.

Each simulation starts with all electrons randomly distributed in the AlGaAs layer such that the electron density equals the ionized impurity density. Since during the first timesteps the depletion layer below the gate still has to be formed, the number of simulation electrons generally will decrease. However, the charge attributed to each electron (eq. 6.3) remains the same throughout the simulation, and is calculated once in the initial state.

The gate electrode is a Schottky barrier contact. An electron which reaches this contact will be absorbed. Furthermore, no injection will take place at this contact.

The most important parameter describing a Schottky barrier is the barrier energy ϕ_B (see fig. 5.3), describing the discontinuity in the energy band diagram at the metal–semiconductor interface. Experimentally it has been found (Robinson 1985) that for GaAs the value of the Schottky barrier height is almost independent of the metal used to form the contact. It is assumed that at the metal–semiconductor interface the Fermi-level is pinned at a certain value due to surface states. Surface states are electronic states localized at the surface of the semiconductor crystal. Several distinctly different physical and chemical models have been proposed to explain Fermi-level pinning. Defect formation, chemical reaction and interdiffusion can all play a role. Therefore it has been very difficult to obtain a simple, self-consistent, comprehensive model for the formation of Schottky barriers on real semiconductors (Robinson 1985). However, recently, Mönch (1988) has presented a very promising model accounting for several distinct mechanisms at the same time.

From measurements on $Al_xGa_{1-x}As$ by Okamoto et al. (1981) the following interpolation formula for ϕ_B in eV has been derived by Balemans (1988)

$$\phi_B = \begin{cases} 0.669 + 1.036x, & \text{for } x \leq 0.36 \\ 1.189 - 0.41x\ , & \text{for } x > 0.36 \end{cases} . \tag{6.35}$$

Then, the boundary condition for the gate electrode is

$$V_{G_{int}} = V_{G_{ext}} - \phi_B/e. \tag{6.36}$$

6.4.2 Heterointerface

The boundary conditions for electron transport at the AlGaAs/GaAs heterointerface have already been described in chapter 5. For the solution of Poisson's equation the continuity of the normal component of the dielectric displacement has to be assured. This is taken care of by the program for the 2D solution of this equation, POT4A.

6.4.3 Outer boundaries

At all other (outer) boundaries the perpendicular component of the electric field is set to zero. Electrons reaching these boundaries reflect specularly, thus representing a zero perpendicular component of the current density.

6.5 Results

6.5.1 Introduction

An Ensemble Monte Carlo device simulator has been developed capable of simulating a High Electron Mobility Transistor (HEMT) with arbitrary rectangular dimensions and with the possibility to define the contact areas in a very flexible manner.

The gate electrode is put on top of the device. The source and drain electrodes both have an adjustable length and depth. Adjacent to each of these electrodes an n^+ region, with minimum length and height of respectively HX and HY, is positioned.

Two possible contact layouts are shown in figs. 6.4 and 6.5.

In fig. 6.4 the area created by the non-zero depth of the electrode represents a metallic region which has been formed by alloying Au–Ge–Ni, and the adjacent area represents the n-doped region caused by the diffusion of Ge. The potentials applied externally are set at the inner boundaries of the metallic regions.

In fig. 6.5 the equivalent of a uniform ion-implanted n^+ region is obtained by setting the depth of the electrode to zero. The voltage applied externally is now set on the top electrodes.

In the following three subsections the parameters will be presented which have been used in the Monte Carlo calculations of the HEMT. These parameters can be distinguished in those concerning the geometry of the device under study, the physics of the semiconductors involved and the Monte Carlo model parameters.

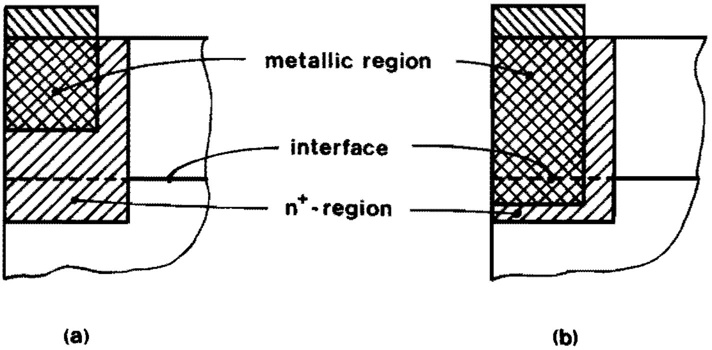

Fig. 6.4 *Contacts formed by alloying are represented by a metal region with an adjacent* n^+ *region, below the metal electrode.(a) The metal region does not reach the GaAs layer, (b) it does reach the GaAs layer.*

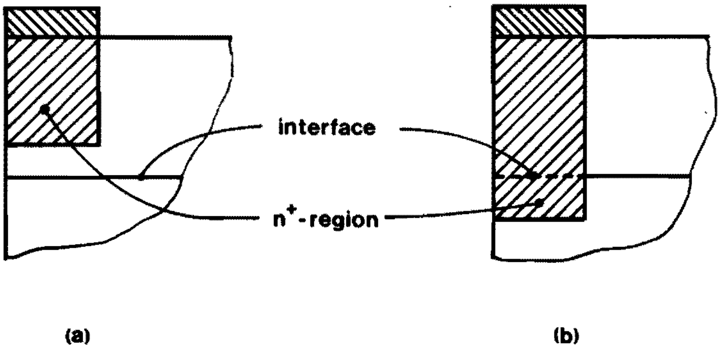

Fig. 6.5 *Contacts formed by ion implantation, consisting of an* n^+ *region below the metal electrode. (a) The* n^+ *region does not reach the GaAs layer, (b) it does reach the GaAs layer.*

Geometrical data

The dimensions of the HEMT under consideration are depicted in fig. 6.6. These dimensions have been taken from Thobel (1988), in order to be able to compare results. The device has a length of 0.96 μm and a total height of 0.32 μm. The GaAs layer is 0.28 μm high. Thus, as there is no spacer layer involved, the height of the AlGaAs layer

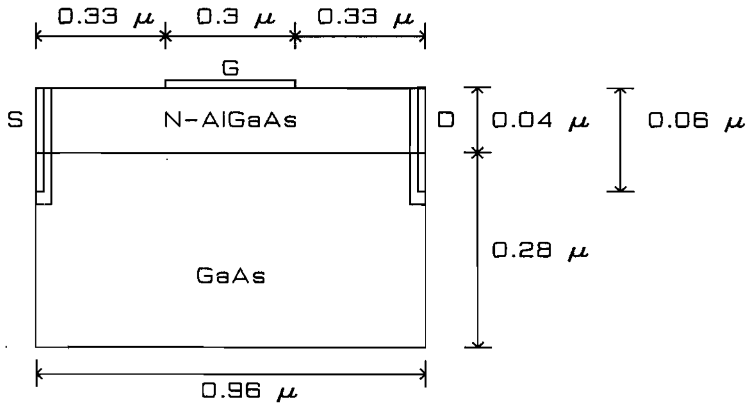

Fig. 6.6 *The dimensions of the simulated HEMT. The length of the source and drain contacts is 0.015 μm.*

equals 0.04 μm. The gate length is equal to 0.3 μm. The length of source and drain being equal to 0.015 μm, the interelectrode spacing becomes 0.315 μm. The depth, 0.06 μm, is such that the contacts reach through the heterojunction. The n^+ regions extend 0.015 μm (HX) in the x-, and 0.0025 μm (HY) in the y-direction.

Furthermore, using this geometry as a starting point, similar devices will be investigated by varying the gate length.

Physical data

The device has been studied at a temperature of 300 K. The Al mol fraction of the AlGaAs is 0.3. The ionized impurity density of $Al_{0.3}Ga_{0.7}As$ is equal to 10^{18} cm^{-3}, whereas the GaAs is supposed to be undoped. These values have been taken from Thobel (1988), in order to be able to compare results.

The conduction bands of GaAs and AlGaAs both are described by a three-valley (Γ-L-X) model, with Kane-type non-parabolicity as treated in chapter 3. The values for the valley separations in both materials are depicted in fig. 6.7. These values have been calculated using the interpolation formulas of table 3.1. This yields for the differences in energy level of the valleys in AlGaAs and GaAs the following values for the Γ-, L- and X-valley: 0.227, 0.07 and -0.095 eV respectively. Thus, e.g., the bottom of the X-valley in GaAs lies above that in AlGaAs.

The scatter processes which have been take into account are: acoustic, polar optical phonon and intervalley scattering, in GaAs as well as in AlGaAs. Furthermore, in AlGaAs also ionized impurity and random potential alloy scattering have been included. The degree of randomness in the latter case has been set to its maximum value by putting $S_o = 1$ (see eq. 3.49).

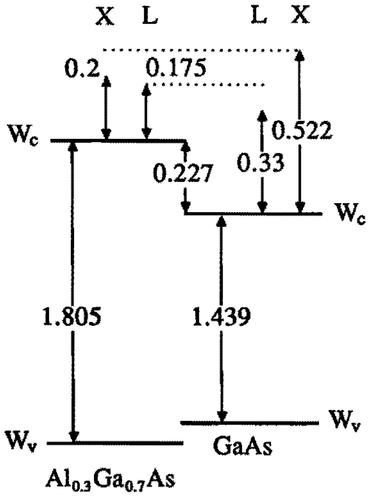

Fig. 6.7 *Schematic energy band diagram of the* $Al_{0.3}Ga_{0.7}As/GaAs$ *heterojunction. Furthermore the energy levels for the different valleys are shown.*

Monte Carlo model parameters

The number of simulation particles present in the model at the beginning of each simulation is 5000. This number may have changed at the end of the simulation due to the build-up of a depletion region below the gate. The numbers of mesh points in the x-, y-direction are 64 and 128 respectively, yielding a mesh cell with a length of 0.015 μm and a height of 0.0025 μm.

The field-adjusting timestep DT is taken as 0.005 ps. The number of steps is 10000, yielding a total simulation time of 50 ps. Summation per mesh point of physical quantities of interest, for instance energy and velocity, starts at 30 ps. This is done for averaging purposes.

As regards stability, with the mesh cell and timestep chosen the following values for the stability criteria result (the required limits are shown between brackets):

$$\begin{aligned}
\omega_{pe}DT &= 0.3129 && (< 2) \\
1/\tau_c &= 1400\ \mathrm{GHz} && (< \lambda_{min}) \\
\tau_h &= 2.4\ \mathrm{ps} && (> DT) \\
v_{th}DT/HX &= 0.09 && (< 1) \\
v_{th}DT/HY &= 0.54 && (< 1)
\end{aligned}$$

The minimum total scatter rate, λ_{min}, occurs in the Γ-valley in GaAs at energies up to the threshold for polar optical phonon emission (0.03536 eV). For those energies the total scatter rate is about 2500 GHz, which still is well above $1/\tau_c$. Thus, all requirements are fulfilled.

6.5.2 DC results for a gate length of 0.3 μm

In fig. 6.8 the I_{DS}–V_{DS} characteristics are presented, for successive gate voltages of -0.2, 0.2 and 0.6 V. As usually with transistor I–V characteristics, a linear, an intermediate and a saturation region can be distinguished. One feature is striking, namely the fact that the saturation voltage is almost a constant. This indicates an early velocity saturation. Furthermore, the flatness of the curve in saturation is unique for such a short-channel device.

In the following, results for the case of V_G = 0.2 V will be presented subsequently showing more detail. With those results serving as an example, in this way the operation of the device will be explained.

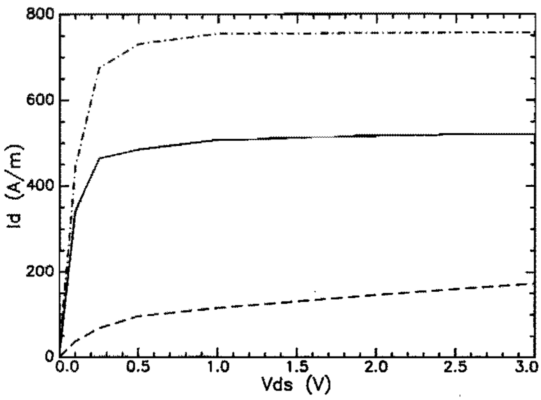

Fig. 6.8 ***I_{DS} versus V_{DS} characteristic for gate voltages of -0.2 V (- -), 0.2 V (—) and 0.6 V (-··-).***

Potential and electric field

In fig. 6.9 equipotential curves are drawn for V_G = 0.2 and V_{DS} being equal to 0.1, 0.5, 1 and 2 V, respectively. In fig. 6.10 the electric field at the AlGaAs/GaAs interface is shown for V_{DS} = 0.5 and 2 V. It can be seen from these plots (both fig. 6.9 and 6.10) that the influence of an increased drain voltage becomes apparent only at the drain end of the gate. There the field strength in the x-direction reaches its maximum value (70 kV/cm for V_{DS} = 2 V). Note that the peak builds up over such a small distance (in the order of 0.1 μm) that the electrons may not be in equilibrium with the lattice during the transit of the high-field region. For instance, the drift velocity relaxation time is in the order of 1 ps when the field is changed from 0 to 10 kV/cm (Warriner 1977b), and decreases with increasing field. An electron with a velocity of 200 km/s undergoing such a field change has to proceed 0.2 μm before having adjusted itself completely to the field.

As mentioned above the potential in the region between source and gate is practically independent of drain voltage. Note that just behind the gate the potential is already 0.4 V for $V_{DS} \geq 0.5$ V, see fig. 6.9. This point represents the pinch-off point, as for higher drain voltages the voltage at this point hardly changes. As a consequence the number of carriers arriving from the source hardly changes anymore. The pinch-off voltage can also be deduced from fig. 6.8.

The electric field in the y-direction is seen to have its maximum negative value at the drain end of the gate. At this point there is an accumulation of carriers caused by a decrease of the velocity (see fig. 6.14). The increase of space charge causes an increase in

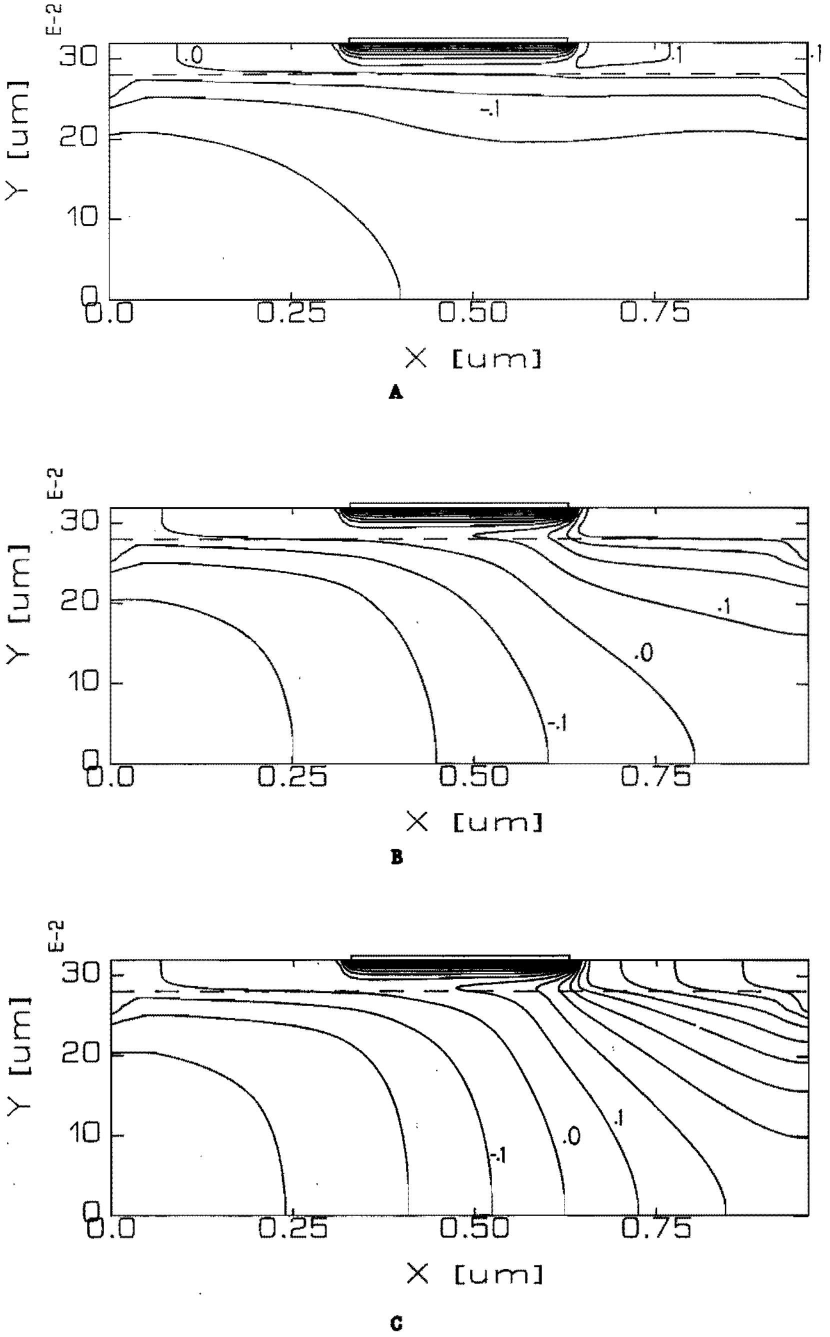

***Fig. 6.9** Equipotential curves for V_G = 0.2 V. (A) V_{DS} = 0.1 V, (B) V_{DS} = 0.5 V, (C) V_{DS} = 1 V, (D) V_{DS} = 2 V (on next page).*

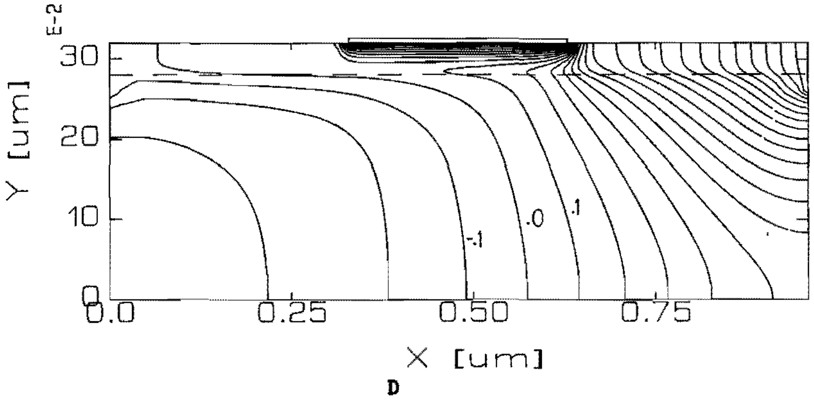

Fig. 6.9 *Equipotential curves for $V_G = 0.2$ V. (D) $V_{DS} = 2$ V.*

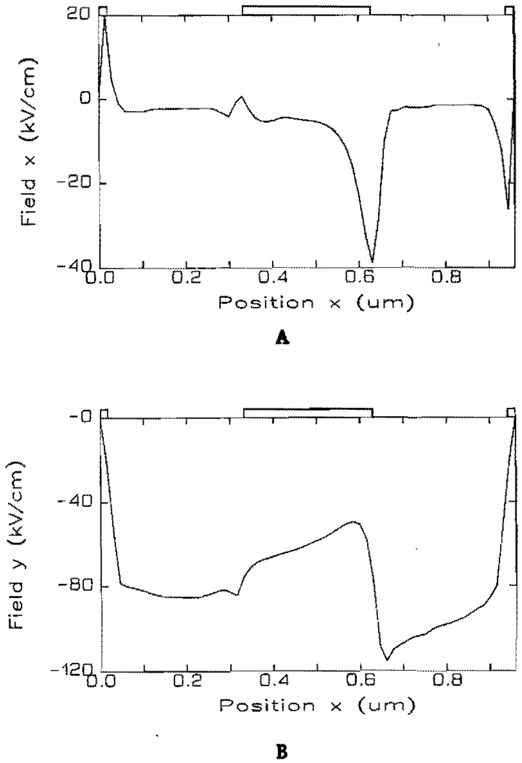

Fig. 6.10 *Electric field strengths along the interface as a function of position for $V_G = 0.2$ V. (A+B) field in the x- and y-direction, respectively at $V_{DS} = 0.5$ V, (C+D) field in the x- and y-direction, respectively at $V_{DS} = 2$ V (on next page).*

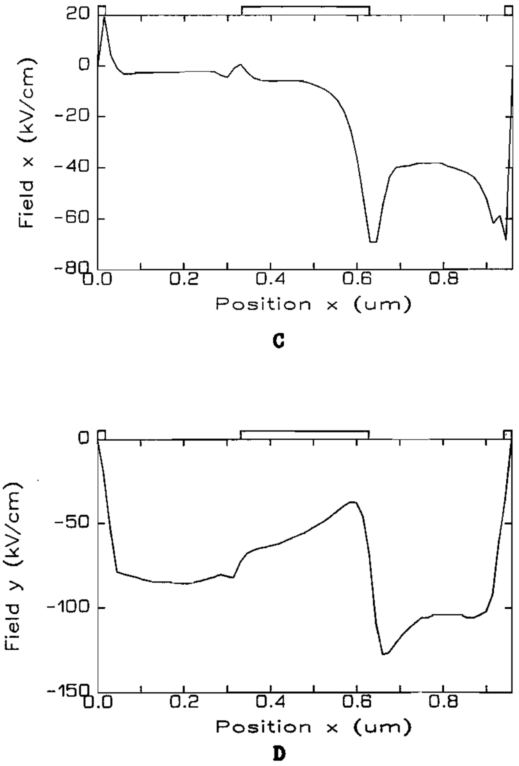

Fig. 6.10 *Electric field strengths along the interface as a function of position for* $V_G = 0.2$ *V. (C+D) field in the x- and y-direction, respectively at* $V_{DS} = 2$ *V.*

the perpendicular component of the electric field, directed such that electrons near the heterointerface in GaAs are pushed towards the interface.

In fig. 6.11 the same information as in the equipotential curves is presented in a 3D plot for $V_{DS} = 0.5$ and 2 V. Note that instead of potential now the conduction band energy level is shown, which implies that the sign has been reversed. Also the conduction band discontinuity at the interface has been added. These pictures provide an instructive insight in the path the electrons are forced to follow. One could imagine the electrons moving like marbles, subject to the law of gravitation, in an area shaped by the profile of the conduction band.

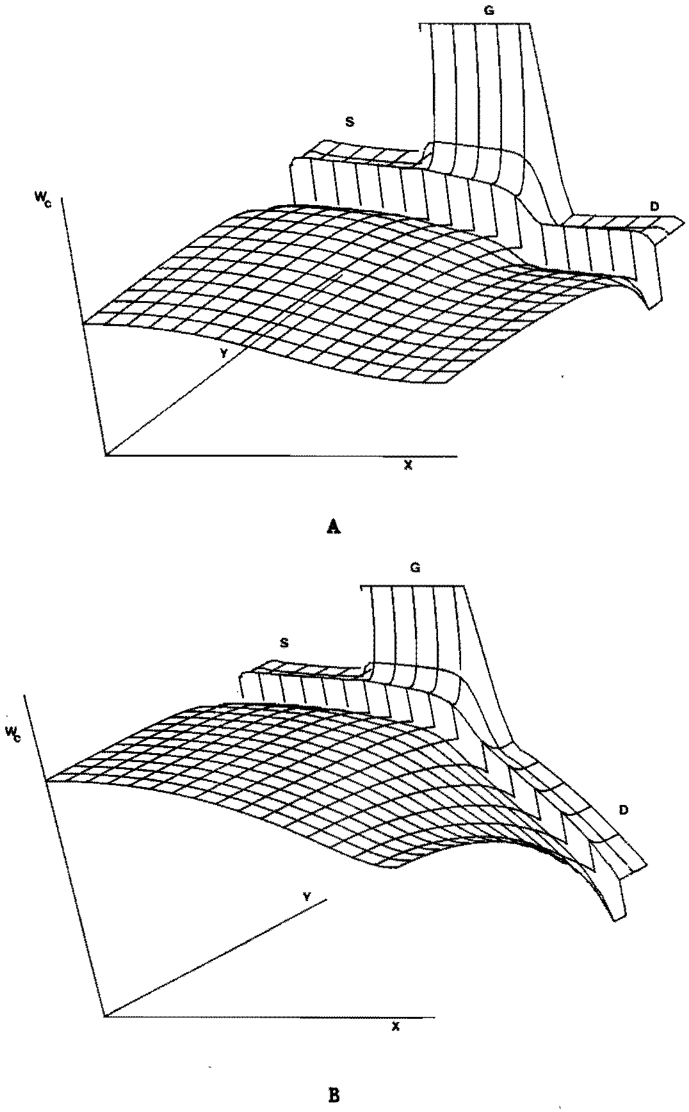

Fig. 6.11 *Conduction band as a function of the x,y position for* $V_G = 0.2$ *V. (A)* $V_{DS} = 0.5$ *V, (B)* $V_{DS} = 2$ *V.*

Swarm plots

The latter idea is visualised in fig. 6.12 by the swarm plots of the electrons in the various valleys, for V_{DS} = 0.5 V. It is seen that at this drain voltage most of the electrons reside in the Γ-valley. Furthermore, about 60 % of the simulation electrons reside in the AlGaAs. However, below the gate practically all electrons are in the GaAs channel. Also, the depletion layer below the gate is clearly visible. Although probably not clear from this picture, most electrons in GaAs are near the interface. Note that these positions are momentary positions after 50 ps.

In the swarm plot for V_{DS} = 2 V (fig. 6.13) the situation has changed considerably. Between source and gate, no change is seen, as is expected from the equipotential curves. However compared to the previous case, behind the gate, the L- and X-valleys have become populated as a consequence of the higher electric field. There, most electrons in GaAs are in the L-valley, and in AlGaAs the L- and X-valleys have become approximately equally populated, whereas the Γ-valley in AlGaAs is practically empty.

In fig. 6.13A, for instance, the boundary condition for the electron density at the contacts can be recognised very clearly from the high concentration of points at especially the drain contact.

Average velocity and electron concentration

In fig. 6.14 the average velocity in GaAs is shown for V_{DS} = 0.1, .25, .5 and 2 V. Especially at the two latter voltages a dynamic overshoot phenomenon is observed, with the half-width of field strength peak being less than 0.05 μm. At 0.5 V the average velocity at the end of the gate is almost the same as at 2 V. The main

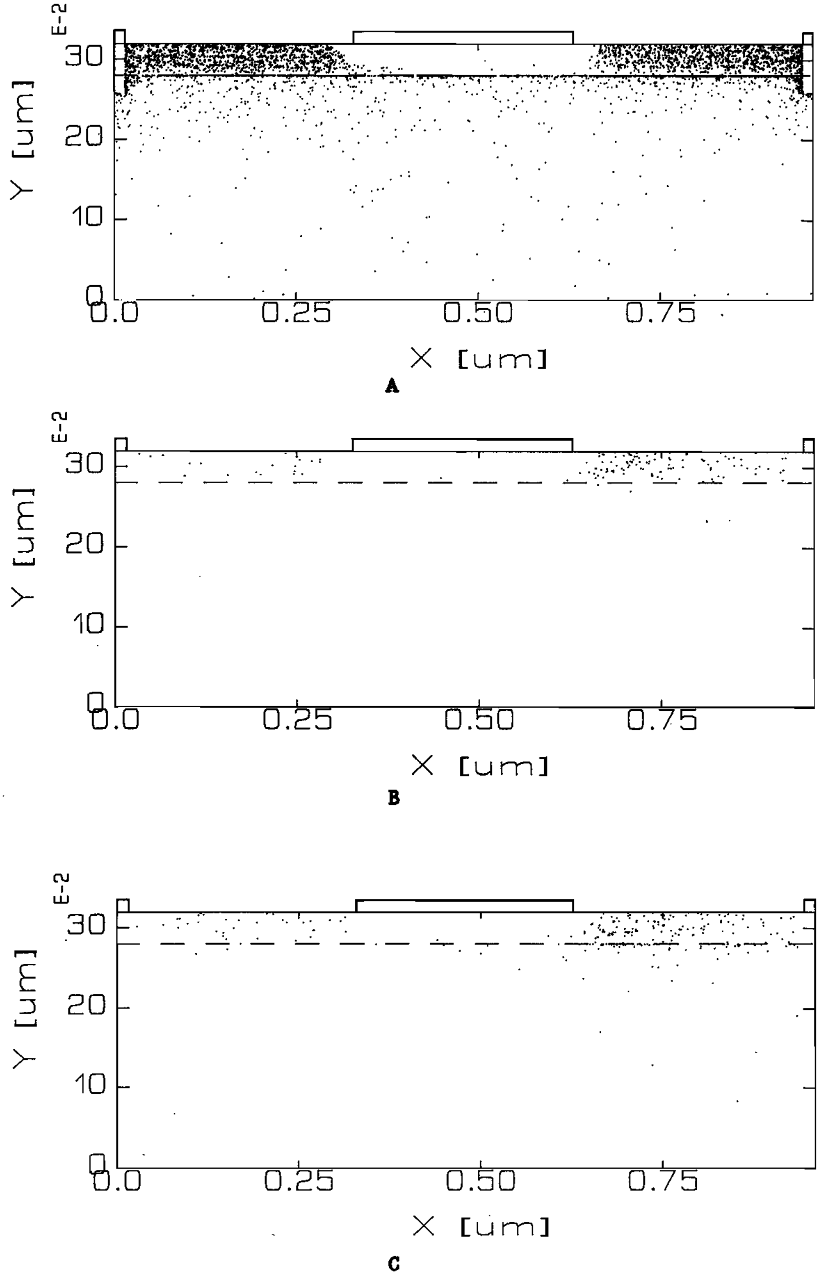

Fig. 6.12 *Swarm plots, showing the momentary position of the simulation electrons for* $V_G = 0.2$ *V,* $V_{DS} = 0.5$ *V. (A+B+C) electrons in the Γ-, L- and X-valley respectively.*

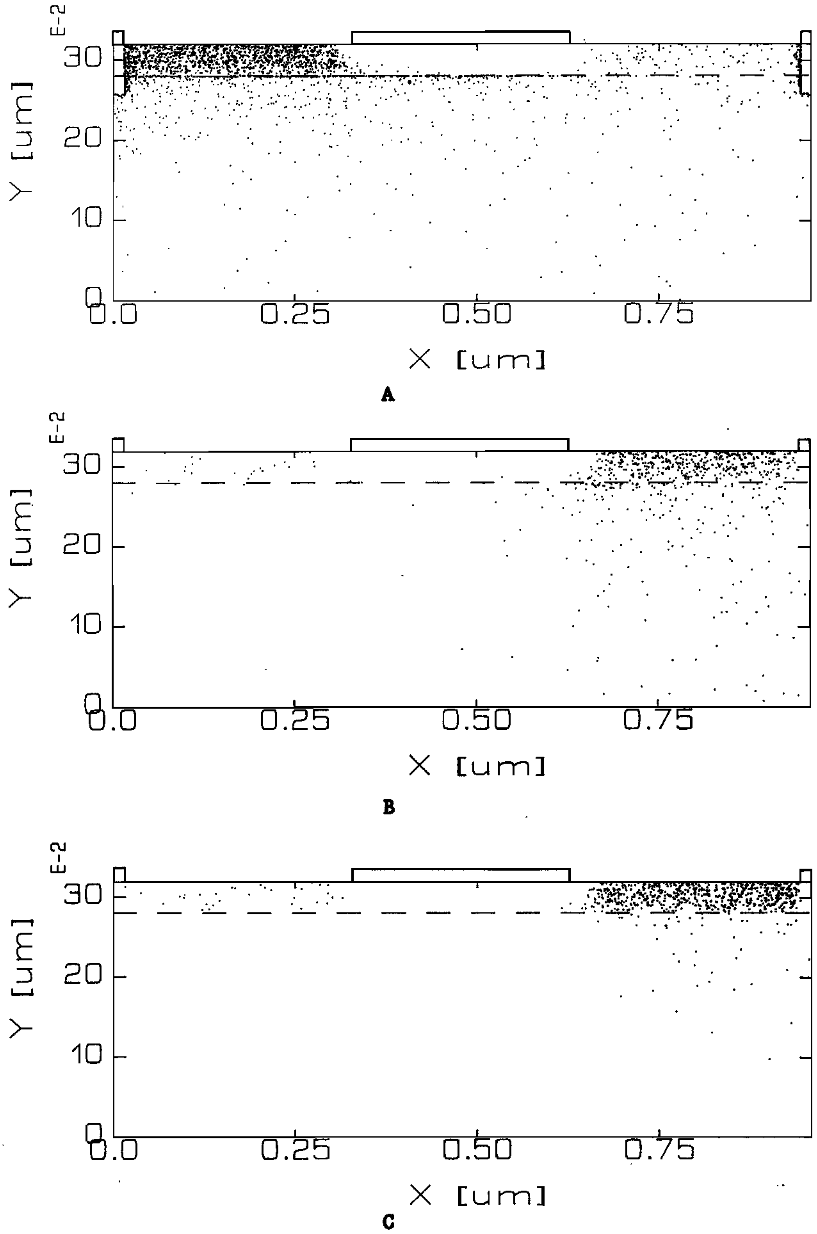

Fig. 6.13 *Swarm plots, showing the momentary position of the simulation electrons for $V_G = 0.2$ V, $V_{DS} = 2$ V. (A+B+C) electrons in the Γ-, L- and X-valley respectively.*

difference is that at 2 V more electrons have been transferred to upper valleys behind the gate, which is the main cause of the decrease in velocity. On the contrary, however, at 0.5 V the velocity decreases because the field in the x-direction practically falls off to zero (see fig. 6.10A).

Note the slight asymmetry in fig. 6.14D. The peak for the Γ-velocity lies at the same position as the peak of the field strength, whereas the maximum of the total velocity is located prior to the field strength peak, as the transfer to upper valleys already sets in before this peak.

The average electron concentration (total and per valley) as a function of position is shown in fig. 6.15 for drain voltages of 0.5 and 2 V. Note that the peak in L-valley occupancy lies just behind the peak of the field strength. This represents the time it takes for the electrons to adjust to the field.

In fig. 6.15B clearly the increased occupancy of the upper valleys is seen for V_{DS} = 2 V, compared to fig. 6.15A (V_{DS} = 0.5 V).

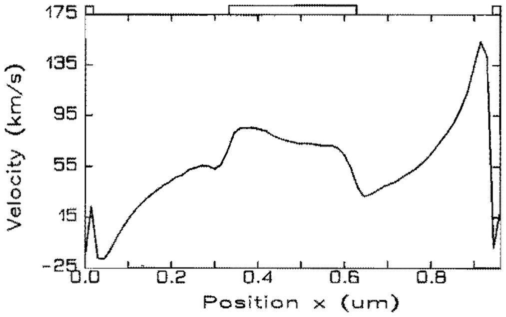

A

Fig. 6.14 *Average velocity in GaAs (—) for V_G = 0.2 V with (A) V_{DS} = 0.1 V, (B) V_{DS} = 0.25 V, (C) V_{DS} = 0.5 V and (D) V_{DS} = 2 V. In the figures the velocity for various valleys is indicated. (Continued on next page.)*

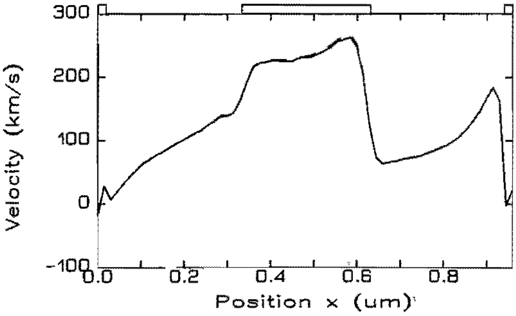

B

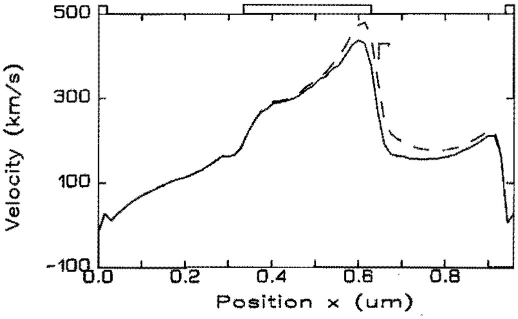

C

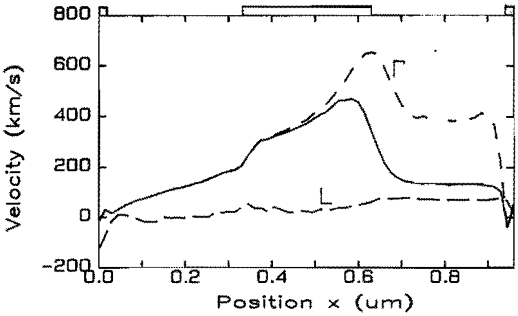

D

Fig. 6.14 *Average velocity in GaAs (—) for $V_G = 0.2$ V with (A) $V_{DS} = 0.1$ V, (B) $V_{DS} = 0.25$ V, (C) $V_{DS} = 0.5$ V and (D) $V_{DS} = 2$ V. In the figures the velocity for various valleys is indicated. (Continuation of previous page.)*

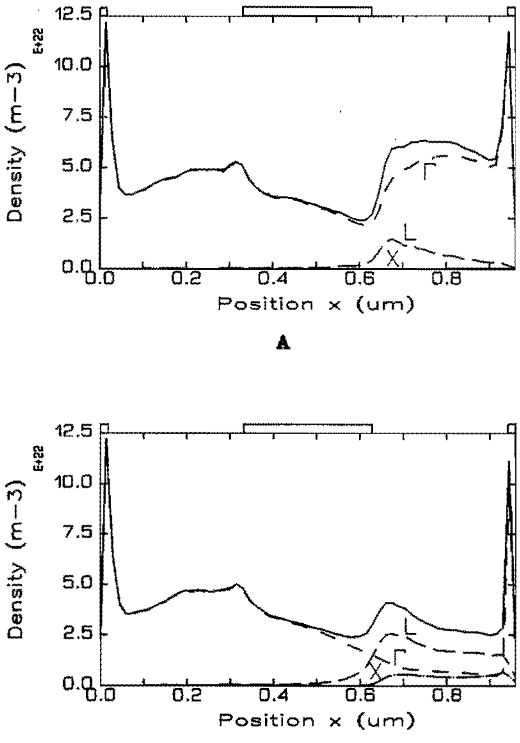

A

B

Fig. 6.15 *Average electron concentration in GaAs (—) for V_G =0.2* V, *with (A) V_{DS} = 0.5 V, and (B) V_{DS} = 2 V. In the figures the concentration for various valleys is indicated.*

Average energy

The average electron energy is shown in fig. 6.16 for drain voltages of 0.25, 0.5 and 2 V. In fig. 6.16C it can be clearly observed how the average energy of the electrons in the Γ-valley increases with the increasing field (fig. 6.10C) until an energy slightly higher than the Γ-L intervalley difference of 0.33 eV is reached. The subsequent decrease is caused by intervalley transfer and by the decrease of the field.

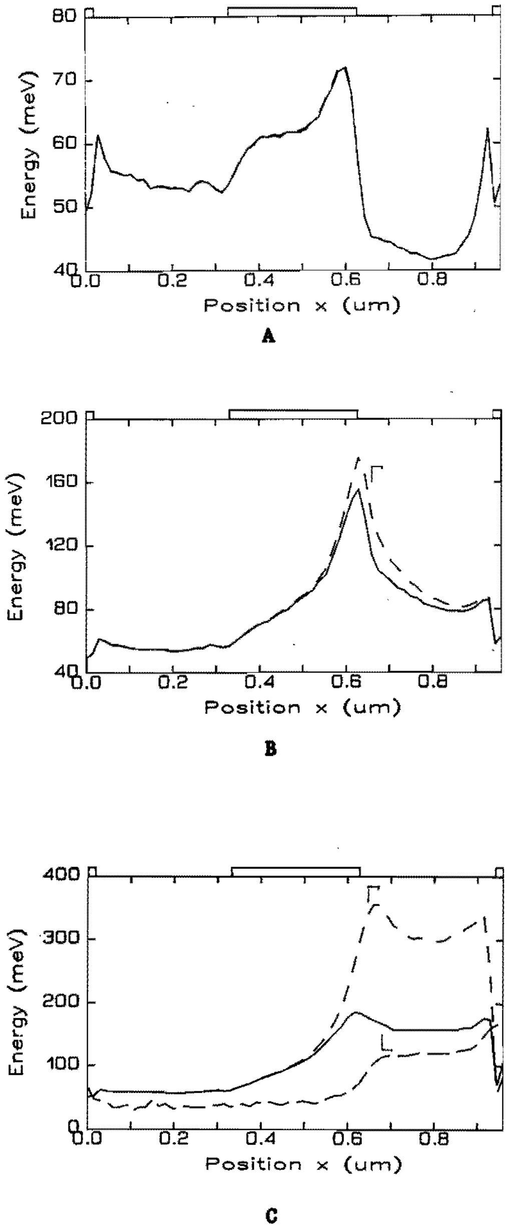

Fig. 6.16 *Average kinetic energy in GaAs (—) for V_G = 0.2 V, with (A) V_{DS} = 0.25 V, (B) V_{DS} = 0.5 V, and (C) V_{DS} = 2 V. In the figures the energy for various valleys is indicated.*

The large difference between total energy and Γ-valley energy in fig. 6.16C, behind the gate, is caused by the fact that at that point the main contribution to the average energy comes from the L-valley electrons. As the effective mass of an L-valley electron is much greater than that of a Γ-valley electron ($0.222 \cdot m_0$ against $0.063 \cdot m_0$) the kinetic energies that can be reached are much lower.

Real space transfer and boundary conditions at the contacts

With increasing energy the possibility of the occurrence of real space transfer becomes higher. As mentioned before the barriers for the Γ-, L- and X-valley are 0.227, 0.07 and -0.095 eV, respectively.

The question whether and where real space transfer occurs, and in which valleys, is an important one. Strongly correlated with this question is the matter of how exactly the current propagates, as will be clear from the following.

In fig. 6.17 the net currents (directed in the y-direction, perpendicular to the interface) caused by real space transfer are shown as a function of position for V_{DS} being equal to 0.25, 0.5, 1 and 2 V. Furthermore, in figs. 6.18–6.20 the net currents split up per valley are shown, for the three latter cases. Note that a positive current means that electrons transfer from GaAs to AlGaAs.

Real space transfer occurs in the first place, in a measure independent of drain voltage, between source and gate. There, a net transfer of electrons from AlGaAs to GaAs takes place (fig. 6.17). The first part of the current path propagates to a high degree through the AlGaAs, before the electrons become transferred to the GaAs. Note however, that the AlGaAs electrons not necessarily have to reach the vicinity of the gate first before they become

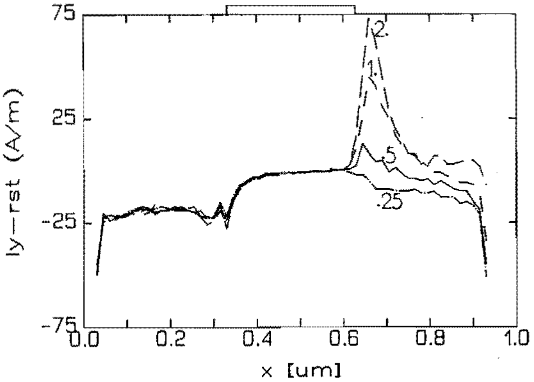

Fig. 6.17 *Real space transfer current as a function of position, for* V_G *= 0.2 V, with* V_{DS} *being equal to 0.25 , 0.5, 1 and 2 V.*

transferred, as the real space transfer current between source and gate is more or less independent of position.

Only at V_{DS} = 0.25 V a net transfer of electrons from AlGaAs to GaAs takes place behind the gate (fig. 6.17). This is a consequence of the boundary conditions at the drain, in combination with the low electric fields between gate and drain which do not prevent part of the electrons injected at the drain to travel quite a distance towards the gate. Near the gate, part of these electrons are pushed into the GaAs where they may travel towards the drain and get absorbed in the GaAs part of the drain. Naturally, the net contribution to the current is zero.

However, removal of the boundary condition for the electron concentration at the drain has yielded physically unrealistic results. As an alternative, simulations have been performed where absorption at one contact was followed by injection at the opposite one. With this boundary condition, sometimes unrealistic accumulations of electrons at the contacts were observed.

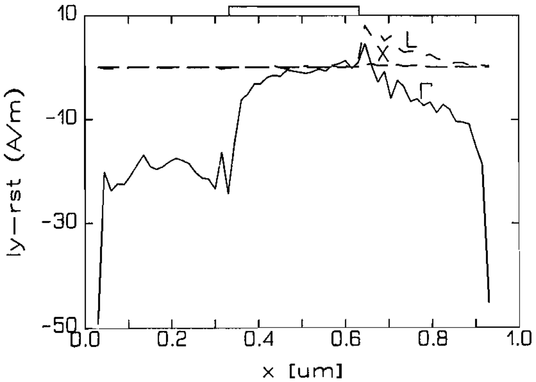

Fig. 6.18 ***Real space transfer current split up per valley, for V_G = 0.2 V and V_{DS} = 0.5 V.***

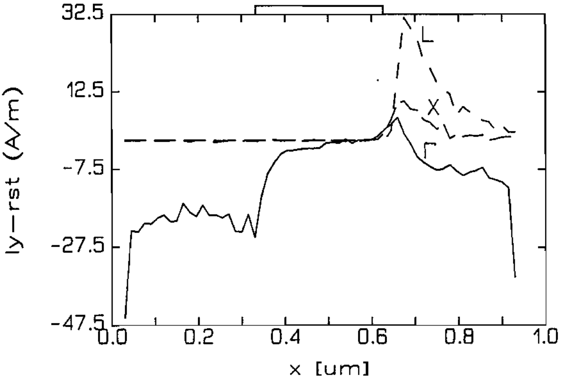

Fig. 6.19 ***Real space transfer current split up per valley, for V_G = 0.2 V and V_{DS} = 1 V.***

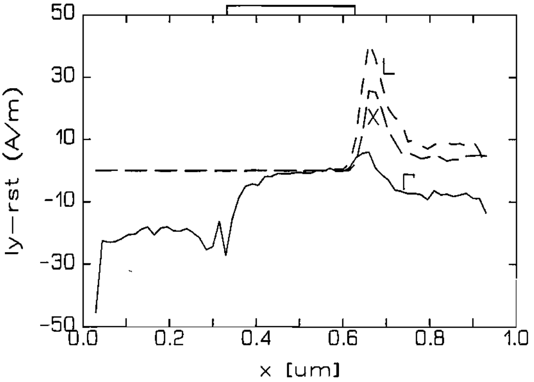

Fig. 6.20 ***Real space transfer current split up per valley, for V_G = 0.2 V and V_{DS} = 2 V.***

Furthermore, in this case there is no physical criterion to decide upon the position at which an electron should be injected. For these reasons, it is concluded that the present boundary condition for the electron concentration is physically the most realistic.

At the drain voltages above 0.25 V distinct peaks in the real space transfer current are seen at the drain edge of the gate (fig. 6.17), representing a net transfer from electrons from GaAs to AlGaAs. The values of these peaks increase with increasing drain voltage. As the drain voltage increases the electric field strength at the drain side of the gate increases and therewith the possibility of electrons obtaining sufficient energy to cross the energy barrier between GaAs and AlGaAs.

Figures 6.18–6.20 show the increasing importance of the contributions of the L- and X-valley electrons to the GaAs-to-AlGaAs transfer occurring behind the gate. In fact, but for a small area at the drain edge of the gate, the contribution of Γ-valley electrons remains negative (i.e from AlGaAs to GaAs). Note that the fact that the net contribution is negative does not mean that the process does not occur!

One should realize that this is not a severe phenomenon. For instance, after an electron has transferred from AlGaAs to GaAs it is very likely that intervalley transfer to the L-valley will occur, as the electron has recently acquired an extra energy of 0.227 eV. Being in the L-valley the possibility of transferring to AlGaAs again is higher than in the Γ-valley.

Furthermore, Γ-electrons in AlGaAs are more mobile and have a higher probability of reaching the interface than the electrons in the upper valleys. Once they reach the interface, real space transfer has a probability of 100 % (note that for X-electrons in AlGaAs in fact a potential barrier exists towards the GaAs).

As the mobility in the AlGaAs is lower than in GaAs the transfer from electrons from GaAs to AlGaAs has a decreasing effect on the performance of the device. However, as the transfer mainly occurs for electrons from the low-mobility valleys in GaAs to the low-mobility valleys in AlGaAs, the net effect is not that dramatic. Thus, the current saturation at high drain voltages is rather caused by velocity saturation in the GaAs than by real space transfer. A similar conclusion has been reached by Mouis et al. (1986).

Sheet densities at different gate voltages

With the gate voltage the charge in the channel can be controlled. In fig. 6.21 the sheet densities at different gate voltages and a fixed drain voltage of 2 V are shown. The sheet densities have been determined with Gauss's law.

Especially from fig. 6.21A it can be concluded that the control of the charge below the gate is rather weak, as the decline in charge is not very not very sharp. This will result in a low threshold voltage, as can be seen in the I_D–V_G characteristic of fig. 6.22.

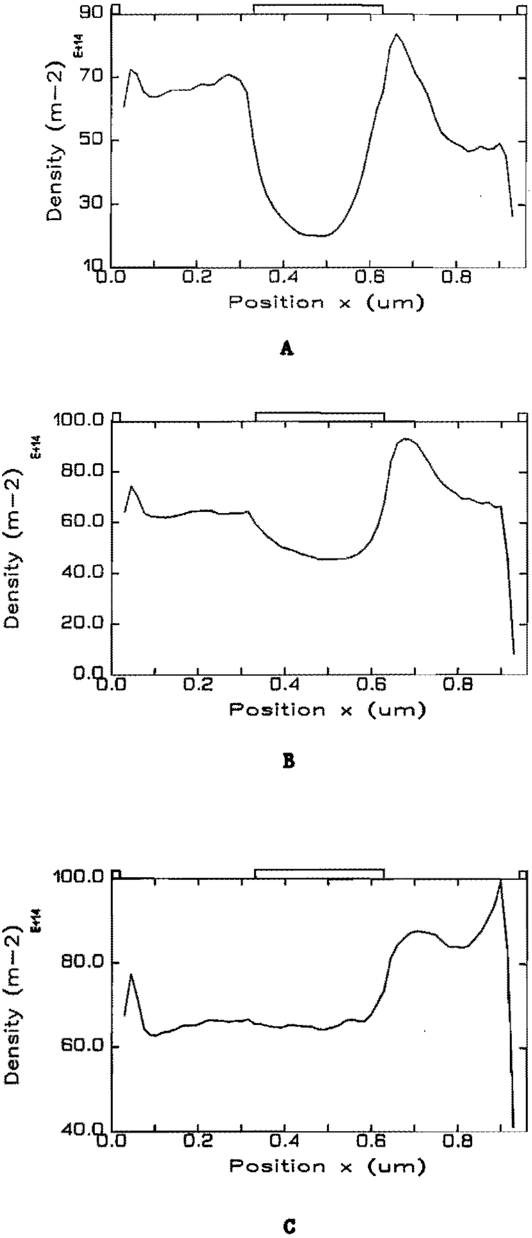

Fig. 6.21 *Sheet density in GaAs for $V_{DS} = 2$ V and (A) $V_G = -0.2$ V, (B) $V_G = 0.2$ V and (C) $V_G = 0.6$ V.*

6.5.3 Small-signal parameters

For the high-frequency behaviour of the device, the values of small-signal parameters are of interest. In the following the transconductance and cutoff frequency have been determined for an HEMT with the same geometry as used in the preceding sections. Later on, the gate length will be changed in order to investigate its effect on the small-signal parameters.

The transconductance g_m, the cutoff frequency f_T and the source-to-gate capacitance C_{GS} are defined according to (Sze 1981)

$$g_m = \left.\frac{\partial I_D}{\partial V_G}\right|_{V_{DS}}, \tag{6.37}$$

$$f_T = \frac{g_m}{2\pi C_{GS}}, \tag{6.38}$$

$$C_{GS} = \left.\frac{-\partial Q}{\partial V_G}\right|_{V_{DS}}. \tag{6.39}$$

In order to determine C_{GS} the change of the charge $-\partial Q$ is taken as the change in charge on the gate, which is determined using Gauss's law.

Results for a gate length of 0.3 μm

In order to determine the quantities mentioned above, simulations have been done at $V_{DS} = 2$ V. The gate voltage has been varied between -0.6 and 0.8 V (with steps of 0.1 V). In fig. 6.22 the resulting curve of I_{DS} as a function of V_G is shown. The derivative yields the transconductance. Note that the geometry of the HEMT is the one shown in fig. 6.6.

In figs. 6.23–6.25 the resulting small-signal parameters are shown. Both the transconductance and the cutoff frequency reach their maximum values around gate voltage 0 V. At higher gate voltages the contribution of the current through the AlGaAs in the area between gate and drain becomes considerable and g_m decreases. The decreasing transconductance together with the increasing capacitance cause the decrease in the cutoff frequency.

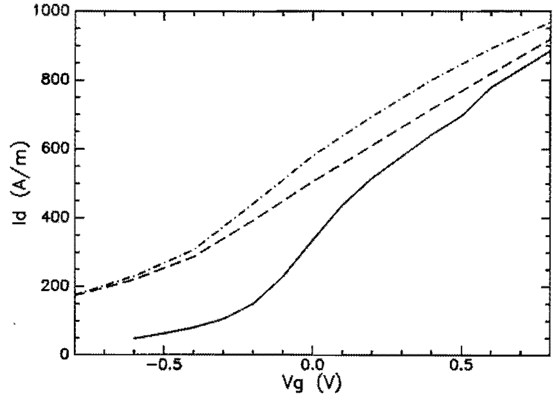

Fig. 6.22 *I_D versus V_G characteristic in the saturation regime (V_{DS} = 2 V), for gate lengths of (—) 0.3 μm, (- -) 0.11 μm (case I), and (-··-) 0.105 μm (case II).*

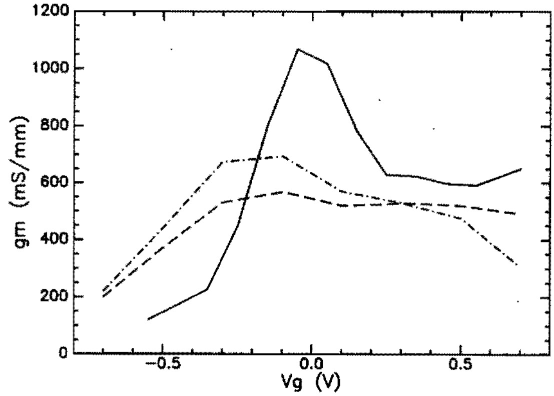

Fig. 6.23 *Transconductance g_m as a function of gate voltage V_G, for gate lengths of (—) 0.3 μm, (– –) 0.11 μm (case I), and (-··-) 0.105 μm (case II).*

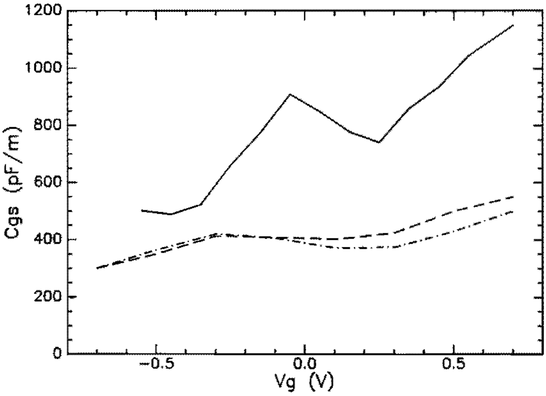

Fig. 6.24 *Gate-to-source capacitance C_{GS} as a function of gate voltage V_G, for gate lengths of (—) 0.3 µm, (– –) 0.11 µm (case I), and 0.105 µm (-··-) (case II).*

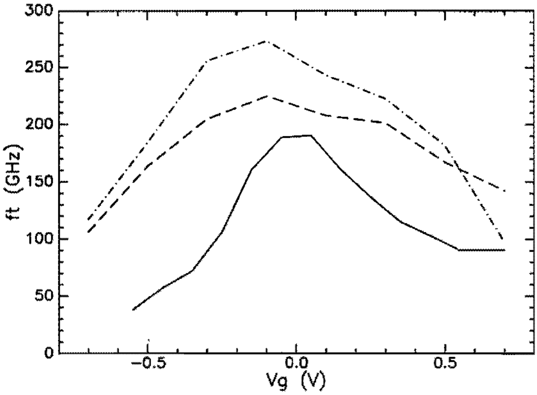

Fig. 6.25 *Cutoff frequency f_T as a function of gate voltage V_G, for gate lengths of (—) 0.3 µm, (– –) 0.11 µm, and (-··-) 0.105 µm.*

Results for a gate length of 0.1 µm

The influence of the gate length and interelectrode spacings on the high-frequency performance of the HEMT will now be investigated. Therefore, two slightly different dimensions will be chosen.

Given the restrictions posed by the mesh it is tried to obtain two devices with gate lengths as close to 0.1 µm as possible. The first device will be chosen to have interelectrode spacings as close as possible to those of the device treated above. The second device should have the same total length as the HEMT treated above. The resulting device dimensions are mentioned in the following.

First, an HEMT with a gate length of 0.11 μm and interelectrode spacings of 0.286 μm is simulated. The interelectrode spacings have been chosen such as to be as much as possible in accordance with the ones in the previous case (0.315 μm), given the mesh sizes. The length of the mesh cell now is 0.011 μm. This case will be referred to as case I.

Next, an HEMT with a gate length of 0.105 μm and interelectrode spacings such that the total length of the device is again 0.96 μm. This results in a source-to-gate distance of 0.405 μm and a gate-to-drain distance of 0.42 μm, with the mesh cell length again being 0.015 μm. This case will be denoted as case II.

All other geometrical, physical and model parameters remain unchanged in both cases. At the same time, all requirements concerning stability are fulfilled again.

The results are shown in fig. 6.22, and the resulting small-signal in figs. 6.23–6.25.

The highest frequencies are reached in the second case (fig. 6.25). This is especially caused by higher transconductance values (fig. 6.23), as the capacitances in case I and II do not differ very much (fig. 6.24). The latter has to be expected, as the capacitance mainly depends on the gate length. The fact that the frequencies are higher than with gate length 0.3 μm is mainly caused by the fact that at smaller gate lengths the capacitances are lower. The transconductance on the average has not been changed very much, except the high peaks around 0 V have been disappeared (fig. 6.23).

This indicates a less effective control of gate on the charge in the channel.

A striking feature is that the gate threshold voltage seems to be much smaller (fig. 6.22) for a gate length of 0.1 μm than for 0.3 μm. Again, as a consequence of the decrease of the gate length, in the devices studied in cases I and II, a reduced charge control shows. This can also be observed in fig. 6.26, which shows the sheet density for gate voltages of -0.4, -0.2 and 0.2 V.

Kizilyalli et al. (1986) have predicted from a two-dimensional analytical model of the HEMT based on a three moments solution of the Boltzmann equation, that at gate lengths smaller than 0.15 μm the transconductance would not increase anymore with decreasing device dimensions. The results obtained in case I and II seem to confirm this prediction.

Another way of determining the cutoff frequency would be to determine it from the transit time t_T, which is defined as (Lindmayer and Wrigley 1965)

$$t_T = \int \frac{1}{v(x)}\, dx. \tag{6.40}$$

The cutoff frequency is then calculated as (Lindmayer and Wrigley 1965)

$$f_T = \frac{1}{2\pi t_T}. \tag{6.41}$$

The difficulty here is the choice of the integration path, which has been found to have great influence on the final result. When only the channel, in GaAs below the gate, is considered values comparable to those found earlier are obtained only for the lowest gate voltages. This indicates that the current propagating through the AlGaAs should be taken into account in some way.

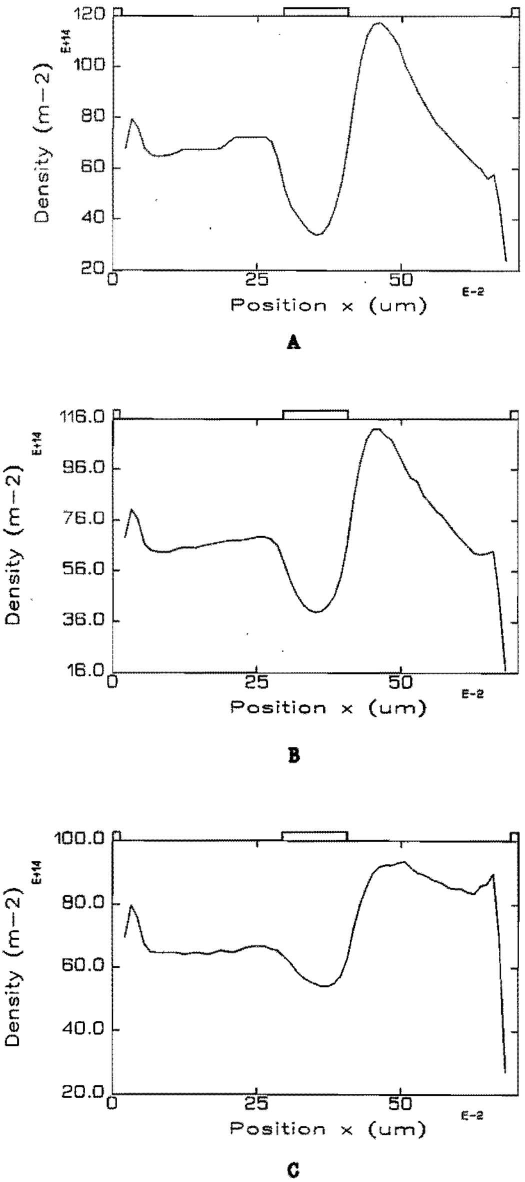

Fig. 6.26 *Sheet density in GaAs for case I, with* $V_{DS} = 2$ *V and (A)* $V_G = -0.4$ *V, (B)* $V_G = -0.2$ *V and (C)* $V_G = 0.2$ *V.*

An attempt to determine the cutoff frequency in this manner has been made on the results obtained in case I.

A different path has been selected for each gate voltage. This path is selected 'by hand', judging the sheet density in GaAs. The path begins where the sheet density starts decreasing, which point will be in the vicinity of the beginning of the gate. The path ends behind the gate, at the point where the sheet density has passed its peak value and more or less has reached its end value. A <v(x)> is determined as the average over the y-coordinate, as

$$\langle v(x)\rangle = \int v(x,y)dy \ / \int dy, \tag{6.42}$$

where the integration over y is taken over the complete height of the device (i.e. both the GaAs and AlGaAs layer). Only in this way it appears that the results for f_T are at least qualitatively resembling those obtained with eq.(6.38). See fig. 6.27.

An alternative for eq.(6.41) has been suggested by Van de Roer (1989) as

$$f_T = \frac{0.35}{t_T}. \tag{6.43}$$

This formula is frequently used in microwave calculations (Javid and Brenner 1963). Transit frequencies obtained with this formula are also shown in fig. 6.27. Using eq.(6.43), the results are quantitatively in much better accordance. However, the choice of a suitable integration path remains a problem.

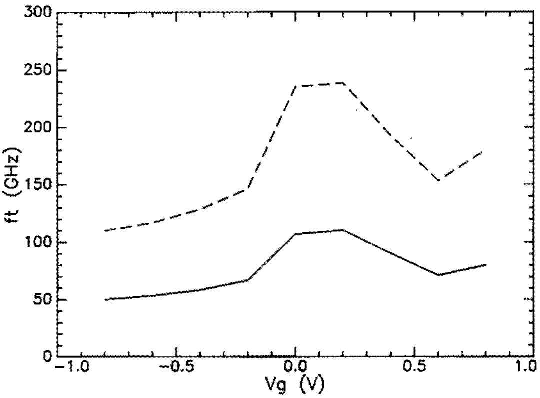

Fig. 6.27 *Cutoff frequency f_T as determined from the transit time, (—) using eq.(6.41) and (– –) using eq.(6.43).*

6.6 Conclusions

The HEMT with a gate length 0.3 μm which has been discussed in the previous section has the same dimensions as the one simulated with the Ensemble Monte Carlo method by Thobel (1988). The results found in this work are qualitatively in accordance with those by Thobel. However, the currents obtained here are higher. As a consequence the transconductances are higher, as well as the maximum cutoff frequency (± 190 GHz against 110 GHz). Such a difference cannot easily be understood.

Experimental results on HEMTs with a gate lenght of 0.25 μm (which is close to 0.3 μm) yield a maximum cutoff frequency of about 80 GHz (Chao et al. 1985). For an HEMT with gate length of 0.1 μm a maximum cutoff frequency of 113 GHz has been obtained (Lepore et al. 1988). The difference with the values found in this work is quite large, and therefore the results obtained here cannot be regarded as final.

It has been pointed out that at high drain voltages the most important contribution to real space transfer from GaAs to AlGaAs behind the gate comes from electrons in the L- and X-valleys. Therefore, it can be concluded that the current saturation is especially caused by intervalley transfer in GaAs.

A decrease of the gate length to about 0.1 μm causes an increase in the maximum cutoff frequency, which is mainly caused by a decrease in source-to-gate capacitance. The interelectrode spacings here have been found of minor influence, although the cutoff frequencies are somewhat higher with the higher electrode spacings.

An alternative method to determine the cutoff frequency from the transit time poses a problem, since an integration path has to be determined which accounts for the current path. For each case this path has to be determined again, whereas it is not clearly defined. Furthermore, the exact choice of the path has a large influence on the final result.

Chapter 7

QUANTUM WELL TRANSFER

In this chapter[1] a mechanism is presented, called quantum well transfer, intended for use in Monte Carlo transport calculations in which 2D as well as 3D electronic states are present. This transfer process provides a means for a phonon-assisted coupling between confined two-dimensional states in a GaAs/AlGaAs heterojunction quantum well and the 3D Bloch states existing in the bulk material. The case of polar-optical phonon-assisted 'quantum well escape' is elaborated.

7.1 Introduction

With the advent of modulation doping in MBE, it has become possible to grow accurately doped and sharply defined GaAs/AlGaAs single or multiple heterolayers. In the High Electron Mobility Transistor (HEMT), see chapter 6, using a GaAs/AlGaAs heterojunction conducting channel, higher mobilities are achieved than in bulk GaAs (Dingle et al. 1978), owing to the fact that the conduction electrons in GaAs are spatially separated from their parent donors in AlGaAs.

In chapters 5 and 6, where the transport properties of an

---

[1] Work performed at the Universite des Sciences et Techniques de Lille-Flandres-Artois while on leave of absence from the University of Technology Eindhoven. The material in this chapter has been published by Nederveen and Zimmermann (1989).

AlGaAs/GaAs heterojunction, respectively, the HEMT have been studied, the special nature of the electrons in the quasi-two-dimensional electron gas (Q2DEG) at the GaAs/AlGaAs heterointerface has been neglected and the 'classical' 3D scatter rates have been used (chapter 3). In reality, the carriers at the interface may be confined in a quantum well, their motion in the direction perpendicular to the interface being forbidden because of quantization. Consequently, the electrons are distributed in energy subbands, a situation which resembles much that encountered in silicon inversion layers (Ando et al. 1982).

The scatter rates for the electrons in subbands are different from the ones given in chapter 3, because the form of the wave function has been changed. Furthermore, additional effects such as inter- and intrasubband scattering should be taken into account.

If one decides to take subbands into account, the necessity of which is depending upon the physical circumstances under which the device is to be studied, one needs a mechanism to account for the transfer of electrons from a confined 2D state to a 3D state, and vice versa. For the description of any electron escape (capture) mechanism from (in) the well, a mechanism has to be formulated that must be accompanied by one of the usual scatter processes (acoustic or polar optical phonon scattering, piezoelectric, intervalley or ionized impurity scattering).

The purpose of this chapter is to arrive at general formulas analogous to those obtained for electron—phonon interaction in a quantum well (Price 1981). In order to show the applicability to Monte Carlo simulations the case of polar-optical phonon-assisted quantum well escape (QWE) will be elaborated. It should be stressed that, to the best of the knowledge of the author of this work, no earlier attempt has been reported to analyse this problem in detail. Ravaioli (1986) has derived scatter rates only for 2D to 3D transitions, with the constraint that at the same time real space transfer occurs, using the variational wave functions of Fang and Howard (Ando et al. 1982). Yokoyama and Hess (1986) seem to have treated the problem only numerically, and Zimmermann and Wu Yen (1987) have adopted a pragmatic approach, where 2D–3D transitions only take place via intervalley scattering and the rates are a modification of the 3D rates for intervalley scattering.

Nevertheless, the interest is clear, because once in a 3D state an electron may exhibit real space transfer from GaAs to AlGaAs, or intervalley transfer. This will make the formalism to be described in the following especially useful for Monte Carlo purposes.

7.2 Electron–phonon interaction in a quantum well

The electron state $|\vec{K},n\rangle$ in a quantum well is characterized by a subband index n and a 2D wave vector $\vec{K}$ parallel to the heterointerface. Its wave function and energy are, respectively,

$$\psi_{\vec{K},n}(\vec{R},z) = A^{-1/2}\phi_n(z)\exp(i\vec{K}\cdot\vec{R}), \tag{7.1}$$

and

$$W_n(\vec{K}) = W_n + \frac{\hbar^2K^2}{2m^*}, \tag{7.2}$$

where $\phi_n(z)$ denotes the quantized normalized wave function in the direction z perpendicular to the interface, $\vec{R}$ is the vector along the interface, m^* the electron effective mass, ħ Planck's constant divided by 2π, and A the heterointerface surface.

The matrix element $M_{2D}(\vec{Q})$ used for the calculation, in first-order perturbation theory, of the transition rate $S(\vec{K},n;\vec{K}',m)$ for an electron in state $|\vec{K},n\rangle$ to $|\vec{K}',m\rangle$ is linked to the matrix element for the three-dimensional case $M_{3D}(\vec{Q},q_z)$ via (Price 1981)

$$|M_{2D}(\vec{Q})|^2 = \frac{V}{2\pi A}\int dq_z\ |M_{3D}(\vec{Q},q_z)|^2|I_{mn}(q_z)|^2, \tag{7.3}$$

where $\vec{Q}$ is the parallel and q_z the transverse wave vector component of the phonon involved, V is the effective volume of the well, and

$$I_{mn}(q_z) = \int dz\ \phi_m(z)\phi_n(z)\ \exp(iq_z z). \tag{7.4}$$

The transition rate is given by Fermi's Golden Rule

$$S(\vec{K},n;\vec{K}',m) = \frac{2\pi}{\hbar}\ |M_{2D}(\vec{Q})|^2\ \Delta(1,2), \tag{7.5}$$

where $\Delta(1,2)$ is a delta-function taking care of conservation of energy. The scatter rate $\lambda(\vec{K})$ now is arrived at by integrating over all possible final states $\vec{K}'$

$$\lambda(\vec{K}) = \frac{A}{4\pi^2}\iint d\vec{K}'\ S(\vec{K},n;\vec{K}',m). \tag{7.6}$$

7.3 Quantum well transfer

In this section expressions for the probability of an electron transferring from a 2D to a 3D state (vice versa) under exchange of a phonon, will be derived. In general, this process will be denoted by 'quantum well transfer', and will be distinguished into quantum well escape (QWE) and quantum well capture (QWC). It is to be understood that QWE should be added to the scatter processes in the

Q2DEG for which the calculation of the rates has been treated in section 7.2. Likewise, QWC is a process additional to the processes for 3D electrons which have been discussed in chapter 3.

As in the derivation of eq.(7.3), the same interaction Hamiltonian, $\mathcal{H}'$, will be assumed to be valid for the quantum well as well as for the bulk phonons. In deriving the following expressions it has been assumed that $\mathcal{H}'$ may be expanded into a sum over phonon states $\vec{q} = \vec{Q} + \vec{q}_z$, as in eq.(3.14)

$$\mathcal{H}' = \sum_{\vec{q}} A(\vec{q})[a_{\vec{q}}\exp(i\vec{q}\cdot\vec{r}) + a^{\dagger}_{\vec{q}}\exp(-i\vec{q}\cdot\vec{r})], \tag{7.7}$$

where $A(\vec{q})$ is related to the amplitude of the lattice vibration represented by phonon wave vector $\vec{q}$, and $a_{\vec{q}}$ and $a^{\dagger}_{\vec{q}}$ are the annihilation and creation operators, respectively (Nag 1980).

7.3.1 Quantum well escape

The matrix element $M_{23}(\vec{Q},q_z)$ for a 2D to a 3D state transition, where the number of phonon states changes from $n_{\vec{q}}$ to $n_{\vec{q}} \pm 1$ (upper sign denotes emission and lower sign absorption of a phonon by the electron, throughout this section) may be written as

$$M_{23}(\vec{Q},q_z) = \langle\vec{k}', n_{\vec{q}} \pm 1|\mathcal{H}'|n_{\vec{q}}, n, \vec{K}\rangle. \tag{7.8}$$

where $|\vec{K},n\rangle$ is characterized by the wave function eq.(7.1), and $|\vec{k}'\rangle$ by the wave function $\Psi_{\vec{k}'}(\vec{r}) = V^{-1/2}\exp(i\vec{k}'\cdot\vec{r})$ with the 3D wave vector $\vec{k}' = (\vec{K}', k_z')$ at position $\vec{r} = (\vec{R},z)$. The derivation is straightforward, see e.g. eqs.(3.15)–(3.18), and leads to a point where

$$M_{23}(\vec{Q},q_z) = \sum_{\vec{q}} A(\vec{q}) \sqrt{n_{\vec{q}} + \tfrac{1}{2} \pm \tfrac{1}{2}} \int dz \; \phi_n(z)\exp(-ik'_z z)\exp(iq_z z) \;\; \delta_{\vec{Q},\vec{K}' \mp \vec{K}}$$

$$= M_{3D}(\vec{Q},q_z) \; I_{23}(q_z,k'_z), \qquad (7.9)$$

with

$$I_{23}(q_z,k'_z) = L_T^{-1/2} \int dz \; \phi_n(z)\exp(-ik'_z z)\exp(iq_z z). \qquad (7.10)$$

One should realize here that just 'above' the quantum well the representation of the 3D electron state by means of a plane wave will not be really very accurate. For reasons of simplicity this representation has been adopted, with the constraint that the plane wave normalization volume V_T should contain that space in which (most of) the 2D electrons reside, i.e. $V_T = A\, L_T$. L_T will be taken as the width of the well at the energy level W_T, with W_T being described below.

The energy level W_T serves as a threshold. Two-dimensional electrons having total energy beyond this level may become three-dimensional. Inversely, three-dimensional electrons with energy below this level have the possibility to become two-dimensional.

Suppose one looks for the minimum energy level for a QWE process under absorption of a phonon $\hbar\omega_0$. The total energy of a two-dimensional electron, being equal to $W_m + W_{\|}$, should be greater than $W_T - \hbar\omega_0$ for this QWE process to be possible. Inversely, if the total energy of a three-dimensional electron is smaller than $W_T + \hbar\omega_0$, QWC accompanied by emission of a phonon is possible.

For the determination of the value of W_T two criteria are possible. To begin with, it could be defined as the level where the subband energy levels have become that close to each other that the energy spectrum could be regarded a continuum. Another possiblitity could be to choose that energy level at which the width of the well is an order of magnitude larger than the average DeBroglie wavelength of the electrons at that level. The two criteria are expected to yield simliar values of W_T. Depending on the problem under consideration the one or the other should be chosen. See also fig. 7.1.

Drawing a simple vector diagram, (see fig. 7.2,) one is inclined to conclude that k'_z should equal q_z. However, this assumption ignores the (principally unknown) value of the wave vector component k_z in the quantum well. As an equivalent to the square well one may argue that $k_z = \pm(2m^*W_m)^{1/2}/\hbar = \pm\alpha$. With $k'_z = k_z + q_z$, $I_{23}(q_z,k'_z)$ now in fact has become a function of k_z, so $I_{23}(q_z,k'_z) = I_{23}(k_z)$, and

$$I_{23}(k_z) = L_T^{-1/2}\int dz\ \phi_m(z)\ \exp(-ik_z z)\ . \qquad (7.11)$$

Note here that $|I_{23}(k_z)|^2$ is independent of the sign of k_z, so $|I_{23}(+\alpha)|^2 = |I_{23}(-\alpha)|^2$.

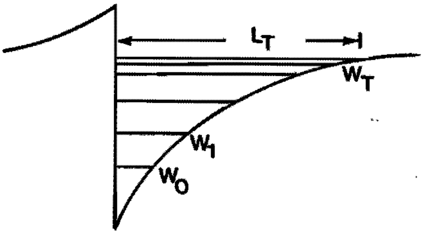

Fig. 7.1 *The conduction band near the heterointerface with (schematically denoted) a set of approaching subbands, the threshold energy level W_T (the upper energy level in the well) and the normalization width L_T.*

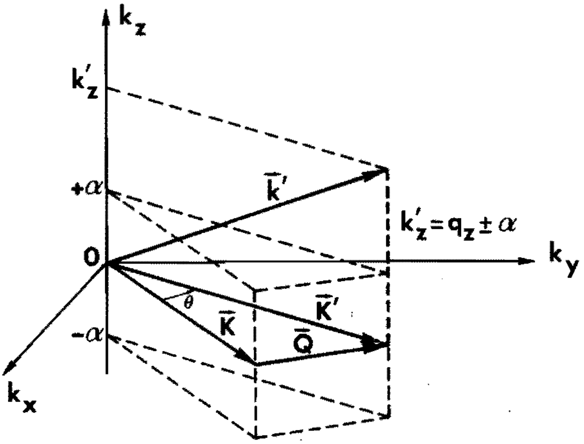

Fig. 7.2 *Vector diagram for the transition from a 2D-electron state (with wave vector $\vec{k}$) to a 3D state (wave vector $\vec{k}'$). The uncertainty for k_z is represented by α.*

In order to proceed from $|M_{23}(\vec{Q},q_z)|^2$ to $|M_{23}(\vec{Q})|^2$ one merely sums over the two possible q_z values, which in essence is a summation over the probabilities $|M_{23}(\vec{Q},q_z)|^2$ weighted with $|I_{23}(\alpha)|^2$. This is analogous to the the calcualtion for the squared matrix element of eq.(7.3), see Vinter (1985). The squared matrix element for the QWE becomes

$$|M_{23}(\vec{Q})|^2 = |I_{23}(\alpha)|^2 \sum_{q_z = k'_z \pm \alpha} |M_{23}(\vec{Q},q_z)|^2 \, , \tag{7.12}$$

so that the scatter rate may be written as

$$\lambda_{23}(\vec{K}) = \frac{2\pi}{\hbar} \frac{V}{8\pi^3} |I_{23}(\alpha)|^2 \sum_{q_z = k'_z \pm \alpha} \iiint d\vec{k}' \; |M_{23}(\vec{Q},q_z)|^2 \Delta(1,2) . \tag{7.13}$$

7.3.2 Quantum well capture

In a way analogous to the former subsection the matrix element $M_{23}(\vec{Q},q_z)$ for the QWC from state $|\vec{k}\rangle$ to $|\vec{K}',n\rangle$ becomes

$$M_{32}(\vec{Q},q_z) = M_{3D}(\vec{Q},q_z)\; I_{32}(q_z,k_z), \tag{7.14}$$

with

$$I_{32}(q_z,k_z) = L_T^{-1/2}\int dz\; \phi_n(z)\exp(ik_z z)\exp(iq_z z). \tag{7.15}$$

The same line of reasoning as before will be followed, with $k_z + q_z = k'_z$ and $k'_z = \pm\alpha$ yielding $q_z = \pm\alpha - k_z$, which leads to a scatter rate

$$\lambda_{32}(\vec{k}) = \frac{2\pi}{\hbar}\,\frac{A}{4\pi^2}\,|I_{32}(\alpha)|^2 \sum_{q_z=\pm\alpha-k_z} \iint d\vec{K}'\; |M_{32}(\vec{Q},q_z)|^2\Delta(1,2). \tag{7.16}$$

7.4 Application to Monte Carlo simulations

The application to Monte Carlo simulations of quantum well transfer is reasonably straightforward. One should be aware of the fact that it will be conceptually wrong to use a sinusoidal wave-function $\phi_m(z)$ stemming from a rectangular well with infinitely high barriers, because the existence of electron states outside the well is denied by this assumption. The variational wave-functions of Fang and Howard (Ando et al. 1982) are better in this respect, although they are zero at the interface $z = 0$, thus forbidding the electrons to penetrate the AlGaAs layer. Of course, one just calculates the rates one requires with any $\phi_m(z)$ available, while the delta function $\Delta(1,2)$ provides the transfer conditions.

Quantum well capture is only likely to occur for an electron residing 'above' the well, a criterion which of course depends heavily upon the form of the well. In order to show the problems to be encountered the case of polar-optical phonon-assisted QWE will be elaborated a little further, because polar-optical phonon scattering is the most important process limiting the electron mobility in the quantum well.

Under the neglect of the overlap function $G(\vec{k},\vec{k}')$ the squared three-dimensional matrix element for polar-optical phonon scattering is, from eq.(3.33)

$$|M_{3D}(\vec{q})|^2 = \frac{e^2\hbar\omega_0}{2V\epsilon_0 q^2}\left(\frac{1}{\epsilon_\infty} - \frac{1}{\epsilon_s}\right)(n_{\vec{q}} + \tfrac{1}{2} \pm \tfrac{1}{2}), \tag{7.17}$$

where ϵ_∞ and ϵ_s are the high and low frequency relative permittivities, respectively, $\hbar\omega_0$ is the longitudinal optical phonon energy, $n_{\vec{q}}$ is the phonon occupation number (with the minus sign for absorption and the plus sign for emission of a phonon).

All that is needed now to be able to evaluate $\lambda_{23}(\vec{K})$ is the deltafunction $\Delta(1,2)$, describing conservation of energy. For parabolic energy bands this leads to $\frac{\hbar^2k'^2}{2m^*} = W_m + \frac{\hbar^2K^2}{2m^*} \pm \hbar\omega_0$, which first of all should be greater than or equal to the W_T as defined above. $\Delta(1,2)$ becomes

$$\Delta(1,2) = \delta(W' - \Delta W - W_{\parallel}), \tag{7.18}$$

with

$$\Delta W = W_m \pm \hbar\omega_0 \tag{7.19}$$

and

$$W_{\parallel} = \frac{\hbar^2K^2}{2m^*}, \tag{7.20}$$

where W' is the kinetic energy after scattering, and $W_{\parallel}$ the kinetic energy parallel to the interface before scattering, and where the plus sign now denotes absorption and the minus sign emission of a phonon.

In order to take into account the symmetry of the problem the integration in eq.(7.13) is taken in cylindrical coordinates, and the integration variable is changed from $\vec{k}'$ to W'. Then one obtains

$$\lambda_{23}(W_{\parallel}) = C \sum \iiint \frac{dW'_{\parallel}\, dW'_{\perp}\, d\vartheta}{(Q^2 + q_z^2) {W'_{\perp}}^{1/2}} \Delta(1,2), \tag{7.21}$$

where ϑ is the angle between $\vec{K}$ and $\vec{K}'$ and

$$C = \frac{e^2 \omega_0 m^{*2}}{8\pi^2 \epsilon_0 \hbar^3 (2m^*)^{1/2}} \left(\frac{1}{\epsilon_\infty} - \frac{1}{\epsilon_s}\right) (n_{\vec{q}} + \tfrac{1}{2} \pm \tfrac{1}{2}) \; |I_{23}(\alpha)|^2. \tag{7.22}$$

The integral is first taken over $W'_{\parallel}$ and then over ϑ, which yields

$$\lambda_{23}(W_{\parallel}) =$$

$$\frac{\pi\hbar^2}{m^*} C \sum \int_0^{W_{\parallel}+\Delta W} dW'_{\perp} \frac{1}{{W'_{\perp}}^{1/2} [(2W_{\parallel} + \Delta W + \beta^2 \pm 2\beta\sqrt{W'_{\perp}})^2 - 4W_{\parallel}(W_{\parallel} + \Delta W - W'_{\perp})]^{1/2}} . \tag{7.23}$$

This results in

$$\lambda_{23}(W_{\parallel}) = G\, c^{-1/2} \ln\left\{[F_+ + (1 + F_+^2)^{1/2}]\; [F_- + (1 + F_-^2)^{1/2}]\right\}. \tag{7.24}$$

with

$$F_{\pm} = \Big\{[2c(W_{\parallel} + \Delta W)^{1/2} \pm b](d + b)^2)^{1/2} \mp$$

$$b[d + [2c(W_{\parallel} + \Delta W)^{1/2} \pm b]^2]^{1/2}\Big\}/d, \tag{7.25}$$

and

$$b = 4\beta(2W_{\parallel} + \Delta W + \beta^2) \tag{7.26}$$

$$c = 4(\beta^2 + W_{\parallel}) \tag{7.27}$$

$$d = 16W_{\parallel}(\Delta W - \beta^2)^2 \tag{7.28}$$

$$\beta = \hbar\alpha(2m^*)^{-1/2} = W_m/\sqrt{2} \tag{7.29}$$

$$G = \frac{m^{*1/2}|I_{23}(\alpha)|^2 e^2\hbar\omega_0}{4\sqrt{2}\hbar^2\epsilon_0}\left(\frac{1}{\epsilon_\infty} - \frac{1}{\epsilon_s}\right)\left(n_{\vec{q}} + \frac{1}{2} \pm \frac{1}{2}\right). \tag{7.30}$$

After the process has been selected the new state must be determined. First of all the scatter angle ϑ between $\vec{K}$ and $\vec{K}'$ has to be determined. Either $W'_{\perp}$ or $W'_{\parallel}$ is to be selected with the help of a random number, from which the moduli K' and k'_z are calculated. The orientation of k'_z (up or down) is randomly determined.

It should be pointed out out here that in principle it is possible to use a 'double' rejection technique, i.e. in evaluating $\lambda_{23}(W_{\parallel})$ one first evaluates the integral over one of the energy components, say $W'_{\parallel}$, leaving a function $H(W'_{\perp},\vartheta)$. The strategy then is to draw a pair of random numbers $(\tilde{W}'_{\perp},\tilde{\vartheta})$ in the ranges $[0,W_{\parallel} + \Delta W)$ and $[0,2\pi)$, respectively, then calculate $H(\tilde{W}'_{\perp},\tilde{\vartheta})$, draw a new random number $\tilde{H}$ between 0 and H_{max} and retain the values $\tilde{W}'_{\perp}$ and $\tilde{\vartheta}$ if $\tilde{H} \leq H(\tilde{W}'_{\perp},\tilde{\vartheta})$, otherwise restart the procedure. Of course, this method may lead to serious computational effort.

Alternatively, although the algebra required to arrive at a formula giving the relation between a random number and $W'_{\perp}$ is rather tedious, the value of $W'_{\perp}$ may be drawn with the direct method as in eqs.(2.16) or (2.17). For this purpose formula (7.23) is used, normalized with the total scatter rate and integrated from 0 to the energy value randomly to be selected, analogous to eq.(2.16).

An expression for the angle ϑ as a function of a random number is arrived at by changing the integration order, starting with $W'_{\parallel}$, yielding

$$\lambda_{23}(W_{\parallel}) = \frac{C\hbar^2}{2m^*}\sum \int_0^{\vartheta'}\int_0^{W_{\parallel}+\Delta W} d\vartheta dW'_{\perp}$$

$$\frac{2W_{\parallel}+\Delta W+\beta^2 \pm 2\beta\sqrt{W'_{\perp}} + 2\cos\vartheta[(W_{\parallel}+\Delta W-W'_{\perp})]^{1/2}}{{W'_{\perp}}^{1/2}[(2W_{\parallel}+\Delta W+\beta^2 \pm 2\beta\sqrt{W'_{\perp}})^2 - 4\cos^2\vartheta\, W_{\parallel}(W_{\parallel}+\Delta W-W'_{\perp})]} . \qquad (7.31)$$

The part of the integrand with the $\cos\vartheta$ term in the numerator makes the integral over $W'_{\perp}$ non-solvable. However, if one approximates $(W_{\parallel} + \Delta W - W'_{\perp})^{1/2}$ by a three term Taylor expansion the integration over $W'_{\perp}$ can be performed . This approximation is not expected to lead to serious errors; a first-order calculation shows that the maximum error to be expected is 10% in the less prominent part of the scatter angle distribution function.

The resultant integral over ϑ cannot be solved. Hence ϑ has to be determined with the rejection technique.

7.5 Conclusion

It has been shown that it is possible to introduce into a Monte Carlo model, describing out-of-equilibrium transport in a heterojunction quantum well, a mechanism which takes into account the coupling between confined 2D states in the well and 3D Bloch states in the bulk, using Fermi's Golden Rule.

Here a so-called Quantum Well Escape process involving polar-optical phonons is elaborated. However, in the described formalism, in principle every known, elastic as well as inelastic, scatter process may be involved. The developed Quantum Well Transfer mechanism is straightforward and could easily be implemented.

REFERENCES

Adachi, S., 1985, J. Appl. Phys. **58**, R1–R29.

Ando, T., A. B. Fowler and F. Stern, 1982, Rev. Mod. Phys. **54**, 437–672.

Awano, Y., K. Tomizawa, N. Hashizume and M. Kawashina, 1983, El. Lett. **19**, 20–21.

Awano, Y., K. Tomizawa, N. Hashizume, 1984, IEEE Trans. El. Dev. **31**, 448–452.

Balemans, H. C. H., 1988, Master's Thesis, no. E/EEA/376/2/88, University of Technology Eindhoven.

Beard, S. J. and R. W. Hockney, 1985, Comput. Phys. Comm. **36**, 25–57.

Blakemore, J. S., 1982, J. Appl. Phys. **53**, R126–R181.

Boardman, A. D., 1980, in: *Physics programs*, ed. A. D. Boardman, Wiley, New York.

Bosi, S. and C. Jacoboni, 1976, J. Phys. **C9**, 315–319.

Braslau, N. and P. S. Hauge, 1970, IEEE Trans. El. Dev. **17**, 616–622.

Brunetti, R., C. Jacoboni, A. Matulionis and V. Dienys, 1985, Physica **134B**, 369–373.

Buot, F. A., 1987, in: *Fundamental research on the numerical modelling of semiconductor devices and processes*, ed. J. J. H. Miller, Boole, Dublin.

Casey, H. C. and M. B. Panish, 1978, in: *Heterostructure lasers, part A: Fundamental principles*, Academic, New York.

Castagné, R., 1985, Physica **134B+C**, 55–66.

Chao, P. C., S. C. Palmateer, P. M. Smith, U. K. Mishra, K. H. G. Duh and J. C. M. Hwang, IEEE El. Dev. Lett. **6**, 1985, 531–533.

Chattopadhyay, D. and H. J. Queisser, 1981, Rev. Mod. Phys **53**, 745–768.

Conwell, E. and V. F. Weisskopf, 1950, Phys. Rev. **77**, 388–390.

Dingle, R., H. L. Störmer, A. C. Gossard and W. Wiegmann, 1978, Appl. Phys. Lett. **33**, 665–667.

Eastman, L. F., 1988, *12th European workshop on compound semiconductor devices and ICs*, Lugano.

Ehrenreich, H., 1957, J. Phys. Chem. Solids **2**, 131–149.

Evanno, M. H., 1983, *Méthodes de détermination expérimentale de la vitesse électronique dans les composés semiconducteurs III–V, application au GaAs et GaInAs*, Ph. D. thesis, Université des Sciences et Techniques de Lille.

Fauqemberge, R., M. Pernisek, J. L. Thobel and P. Bourel, 1987, Proc. ESSDERC, 107–110.

Fauqemberge, R., J. L. Thobel, P. Descheerder, M. Pernisek and P. Wolf, 1988, Solid-St. El. 31, 595–598.

Fawcett, W., A. D. Boardman and S. Swain, 1970, J. Phys. Chem. Solids 31, 1963–1990.

Fritzsche, D., 1988, private communication.

Glisson, T. H., J. R. Hauser, M. A. Littlejohn, K. Hess, B. G. Streetman and H. Shichijo, 1980, J. Appl. Phys. 51, 5445–5449.

Glisson, T. H., C. K. Williams, J. R. Hauser and M. A. Littlejohn, 1982, in: *VLSI Electronics: Microstructure science*, vol. 4, Academic, New York.

Graybeal, W. J. and U. W. Pooch, 1980, *Simulation: principles and methods*, Winthrop, Cambridge, Mass.

Hall, A., 1873, Messag. Math. 2, 113.

Hammersley, J. M. and D. C. Handscomb, 1964, *Monte Carlo methods*, Methuen, London.

Harrison, J. W. and J. R. Hauser, 1976, Phys. Rev. B13, 5347–5350.

Hess, K., H. Morkoç, H. Schichijo and B. G. Streetman, 1979, Appl. Phys. Lett. 35, 469–471.

Hockney, R. W. and J. W. Eastwood, 1981, *Computer simulation using particles*, McGraw–Hill, New York.

Hockney, R. W., R. A. Warriner and M. Reiser, 1974, El. Lett. 10, 484–486.

Houston, P. A. and A. G. R. Evans, 1977, Solid-St. El. 20, 197–204.

Inoue, M. and J. Frey, 1980, J. Appl. Phys. 51, 4234–4239.

Jacoboni, C. and L. Reggiani, 1983, Rev. Mod. Phys. 55, 645–705.

Javid, M. and E. Brenner, 1963, *Analysis, transmission and filtering of signals*, McGraw–Hill, New York.

Kane, E. O., 1957, J. Phys. Chem. Solids 1, 249.

Kaszynski, A., 1979, *Etude des phénomènes de transport dans les matériaux semiconducteurs par les méthodes de Monte Carlo: application à l'arseniure de gallium de type n*, Ph. D. thesis, Université des Sciences et Techniques Lille.

Kittel, C., 1986, *Introduction to solid state physics*, 6th ed., Wiley, New York.

Kizilyalli, I. C., K. Hess, J. L. Larson and D. J. Widiger, 1986, IEEE Trans. El. Dev. 33, 1427–1432.

Knuth, D. E., 1969, *The art of computer programming*, vol. 2, Addison-Wesley, Reading, Mass.

Kroemer, H., 1985, in: *VLSI Electronics: Microstructure Science*, vol. 10, Academic, New York.

Kroemer, H., 1986, Surf. Sci. **174**, 299–306.

Kurosawa, T., 1966, J. Phys. Soc. Jpn Suppl. **21**, 424–426.

Lebwohl, P. A. and P. J. Price, 1971, Solid St. Commun. **9**, 1221–1224.

Lepore, A. N., H. M. Levy, R. C. Tiberio, P. J. Tasker, H. Lee, E. D. Wolf, L. F. Eastman and E. Kohn, El. Lett. **24**, 1988, 365–366.

Lindmayer, J. and C. Y. Wrigley, 1965, *Fundamentals of semiconductor devices*, Van Nostrand, Princeton.

Littlejohn, M. A., T. H. Glisson and J. R. Hauser, 1977, J. Appl. Phys. **48**, 4587–4590.

Littlejohn, M. A., J. R. Hauser, T. H. Glisson, D. K. Ferry and J. W. Harrison, 1978, Solid-St. El. 21, 107–114.

Littlejohn, M. A., W. M. Kwapien, T. H. Glisson, J. R. Hauser and K. Hess, 1983, J. Vac. Sci. Technol. B1, 445–448.

Lugli, P. and D. K. Ferry, 1985a, Appl. Phys. Lett. **46**, 594–596.

Lugli, P. and D. K. Ferry, 1985b, IEEE El. Dev. Lett. **6**, 25–27.

Lugli, P. and D. K. Ferry, 1985c, IEEE Trans. El .Dev. 32, 2431–2437.

Lugli, P. and C. Jacoboni, 1987, Proc. ESSDERC, 97–101.

Madelung, O., 1978, *Introduction to solid-state theory*, Springer, Berlin.

Masselink, M. T., N. Braslau, D. LaTulipe, W. I. Wang and S. L. Wright, 1988, Solid-St. El. 31, 337–340.

Matulionis, A., J. Pozela and A. Reklaitis, 1975, Solid St. Comm. **16**, 1133–1137.

Milnes, A. G., 1986, Solid-St. El. 29, 99–121.

Mimura, T., M. Abe, A. Shibatomi and M. Kobayashi, 1986, Surf. Sci. **174**, 343–351.

Mimura, T., S. Hiyamizu, T. Fujii and K. Nanbu, 1980, Jpn J. Appl. Phys. **19**, 225–227.

Moglestue, C., 1983, IEEE Proc. 130, 275–280.

Moglestue, C., 1984, IEEE Proc. 131, 193–202.

Moglestue, C., 1985, IEEE Proc. 132, 217–223.

Moglestue, C., 1986, IEEE Trans. CAD 5, 326–345.

Mönch, W., 1988, preprint, to appear in: *Proc. NATO Adv. Res. Workshop*, ed. I. P. Batra, Plenum, New York.

Morkoç, H., 1984, IEEE Spectrum (febr.), 28–35.

Mouis, M., P. Dolfus, B. Mougel, J.-F. Pône and R. Castagné, 1986, in: *High-speed electronics*, eds. B. Köllböck and H. Beneking, Springer, Berlin.

Nag, B. R., 1980, *Electron transport in compound semiconductors*, Springer, Berlin.

Nederveen, K. and T. G. van de Roer, 1988, Solid-St. El. 31, 375–377.

Nederveen, K. and J. Zimmermann, 1989, Superl. Microstr. 6., 133–137.

Okamoto, K., C. E. C. Wood and L. F. Eastman, 1981, Appl. Phys. Lett. 38, 636–638.

Panish, M. G. and A. Y. Cho, 1980, IEEE Spectrum (april), 18–23.

Perri, F., 1986, *Sur un nouveau modèle de l'interaction electron–impureté dans les semiconducteurs*, Ph. D. thesis, Université des Sciences et Techniques de Lille-Flandres-Artois.

Press, W. H., B. P. Flannery, S. A. Teukolsky and W. T. Vetterling, 1986, *Numerical recipes*, Cambridge University Press, Cambridge.

Price, P. J., 1979, in: *Semiconductors and semimetals*, vol. 14, eds. R. K. Willardson and A. C. Beer, Academic, New York.

Price, P. J., 1981, Ann. Phys. (NY) 133, 217–239.

Ravaioli, U., 1986, *Monte Carlo simulation of the High Electron Mobility Transistor*, Ph. D. thesis, Arizona State University.

Ravaioli, U. and D. K. Ferry, 1986a, IEEE Trans. El. Dev. 33, 677–681.

Ravaioli, U. and D. K. Ferry, 1986b, Superl. Microstr. 2, 377–380.

Ravailoi, U. and D. K. Ferry, 1986c, in: *High-speed electronics*, eds. B. Köllböck and H. Beneking, Springer, Berlin.

Rees, H. D., 1968, Phys. Lett. 26A, 416–417.

Rees, H. D., 1969, J. Phys. Chem. Solids 30, 643–655.

Ridley, B. K., 1977, J. Phys. C10, 1589–1593.

Robinson, G. Y., 1985, in: *Physics and chemistry of III–V compound* *semiconductor interfaces*, ed. C. W. Wilmsen, Plenum, New York.

Rode, D. L., 1978, in: *Semiconductors and semimetals*, vol. 10, eds. R. K. Willardson and A. C. Beer, Academic, New York.

Saxena, A. K., 1985, J. Appl. Phys. 58, 2640–2645.

Seeger, K., 1973, *Semiconductor physics*, Springer, Berlin.

Shaw, M. P., 1981, in: *Handbook on semiconductors*, vol. 4, ed. C. Hilsum, North-Holland, Amsterdam.

Shreider, Yu. A., ed., 1966, *The Monte Carlo method*, Pergamon, Oxford.

Smith, R. A., 1978, *Semiconductors*, 2nd ed., Cambridge University Press, Cambridge.

Sze, S. M., 1981, *Physics of semiconductor devices*, 2nd ed., Wiley, New York.

Takenaka, N., M. Inoue and Y. Inuishi, 1979, J. Phys. Soc. Jpn 47, 861–868.

Thobel, J. L., 1988, *Simulation Monte Carlo de composants submicroniques à effet de champ et à heterojonctions, application au TEGFET et à ses structures derivées*, Ph. D. thesis, Université des Sciences et Techniques de Lille-Flandres-Artois.

Tomizawa, M., A. Yoshii and K. Yokoyama, 1985, IEEE El. Dev. Lett. 6, 332–334.

Ulam, S. M. and J. von Neumann, 1947, Bull. Am. Math. Soc. 53, 1120.

Van de Roer, T. G., 1989, private communication.

Van de Roer, T. G. and F. P. Widdershoven, 1986, J. Appl. Phys. 59, 813–815.

Vinter, B., 1973, Ph. D. thesis, Technical University of Denmark.

Vinter, B., 1985, Lecture notes for 'Winter school on semiconductor heterojunctions and superlattices', Les Houches.

Wang, T. and K. Hess, 1985, J. Appl. Phys. 57, 5336–5339.

Warriner, R. A., 1977a, Solid-St. El. Dev. 1, 105–110.

Warriner, R. A., 1977b, Solid-St. El. Dev. 1, 92–96.

Watanabe, M. O., J. Yoshida, M. Mashita, T. Nakanisi and A. Hojo, 1985, J. Appl. Phys. 57, 5340.

Widdershoven, F. P., 1984a, Master's Thesis, no. ET-4-84, University of Technology Eindhoven.

Widdershoven, F. P., 1984b, private communication.

Widiger, D., K. Hess and J. J. Coleman, 1984, IEEE El. Dev. Lett. 5, 266–269.

Widiger, D. J., I. C. Kizilyalli, K. Hess and J. J. Coleman, 1985, IEEE Trans. El. Dev. **32**, 1092–1102.

Williams, C. K., 1982, *Monte Carlo studies of the electron transport in III–V semiconductors and semiconductor devices*, Ph. D. thesis, North Carolina State University, Univ. Microfilm Int., Ann Arbor.

Williams, C. K. and T. H. Glisson, 1985, private communication.

Williams, C. K., T. H. Glisson, J. R. Hauser, M. A. Littlejohn and M. F. Abusaid, 1985, Solid-St. El. **28**, 1105–1109.

Williams, C. K., M. A. Littlejohn, T. H. Glisson and J. R. Hauser, 1986, Superl. Microstr. **2**, 201–207.

Yokoyama, K. and K. Hess, 1986, Phys. Rev. **B33**, 5595–5606.

Yuh Fong Tang, J., 1985, IEEE Trans. El. Dev. **32**, 1817–1823.

Ziman, J. M., 1960, *Electrons and phonons*, Clarendon, Oxford.

Ziman, J. M., 1972, *Principles of the theory of solids*, 2nd ed., Cambridge University Press, Cambridge.

Zimmermann, J., 1987, private communication.

Zimmermann, J. and Wu Yen, 1987, Revue Phys. Appl. **22**, 1501–1513.

SUMMARY

This thesis deals with the modelling of various aspects of electron transport in AlGaAs/GaAs heterostructures. For this purpose the Ensemble Monte Carlo method is applied. In this method the Boltzmann transport equation is solved with statistical techniques, from the knowledge of the electric field and the rates of different possible interactions of an electron with the semiconductor lattice (the scatter rates).

In chapter 2 the principles of the Monte Carlo technique are outlined, in chapter 3 followed by a discussion of the scatter processes which are taken into account in the semiconductors considered here.

In chapter 4 first the working of the computer program developed is tested by simulations of bulk GaAs, with and without taking into account ionized impurity scattering. The results agree with other Monte Carlo calculations and scarcely available measurements. Furthermore, as in heterojunctions high electron concentrations can arise at the GaAs side of the AlGaAs/GaAs interface, the influence of degeneracy and electron–electron scattering is investigated in bulk GaAs. An existing model for taking into account the degeneracy effects at low electric fields is extended and made suitable for high fields. Velocity–field curves are obtained for an ionized impurity and electron density of 10^{18} cm^{-3}. As a result of the inclusion of degeneracy velocity is slightly changed; an increase at fields until 10 kV/cm, a decrease at higher fields. The energy distribution as a whole is shifted towards higher energy, especially at low fields. Electron–electron scattering causes an increase in

velocity in the order of 10 % at fields between 5 and 30 kV/cm. Although the average energy is hardly affected the high- and low-energy tails of the energy distribution both get pushed towards the centre of the distribution. This causes a reduction of intervalley scattering.

When both mechanisms are combined their effects are superposed. In a way both mechanisms counteract, especially their effect on the high-energy tail of the energy distribution. In general, at the densities considered, the influence on the transport properties is not dramatical. Electron–electron scattering is the most prominent of the two.

In chapter 5 the electron transport along the AlGaAs/GaAs interface under influence of a constant longitudinal field (parallel to the interface) is studied. Poisson's equation is solved in one dimension, providing the transverse electric field in a selfconsistent manner. The scatter rates which are used are the same as in the bulk case, which implies that energy discretization effects are not accounted for. It is found that the average steady-state velocities, of the electrons in GaAs, parallel to the interface are higher than in bulk GaAs under the same electric field. It is demonstrated that both real space transfer and the transverse electric field are responsible for this increase in velocity. Both reduce the number of electrons which transfer between the Γ- and L-valley in steady state. As a result the average velocity in the Γ-valley is higher, and therewith the total average velocity.

In chapter 6 an Ensemble Monte Carlo model is presented for the High Electron Mobility Transistor (HEMT), in which Poisson's equation is solved in two dimensions. First the criteria to obtain a numerically stable calculation are summarized. From these criteria a stable so-called time integration scheme is derived.

The I_D–V_{DS} characteristics for an HEMT with a gate length of 0.3 μm are calculated. Furthermore the small-signal parameters, like the transconductance, the source-to-gate capacitance and the cutoff frequency are determined. The results found here are qualitatively in accordance with those from others. However, the currents obtained here are higher, and as a consequence the maximum cutoff frequency is also higher (±190 GHz against 110 GHz).

It is pointed out that at high drain voltages the most important contribution to real space transfer from GaAs to AlGaAs behind the gate comes from electrons in the L- and X-valleys. Therefore, it can be concluded that the current saturation is especially caused by intervalley transfer in GaAs.

A decrease of the gate length to about 0.1 μm causes an increase of the maximum cutoff frequency, which is mainly caused by a decrease in source-to-gate capacitance. The interelectrode spacings here are found to have a minor influence, although the cutoff frequencies are somewhat higher with the higher interelectrode spacings.

In chapter 7 it is described how, using Fermi's Golden Rule, the coupling between confined 2D states in the well and 3D Bloch states in the bulk can be introduced into a Monte Carlo model which describes out-of-equilibrium electron transport in a heterojunction quantum well. This new transition process is called Quantum Well Transfer.

Here a so-called Quantum Well Escape process involving polar-optical phonons is elaborated. However, in the described formalism, in principle every known, elastic as well as inelastic, scatter process may be involved. The developed Quantum Well Transfer mechanism is straightforward and could easily be implemented.

SAMENVATTING

Dit proefschrift behandelt het modelleren van diverse aspekten van het elektronentransport in AlGaAs/GaAs heterostrukturen. Hierbij is gebruik gemaakt van de Ensemble Monte Carlo methode. Bij deze methode wordt de Boltzmann transport vergelijking opgelost met statistische technieken, uitgaande van de waarde van het elektrisch veld en de frekwenties van de mogelijke interakties van een elektron met het halfgeleiderrooster (de verstrooiingsfrekwenties).

In hoofdstuk 2 wordt het principe van de Monte Carlo techniek geschetst, in hoofdstuk 3 gevolgd door een behandeling van de verstrooiingsprocessen die mee zijn genomen voor de in dit proefschrift beschouwde halfgeleiders.

In hoofdstuk 4 wordt eerst de werking van het ontwikkelde computerprogramma getest aan de hand van simulaties aan bulk GaAs, waarbij afwisselend de verstrooiing aan geionizeerde verontreinigingen wel en niet meegenomen wordt. De resultaten komen zowel met de resultaten van andere Monte Carlo berekeningen overeen als met metingen, voor zover beschikbaar.

Aangezien in heterojunkties hoge elektronenkoncentraties kunnen voorkomen aan de GaAs kant van het AlGaAs/GaAs grensvlak, is in bulk GaAs de invloed van degeneratie en elektron–elektron verstrooiing onderzocht. Een bestaand model voor het meenemen van degeneratie-effekten bij lage elektrische velden is uitgebreid en geschikt gemaakt voor hogere velden. Snelheids–veld relaties zijn verkregen in het geval dat de dichtheid van de geionizeerde verontreinigingen en van de elektronen 10^{18} cm^{-3} bedraagt. Als gevolg van het meenemen van degeneratie treedt een geringe verandering in de snelheid op; een verhoging bij velden tot 10 kV/cm, een verlaging bij hogere velden. De energieverdeling verschuift in zijn geheel naar hogere energiewaarden, vooral bij lage velden. Elektron—elektron verstrooiing veroorzaakt een vergroting van de snelheid in de orde van 10% voor velden van 5 tot 30 kV/cm. Hoewel de gemiddelde energie nauwelijks verandert worden de staarten van de energieverdeling, zowel bij lage als hoge energie, naar het centrum van de verdeling gedrukt. Als gevolg hiervan neemt intervallei verstrooiing in frekwentie af.

Als beide mechanismen tegelijkertijd meegenomen worden, worden hun effekten gesuperponeerd. In zekere zin werken ze elkaar tegen, vooral wat betreft hun invloed op de staart van de energieverdeling bij hoge energie. In het algemeen kan gesteld worden dat het effekt op de transport eigenschappen gering is. Elektron—elektron verstrooiing is de meest dominante van de twee.

In hoofdstuk 5 wordt het elektronentransport langs het AlGaAs/GaAs grensvlak onder invloed van een konstant longitudinaal veld (parallel aan het grensvlak) bestudeerd. Door de Poisson vergelijking ééndimensionaal op te lossen wordt het transversale veld op een zelfkonsistente manier verkregen. Effekten van energie-diskretizatie worden verwaarloosd, zodat dezelfde verstrooiingsfrekwenties als in de berekeningen aan bulk GaAs worden gebruikt. De gemiddelde stationaire snelheden parallel aan het grensvlak van de elektronen in het GaAs blijken hoger te zijn dan in bulk GaAs onder invloed van een vergelijkbaar elektrisch veld. Er wordt aangetoond dat zowel *real space transfer* als het transversale veld verantwoordelijk zijn voor deze toename in snelheid. Beide verminderen ze het aantal elektronen dat in stationaire toestand tusen de Γ- en L-vallei heen en weer beweegt. Als gevolg hiervan is de gemiddelde snelheid in de Γ-vallei hoger, en daarmee de totale snelheid.

In hoofdstuk 6 wordt een Ensemble Monte Carlo model gepresenteerd voor de *High Electron Mobility Transistor* (HEMT), waarbij de Poisson vergelijking twee-dimensionaal opgelost wordt. Om te beginnen worden de kriteria opgesomd om tot een numeriek stabiel schema te komen. Hiervan uitgaand wordt een numeriek stabiel tijd-integratie schema afgeleid.

In de eerste plaats zijn de I_{DS}–V_{DS} karakteristieken voor een HEMT met *gate* lengte van 0.3 μm berekend. Verder zijn de klein-signaal parameters, zoals de steilheid, de *source-gate* kapaciteit en de afsnijfrekwentie bepaald. De hierbij verkregen resultaten zijn kwalitatief in overeenstemming met werk van anderen. Echter zijn de stromen hier hoger, waardoor ook de maximale afsnijfrekwentrie hoger is (±190 GHz tegen 110 GHz).

Het blijkt dat bij hoge *drain* spanningen de grootste bijdrage aan *real space transfer* van GaAs naar AlGaAs aan het eind van de *gate* afkomstig is van elektronen die zich in de L- en X-valleien bevinden. Hieruit valt af te leiden dat de verzadiging van de stroom vooral veroorzaakt wordt door intervallei verstrooiing in GaAs.

Een verkleining van de *gate* lengte naar ongeveer 0.1 μm veroorzaakt een verhoging van de maximale afsnijfrekwentie, die vooral veroorzaakt wordt door een vermindering van de *source-gate* kapaciteit. Hoewel bij grotere interelektrode afstanden de afsnijfrekwenties wat hoger zijn, hebben deze afstanden hierbij weinig invloed.

In hoofdstuk 7 wordt beschreven hoe in een Monte Carlo model voor niet-stationair elektronentransport in een heterojunktie kwantumput, een mechanisme geintroduceerd kan worden om de koppeling tot stand te brengen tussen de opgesloten 2D toestanden in de put en de 3D toestanden in de bulk, met behulp van Fermi's Gulden Regel. Dit nieuwe overgangsproces wordt aangeduid met *Quantum Well Transfer*.

Het geval van een zogenaamd *Quantum Well Escape* proces waarbij polair-optische fononen betrokken zijn wordt verder uitgewerkt. In principe kan echter ieder proces, elastisch of inelastisch, met behulp van dit formalisme meegenomen worden. Het *Quantum Well Transfer* mechanisme kan eenvoudig geimplementeerd worden.

ACKNOWLEDGEMENTS

The calculations described in this thesis have been produced by computer programs which have been developed and tested on various computer systems which all were situated in the Laboratory of Automated Design of the University of Technology Eindhoven. I would like to thank the various system managers I bothered in the course of the work, namely Oege Koopmans, Alberto Martis, Herman Rohenkohl and Hans van Zuidam, for their cooperation.

With the technical preparation of this thesis I have been especially helped by Frans Starmans who made a couple of fine drawings and did a lot of wordprocessing. Furthermore, Tine Bijl, Hugo Heyker, Theo Smedes and Lidewij Hompe-Jansen van Galen have contributed to the preparation of the manuscript. I would like to thank them for their help.

I had the opportunity to work some time under the guidance of Jacques Zimmermann from the University of Lille. I thank him for many stimulating discussions. Furthermore, I am very grateful for the support I received from Jean-Luc Thobel of the same University.

Furthermore, I thank Harold Balemans who, as a student, set the first steps towards the HEMT model together with me and who made some nice plot programs.

And above all I would like to thank the people who have guided me during the course of this work, especially while writing the thesis, for their valuable support and patience, namely dr ir Van de Roer, Prof. Klaassen and Prof. Kaufmann.

LEVENSLOOP

De auteur van dit proefschrift werd geboren op 1 november 1957 te Rotterdam. Van 1970 tot 1976 volgde hij de opleiding gymnasium β aan de Openbare Scholengemeenschap Prof. Casimir in Vlaardingen. Van 1976 tot 1982 studeerde hij Technische Natuurkunde aan de Technische Hogeschool in Delft. Van 1983 tot 1984 was hij werkzaam als bureauredakteur bij Elsevier Science Publishers in Amsterdam. Van 1984 tot 1988 werkte hij als wetenschappelijk assistent bij de Technische Universiteit Eindhoven, Fakulteit der Elektrotechniek, eerst bij de vakgroep Theoretische Elektrotechniek, daarna bij de vakgroep Elektronische Bouwstenen. Momenteel is hij werkzaam bij het ASM Micro-electronics Technology Centre in Bilthoven.

Stellingen behorende bij het proefschrift:

Ensemble Monte Carlo simulation
of
electron transport in AlGaAs/GaAs heterojunctions

door

Karel Nederveen

1. De bewering van Lugli en Ferry dat het Pauli principe hetzelfde effekt heeft op de energieverdeling van elektronen als elektron-elektron interaktie is op zijn minst verwarrend, aangezien deze bewering alleen juist is voor elektronen die zich in de lage-energie staart van de verdeling bevinden.
Dit proefschrift, Hoofdstuk 4;
P. Lugli and D.K. Ferry, 1985, IEEE Trans. El. Dev. 32, 2431-2437.

2. De manier waarop Hockney en Eastwood met de Monte Carlo methode de verplaatsing van het elektron berekenen levert een tijd-integratie schema op dat volgens de door henzelf gehanteerde kriteria instabiel is.
Dit proefschrift, Hoofdstuk 6;
R.W. Hockney and J.W. Eastwood, 1981, Computer simulation using particles, McGraw-Hill, New York.

3. De door Hockney en Eastwood gehanteerde manier om, in Monte Carlo berekeningen, de vrije-vluchttijd van een elektron te selekteren met behulp van getabelleerde *self-scatter* konstantes is principieel onjuist.
R.W. Hockney and J.W. Eastwood, 1981, Computer simulation using particles, McGraw-Hill, New York.

4. Met behulp van een *multi-wafer CVD* reaktor kan dezelfde uniformiteit in laagdikte op een halfgeleiderplak bereikt worden als met een *single-wafer* reaktor.
K. Nederveen, AMTC Activity Report, May-June 1989.

5. Het door K.Y. Toh voorgestelde "engineering model" is te onnauwkeurig voor de berekeningen van de eigenschappen van CMOS schakelingen.
K.Y. Toh, 1988, IEEE/SSC 23, 950.

6. De cocitatie-clusteranalyse methode is veeleer een sociologisch instrument om vriendengroepen op te sporen dan een betrouwbaar hulpmiddel om de kwaliteit van wetenschappelijk onderzoek te meten.
J. van Deen, 1987, Nederlands Tijdschrift voor Natuurkunde B53, 105-107.

7. Een dicht gepakte groep mensen gedraagt zich niet als een vloeistof, maar als een vaste stof met een kleine elasticiteitsmodulus en Poissonkontraktie.

8. Om te komen tot een konsekwente spelling van het Nederlands zijn er slechts twee mogelijkheden: de "ouderwetse" spelling handhaven die zoveel mogelijk recht doet aan de oorsprong van woorden, of een "moderne" spelling invoeren die zoveel mogelijk de Duitse spellingsprincipes overneemt.

9. Het wettelijk verplicht stellen van "positieve diskriminatie" van nauwkeurig omschreven groepen mensen uit de samenleving werkt stigmatiserend en is niet bevorderlijk voor het gevoel van eigenwaarde van de leden van betreffende groepen.

10. Méér nog dan over de vraag of de gewenste doelen wél bereikt worden dienen wetgevers zich, bij het ontwerpen van nieuwe wetten, te buigen over de vraag of niet-gewenste doelen juist níet bereikt worden.

11. Bij niet-kunstliefhebbers leeft het idee dat "kunst" en "mooi" synoniem zouden moeten zijn. Dit is een misverstand: "mooi" is een van de mogelijke kwalifikaties van iets waarvan objektief is vast te stellen dat het "kunst" betreft.

12. Het gebruik van het woord "gebeuren" als zelfstandig naamwoord wijst op een gebrek aan taalkundig vermogen bij de spreker om duidelijk te maken wát er nu eigenlijk gebeurt.